VOLCANO-PLUTON CONNECTIONS IN SILICIC MAGMATIC SYSTEMS: INSIGHTS FROM SOUTHEAST ICELAND AND SOUTHERN NEVADA

By

Abraham de Jesus Padilla

Thesis

Submitted to the Faculty of the
Graduate School of Vanderbilt University
in partial fulfillment of the requirements
for the degree of

MASTER OF SCIENCE

in

Earth and Environmental Sciences

August, 2011

Nashville, Tennessee

Approved:

Professor Calvin F. Miller

Professor Guilherme A.R. Gualda

To my Father and Mother, for being my biggest source of inspiration and motivation, and for giving me their unconditional love and support in my science quest.

ACKNOWLEDGEMENTS

I owe my deepest gratitude to professors Calvin Miller and Guilherme Gualda for their incredible guidance, patience, and motivation, on and off the field, for helping me explore and expand my scientific curiosity, for teaching me to think critically about volcanic-plutonic systems and processes, for stimulating my intellectual growth, for putting up with me through the learning process, and for providing me with the opportunity to visit and work in some of the most incredible natural geologic laboratories this Earth has to offer! I owe a great deal of appreciation to my incredible friend, Beverly Walker, for her unlimited company and support through rain and shine, for helping me maintain my sanity, and for being by my side in facing all the challenges that come with Graduate School.

I am also grateful for the company provided by Tamara Carley and Evan Kelly in the field, as well as their support and assistance with sample processing and laboratory work off the field; Danny Flanagan for making life SO MUCH easier with ***FlannyPlot***, and generously helping me with thesis editing and formatting; Lily Claiborne, for always taking the time to sit with me and share her zircon knowledge; professor David Furbish for never failing to help me find and see the fun and excitement in every aspect of science; my fellow MESSYers for providing fun and insightful magma discussions; Vanderbilt EES Faculty and Graduate Students, Aaron Covey, Teri Sparkman, and Jewell Beasley-Stanley for being there to make sure this department runs smoothly; my wonderful family for their unconditional love and support, and for always pushing me to keep moving forward in my quest for science; and Warner Cribb, at the MTSU XRF lab, and Joe Wooden, at the SUMAC SHRIMP-RG lab, for their help and technical support with analytical work. This research would not have been possible without the financial support of the National Science Foundation (grants NSF-EAR-0635922, NSF-EAR-0948528, and NSF-EAR-0948528), the Geological Society of America (graduate student grant #9264-10), and Vanderbilt's Department of Earth and Environmental Sciences.

TABLE OF CONTENTS

Page

PART I

Chapter

PART II

Chapter

Appendix

LIST OF TABLES

Part I

Table

Part II

Table

LIST OF FIGURES

Part I

Figure

Part II

Figure

INTRODUCTION

Silicic rocks make up a large fraction of the continental crust, and thus silicic magmatism plays a key role in the creation and evolution of continental crust as well as continental landmasses. It is important to study such magmatic systems to gain better understanding of how they evolve through time, their contribution to Earth's history, and the processes that control whether these magmas are ultimately ponded in the upper crust, solidifying into silicic plutons, or are erupted at the surface via volcanic centers.

Whether plutonic magmatic systems within the Earth's crust and volcanic complexes at the Earth's surface are genetically related remains a topic of disagreement among members of the geological community. There are currently two dominant and contrasting end-member hypotheses for the existence, or lack, of a genetic volcano-pluton connection. In the first hypothesis, plutons and volcanoes are interpreted as relatively independent systems that evolve with limited interaction with each other. Large plutons preserve batches of magmas that are accumulated over time as small intrusions, suggesting that large volumes of magma capable of producing the largest volcanic eruptions do not exist as single integrated reservoirs at any one point in time (e.g. Coleman *et al.*, 2004; Glazner, *et al.*, 2004). In contrast, volcanic complexes are interpreted to be fed by magmas that are produced at depth, move upward through the crust relatively rapidly with limited interactions, and are only stored briefly beneath the volcano prior to being erupted at the Earth's surface (e.g. Glazner, *et al.*, 2004).

Alternatively, many authors argue that plutons and volcanoes are part of large, complex, and commonly interconnected systems in which magmas accumulate, interact, and evolve within the crust over hundreds of thousands to millions of years, regularly stalling, cooling and crystallizing beneath volcanoes in an active intrusive body, and are often rejuvenated, remobilized, and incorporated by younger, hotter magmas as these make their way to the surface for eruption (e.g. Claiborne *et al*., 2006; Lipman, 2007; Walker *et al.*, 2007; Bolhar *et al.*, 2008; Shane *et al.*, 2008; Claiborne *et al.*, 2010b).

In this study, we advocate for the latter hypothesis and present our arguments for the volcano-pluton connections preserved within the Austurhorn Intrusive complex and the Highland Range silicic volcanic sequence. We aim to understand the processes by which silicic magmatic systems evolve and are terminated, and the link between magmatic processes at depth and eruptive centers on Earth's surface. We present evidence from two perspectives: the evolution of a shallow subvolcanic plutonic silicic system, recorded in the mineral *zircon*, at Austurhorn Intrusive Complex (AIC), Iceland, and the death of a silicic magmatic system, indicated by field relationships and geochemistry, in the Highland Range Silicic Volcanic Sequence (HRSVS), Nevada. Both systems preserve a striking record of the complex interactions that take place between mafic and felsic magmas. While we employ different methods in the study of each setting, we emphasize the similarity between the two complexes in that both are part of greater systems that preserve intrusive as well as extrusive components characterized by extensive mafic-felsic magmatic interactions. The research presented here helps shed light on the significance of such interactions in the evolution of volcano-pluton systems, the generation of explosive silicic magmas from effusive mafic parents, and the role such processes have played in the evolution of the Earth's crust.

PART I

The Austurhorn Intrusive Complex, southeast Iceland

CHAPTER I

INTRODUCTION

Zircon ($ZrSiO_4$), though a minor constituent, is present in most rocks and sediment in and on the Earth's crust and is an ideal tool for investigating the evolution of magmas and the connections between volcanic and plutonic magmatic systems. Its low solubility in almost all melt and fluid compositions, its stability at Earth's surface, and its physical durability during transport enables it to survive many crustal processes during which most or all other minerals are destroyed. Furthermore, elemental diffusion in zircon is extremely slow (e.g. Cherniak *et al.*, 1997a,b; Watson and Cherniak, 1997; Cherniak and Watson, 2000, 2003, 2007), so it retains elemental concentrations and zoning patterns that provide information about the environments in which it grew (e.g., Ti provides information about temperature, Hf about the composition of the melt from which a crystal was growing, rare earth elements about other environmental factors). Finally, it incorporates abundant U and Th, and since diffusion of Pb in zircon is extremely slow, age information is preserved, growth zones can be dated, and the ages of the environments that it records can be determined (e.g. Hoskin and Schaltegger, 2003). However, despite widespread recognition of the value of zircon for elucidating the temporal and environmental record of magmatic processes, there has been almost no investigation of this mineral in Iceland plutonic rocks (e.g. Furman *et al.*, 1992a).

Due to its unique location, an oceanic divergent boundary coupled with a hot-spot, as well as to the unusual presence and abundance of felsic rocks in this oceanic setting, Iceland has been the subject of intensive petrologic study. However, most previous work has focused on volcanism (Gunnarson *et al*., 1998; Martin and Sigmarsson, 2007; Carley *et al*., 2009); less attention has been paid to the plutonic rocks. The relatively well-studied Austurhorn Plutonic Complex (Blake, 1966; Gale *et al*., 1966; Mattson *et al*., 1986; Furman *et al*., 1992a, 1992b; Thorarinsson and Tegner, 2009), situated in southeastern Iceland, exemplifies the mafic-felsic magma interaction typical of granites and rhyolitic systems in Iceland, and thus provides an ideal location to investigate how relatively large volumes of silicic magmas develop and potentially create new continents in oceanic settings, and helps to evaluate whether such processes have been important in generation of silicic crust throughout Earth history.

Geologic Setting: The Austurhorn Intrusive Complex, SE Iceland

The Austurhorn Intrusive Complex (AIC) is a small Tertiary silicic center located along the coast of southeastern Iceland. Outcropping over 15 km^2, the AIC is comparable in dimension and in diversity and abundance of rock types to modern and Tertiary Icelandic central volcanoes (Fig. 1). The exposed portion of the AIC includes roof and wall contacts in several locations. It intrudes predominantly basaltic lavas that dip gently to the west, products of the Álftafjördur and Lón mid-Miocene central volcanoes (Fig. 1; Furman, 1992a; Mattson et al, 1986; Blake, 1966). The intrusion comprises granophyre, gabbro, and an associated mafic-felsic composite zone (MFCZ – previously referred to as the "net-veined complex," e.g. Furman *et al.*, 1992; Mattson *et al.*, 1986; Blake, 1966) in which evidence for open system behavior, including chamber replenishment by dense basaltic and buoyant felsic magmas indicated by the mingling and mixing of magmas, is observed (Mattson et al, 1986; Furman, 1992). The exposed gabbro is

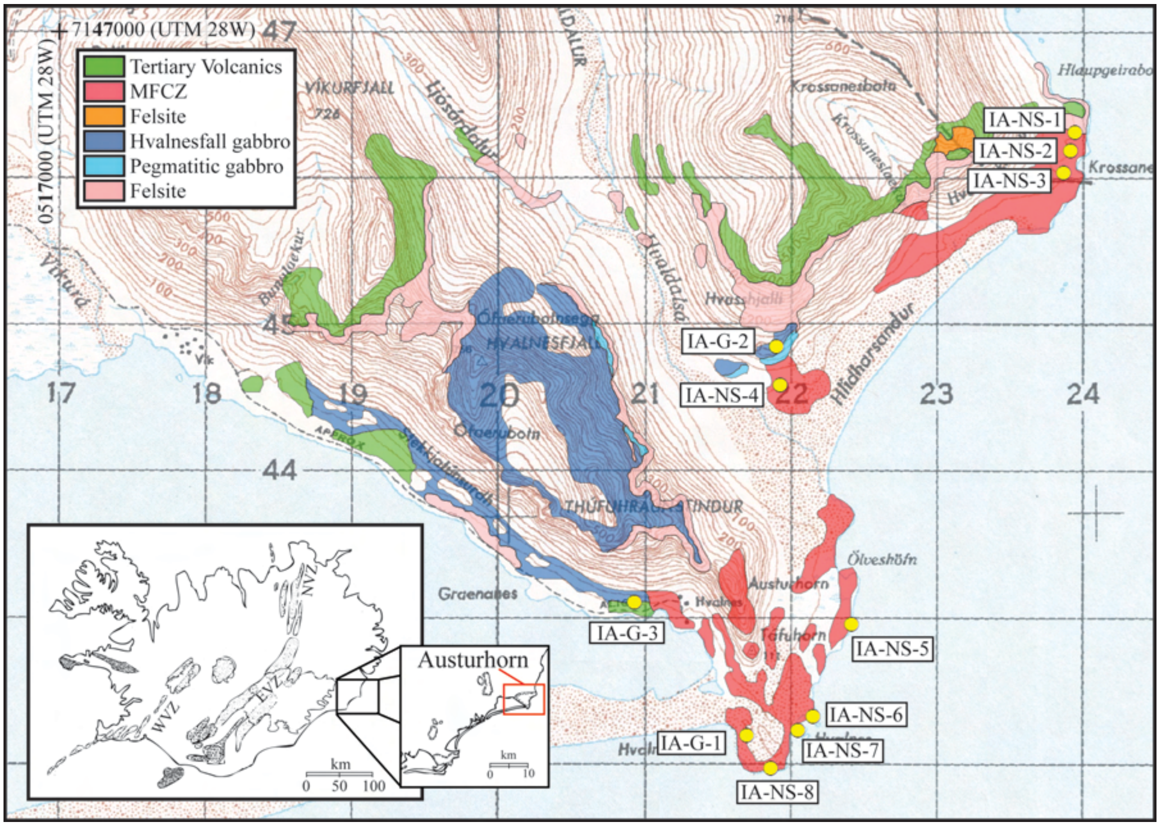

Figure 1 – Geologic map of the Austurhorn Intrusive Complex. Insets: regional map of Iceland; Northern (NVZ), Eastern (EVZ), and Western Volcanic Zones (WVZ) and the Austurhorn Peninsula are indicated (modified after Furman *et al.*, 1992).

largely restricted to Hvalnesfjall (Fig. 1) in the central part of the complex, and appears to be entirely encircled by granophyre (Blake, 1966).

The structure of the intrusion and geochemistry of the mafic and felsic rocks at AIC suggest it developed within a short-lived immature axial extensional environment, analogous to the Eyjafjallajökull and Torfajökull central volcanoes in Iceland's modern Eastern Neovolcanic Zone (EVZ; Furman, 1992a), which are constructed from both basaltic and silicic eruption products. The AIC is thus interpreted to represent an exhumed Tertiary central volcano. Late stage mafic dikes and sheets of tholeiitic basalt intrude the complex, suggesting that magmatic heat was abundantly available throughout the evolution of the system. Previous studies have constrained the origin of felsic magmas at pressures greater than 1 kbar, primarily based on field relations, presumably by fractional crystallization (Furman *et al.*, 1992). The complex has been previously dated by K-Ar, using biotite from the gabbro intrusion, at an age of 6.6 ±0.4 Ma (Mattson *et al.*, 1986; Moorbath *et al.*, 1968).

The Mafic-Felsic Composite Zone (MFCZ)

This composite zone, containing juxtaposed mafic and felsic rocks, occupies the lowest structural levels exposed from Hvalnes north to Hlaupgeirabotn, where it intrudes Tertiary volcanics (Fig. 1). It comprises approximately 30-40% of the AIC in three main areas at the eastern margins of the intrusion (Mattson et al, 1986; Furman, 1992). The zone is dominated by mafic-to-intermediate enclaves (pillow-like bodies), with cuspate, crenulate, or angular boundaries and entirely surrounded by silicic rock, and sheets. The enclave density within a given outcrop is highly variable, ranging from a few volume percent up to 60%. Furman *et al.* (1992a) attribute the lack of convective mixing of the Austurhorn chamber to infrequent felsic replenishment during this time.

The overall appearance of the MFCZ is that of a large composite silicic intrusion that contains abundant (up to 50%) clasts, pillows, tabular masses, and sheets of diabasic and basaltic rock. The margins of the MFCZ have been defined by Furman *et al.* (1992) to be where a felsic host rock bearing mafic blocks > 5 cm in dimension is in contact with Hvalnesfjall gabbro or Tertiary volcanics, or where mafic blocks disappear abruptly without apparent change in the felsic matrix itself. They identify up to 16 individual felsic units, which occur commonly as sills of up to 500 m lateral extent with generally distinct contacts. These felsic units can be grouped into four rock types based on bulk composition and mafic enclave abundance: (type 1) enclave-free homogeneous granophyres; (type 2) enclave-bearing granophyres with up to 40 vol.% angular mafic enclaves; (type 3) granophyres that are heterogeneous, extensively mixed and mingled, and containing partially hybridized zones and all types of mafic enclaves, ranging from micro-enclaves distinguishable in thin section to large pillows and clasts; and (type 4) foliated enclave-free granodiorite with up to 10% acicular amphibole.

CHAPTER II

METHODS

Fieldwork

Our research team (hereafter “we”) spent a total of 7 days in the field doing a hiking transect of the “mafic-felsic composite zone” (MFCZ), making careful observations on the contact relationships and the nature of interaction between felsic and mafic units, and characterizing the diversity of felsic rock units as well as the distribution and abundance of mafic pillows and clasts within them (see *Field Observations* under *Results* for more detailed descriptions). Our study built upon field descriptions of the Austurhorn Intrusive Complex and MFCZ outlined by Furman *et al.* (1992) and Mattson *et al.* (1986). We collected a total of 11 representative samples from well-exposed outcrops of the MFCZ, and surrounding gabbro and granophyre units within the AIC (see Fig. 1 and Table 1 for locations and sample descriptions). Felsic samples collected within the MFCZ, selected based on differing textures, grain size and/or mafic phenocryst content, as well as the abundance of mafic material (pillows, enclaves, and/or clasts), span the diversity of felsic components within the zone.

Thin Section Petrography

Thin-sections were prepared by Idaho Petrographics (Grangeville, ID). I used a Zeiss Axioskop 40 petrographic microscope, equipped with an AxioCam MRc 5 camera, at Vanderbilt

Table 1

AUSTURHORN INTRUSIVE COMPLEX

Thin Section Petrography

Sample	Lithology	Location (UTM 28W)		Petrographic Summary			
		Easting	Northing	Major Mineral Phases[a] (approx. modal abundance)	Accessory Phases	Textural Features	Mafic Content
IA-NS1	Granophyre	**524155**	**7146435**	Qtz (~20%), feld (~60%), CPX (~7%), oxides (~5%), bio (<2%), amph (5-7%), epi (<2%; S)	zircon, sphene, apatite	homogeneous, micrographic	absent
IA-NS2	Granophyre	**524122**	**7146308**	Qtz (30-35%), feld (~40-45%), amph (~10%), oxides (~5%), CPX (~5%), bio (<1%), chl (<5%; S), epi (S)	zircon, sphene (sub- to euhedral)	micrographic, strong alteration	micro enclaves, clasts, pillows
IA-NS3	Granodiorite	**524076**	**7146157**	Qtz (<5%), plag (~70%), CPX (~5%), amph (~10%), oxides (~5%), chl (5-10%; S), epi (S)	zircon, sphene	strong alteration	pillows, mafic zones
IA-NS4a	Granophyre	**522128**	**7144701**	Qtz (~20-25%), feld (~70%), oxides (~7%), amph (<2%; S), CPX (<2%), bio (<1%)	zircon, sphene (sub- to euhedral)	strong alteration, micrographic	poor
IA-NS4b	High-Si Granophyre	**522128**	**7144701**	Qtz (~45-50%), feld (~50%), oxides (<2%), epi (<1%; S), chl (<1%; S)	zircon, sphene (anhedral)	micrographic, strong alteration	poor
IA-NS5	Granophyre	**522618**	**7143057**	Qtz (~30%), feld (~45%), amph (~5%), oxides (~5%), bio (<5%), chl (~10%; S), epi (<2%; S)	zircon, sphene (sub- to euhedral), apatite	homogeneous	clasts, pillows, mafic zones

[a] See notes on page 11.

Table 1 (continued)

AUSTURHORN INTRUSIVE COMPLEX

Thin Section Petrography

Sample	Lithology	Location (UTM 28W)		Petrographic Summary			
		Easting	Northing	Major Mineral Phases[a] (approx. modal abundance)	Accessory Phases	Textural Features	Mafic Content
IA-NS6	Diorite	**522353**	**7142422**	Qtz (~5%), feld (~75%), oxides (~5-10%), amph (<2%), epi (~5-10%; S), chl (<5%; S)	zircon, sphene (sub- to euhedral), allanite, apatite	homogeneous	clasts, pillows, mafic sheets & pods
IA-NS7	Granodiorite	**522250**	**7142329**	Qtz (~20%), feld (~40-45%), amph (10-15%), bio (5-10%), oxides (~5-7%), chl (5-10%; S), epi (<2%; S)	zircon, sphene (sub- to euhedral)	micrographic, acicular amph	absent
IA-NS8	Granophyre	**522062**	**7142067**	Qtz (~30%), feld (~50%), oxides (~5%), chl (<10%; S), epi (<3%; S), calc (<1%; S)	zircon, sphene, apatite	mild alteration	mafic dikes
IA-G1	Gabbro	**521899**	**7142291**	Plag (~40%), CPX (~25%), oxides (~15%), amph (~25%; S), bio (<5%), chl (<5%; S), qtz (<5%; S)	zircon, sphene, apatite	homogeneous, acicular oxides	n/a
IA-G3	Gabbro	**521124**	**7143207**	Plag (~45%), CPX (~30%), oxides (15-20%), amph (~5%; S), chl (<1%; S)	zircon	homogeneous	n/a

Notes: [a] Mineral phases: quartz (qtz), feldspar (feld), clinopyroxene (CPX), Fe-Ti oxides (oxides), amphibole (amph), epidote (epi), chlorite (chl), biotite (bio), calcite (calc), and secondary phases (S).

University's Earth & Environmental Sciences Department to examine each thin-section and characterize its mineral assemblage and textural relations.

Whole-Rock Geochemistry

I selected eleven representative samples from the Austurhorn Intrusive Complex to be analyzed for whole-rock geochemistry. Thirty to forty-five grams of rock chips from each sample were mailed to the Michigan State University Geological Analytical Services Laboratory (East Lansing, MI) for analyses of major and trace element abundances by a combination of x-ray fluorescence, using a Bruker S4 Pioneer wavelength dispersive X-ray fluorescence (WD-XRF) spectrometer, and laser ablation, using a Micromass Platform Inductively-Coupled Plasma-Mass spectrometer (ICP-MS). Standards *RGM-1*, *W-2*, *JA-2*, and *BHVO-1* were used for calibration.

Zircon Analyses

Separation and Imaging

I separated individual zircon grains from five bulk-rock samples at Vanderbilt University following standard separation techniques, a process that included jaw-crushing and disk-pulverizing (using a type UA Bico Pulverizer); sieving pulverized material to a size smaller than 500 μm in diameter; density separation by water table (Magna Dyne® Gemini Table) and heavy liquid (*lithium heteropolytungstate* or LST); separation based on magnetic susceptibility (best recovery for zircon in non-magnetic fraction at 1.6 amps (cf. Rosenblum, 1958, and Flinter,

1959) using a Model L-1 Frantz Isodynamic magnetic separator; and lastly hand-picking individual zircon grains under a Zeiss Stemi 2000-C stereomicroscope. Approximately 1-2 kg of each sample was processed for mineral separation.

The selected zircon grains from all samples were mounted in epoxy and polished down to expose grain interiors. I then imaged them by reflected light (RL), using a Leitz petrographic microscope equipped with a Paxcam digital camera, and cathodo-luminescence (CL), using a JEOL 5600LV Scanning Electron Microscope (SEM) with custom Photo Multiplier Tube assembly, at the Stanford/USGS Micro Analysis Center (SUMAC). Zircon CL images primarily served as a guide in selecting the location of spots on individual grains for microprobe analyses using the character and diversity of zoning patterns, grain morphology, and the presence of discrete centers or cores as criteria for selection.

SHRIMP-RG Analyses

We determined trace element and U-Pb isotopic abundances of spots on individual mounted zircon grains using the SUMAC Reverse Geometry Sensitive High Resolution Ion Microprobe (SHRIMP-RG). Concentrations of a large suite of elements were measured; emphasis was placed upon Ti for thermometry (see Ti-in-zircon thermometry below), and U, Th, Hf, and the rare earth elements (REE) for evaluating magma evolution and characterizing the populations for comparison with other Icelandic and global zircons. Chips of zircon standard R33 (419 Ma) were mounted alongside our samples for calibration, and the basic operating parameters and technique employed for SHRIMP-RG elemental suite analyses and data reduction are as outlined by Claiborne *et al.* (2006). The operating microprobe beam sizes for elemental and U-Pb analyses were 15-20 μm and 35-40 μm, respectively. Zircon CL images were used as a guide in determining spot placement on each grain, and when possible multiple spots were placed on grains to discern distinctions between grain cores/interiors and rims/edges. We carried out a total of 156 trace element analyses on 118 grains, and obtained U-Pb ages for 82 spots on 81 grains (only one grain with 2 spots). Data tables containing all zircon SHRIMP U-Pb and elemental analyses can be found in appendix B.4.

Ti-In-Zircon Thermometry

The Ti-in-zircon thermometer of Ferry & Watson (2007), which uses the temperature dependence of Ti uptake in zircon to establish a quantitative relationship between Ti concentrations and temperature of crystallization, can be rearranged as

$$T(°C) = \left(\frac{-(4800 \pm 86)}{\log[Ti - in - zircon] + \log[a_{SiO_2}] - \log[a_{TiO_2}] - [5.711 \pm 0.072]}\right) - 273,$$

in which *Ti-in-zircon* is in parts per million (ppm). We use the above equation to estimate the crystallization temperature for all analyzed AIC zircon (see above section, *Zircon SHRIMP-RG Trace-Element Analyses*, on methodology for obtaining Ti concentration in zircon). Using this method, the obtained temperatures are dependent on the activities of SiO_2 (a_{SiO2}) and TiO_2 (a_{TiO2}) in the melt, which requires reasonably well-constrained activity values at the time of zircon crystallization.

Choosing accurate values for a_{SiO2} and a_{TiO2} proves to be problematic because 1) whole-rock or glass compositions may not represent the original host melts from which zircon crystallized and thus cannot be used to definitively establish these values, and 2) a_{SiO2} and a_{TiO2} are likely to vary throughout the evolution of the magma. However, a_{TiO2} can generally be restricted to >0.5 by the melt compositions and temperatures required for zircon growth (Watson and Harrison, 2005) as well as the presence of Sphene (a Ti-essential accessory phase) in AIC rocks, and since no Austurhorn rocks contain rutile it can be assumed that a_{TiO2} is <1.0. Furthermore, in a typical silicic magma a_{TiO2} usually falls between 0.6 and 0.9 at geologically relevant temperatures (Ferry and Watson, 2007; Hayden and Watson, 2007). Given these constraints, we assume a uniform value of 0.7 for a_{TiO2} in all our calculations of zircon crystallization temperatures. In addition, because zircon growth generally takes place at or near silica-saturated conditions, we assume a_{SiO2} to be 1.0.

We acknowledge that the activity of TiO_2 may, in fact, vary throughout the evolution of the magmatic system, but emphasize that the temperature variations that the Ti-in-zircon thermometer yields for our Austurhorn zircons are larger than the potential error that would be associated with a varying a_{TiO2}. We use the Ti-in-zircon thermometer with caution, and by choosing the above uniform values of a_{SiO2} and a_{TiO2} for all our calculations, we ensure that any quantitative error in our data processing is systematic, thus making our results appropriate for qualitative interpretation and yielding a reliable internal thermal variation and range of zircon crystallization temperatures within the AIC.

CHAPTER III

RESULTS

Field Observations

In describing our observations, we follow field nomenclature of Furman *et al.* (1992a) and Mattson *et al.* (1986). We recognize two types of mafic enclaves found throughout the MFCZ and adopt the terminology used by Mattson *et al*. to distinguish these: mafic pillows, which range in size from a few centimeters to meters across their long axis and are interpreted to represent melt-melt interactions, and mafic clasts, which can also range from centimeters to meters across and are interpreted to represent melt-solid interactions. Pillows commonly have cuspate or crenulate margins, sometimes chilled, or diffuse boundaries, whereas clasts typically have very sharp and angular edges (Fig. 2). In some areas, we find enclaves that are partially bound by angular edges and partially by diffuse or crenulate margins. Skialithic pillows are also present throughout the MFCZ (skiathilic pillow is defined as a “double pillow” or “pillow within a pillow,” usually a chilled dark mafic pillow surrounded by a lighter hybrid gradational, though sometimes also chilled, outer zone, all surrounded by the host silicic rock; Mattson *et al.*, 1986). Some large pillows are disaggregated into smaller enclaves at the margins.

In addition to mafic enclaves (pillows and clasts), there are large uniform bodies of fine-grained, homogeneous mafic rock within the MFCZ that have a sheet-like appearance. The edges of these sheet-like bodies are commonly seen disaggregated into mafic clasts with veins of felsic material intruding as apophyses, and in some locations we find wide areas of clast- and pillow-free felsic rock between two mafic sheets. Mafic clasts at the edges of sheets can often be put

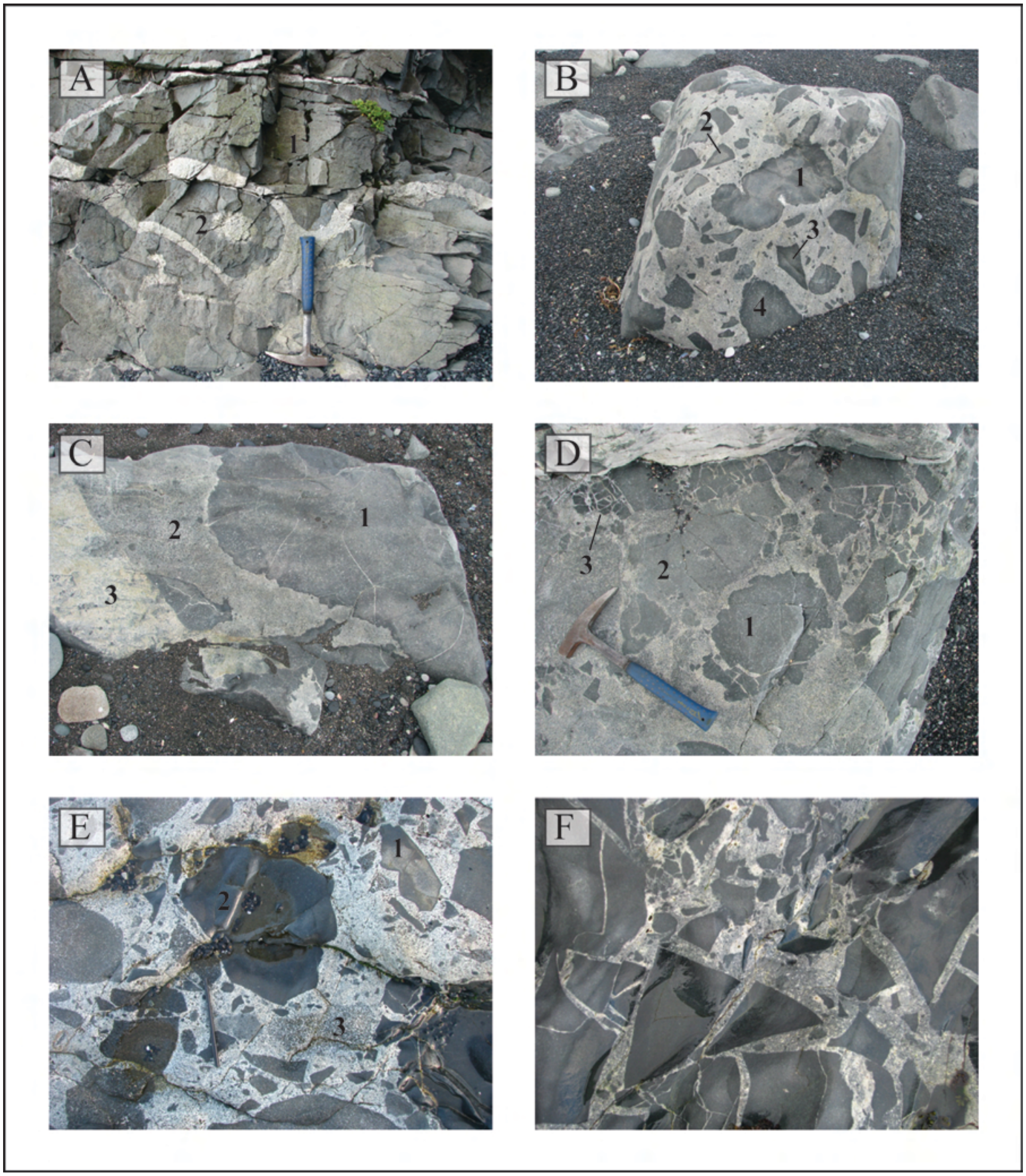

Figure 2 – Diversity of mafic enclaves found within the AIC: A) plume-like pillow structures (1, 2); B) pillow-like enclaves with chilled and crenulate margins (1, 4), and clasts with sharp and angular boundaries (2, 3); C) skialithic pillow, with dark mafic core (1) surrounded by lighter hybrid zone (2) all within a felsic host (3); D) crenulate pillows often displaying disaggregated margins (1), pillows with diffuse boundaries (2), and disaggregated clasts (3); E) pillows partly bounded by angular contacts and partly by irregular margins (1), very dark pillows with sharp irregular margins (2), and cumulate-like hybrid pillows with diffuse boundaries (3); and E) puzzle-like clasts with sharp boundaries within a lighter, hybrid matrix.

back together in a jigsaw puzzle-like manner. Furman *et al.* (1992a) also recognized the presence of these mafic sheet-like bodies within the MFCZ.

The felsic rocks in the MFCZ range in appearance from very large, homogeneous, and clast- and pillow-free bodies, to extensively mingled and mixed bodies of felsic material with abundant mafic clasts and pillows of all types and sizes, which we term *heterogeneous* units. Microenclaves with a thoroughly diffuse character (hybridized enclaves) are common in this latter type of rock (Fig. 2E-3). Felsic rocks are typically fine-grained. Some of the less silicic rocks contain a distinctively higher abundance of mafic, acicular amphibole phenocrysts and are generally clast- and pillow-free units. A particularly noteworthy exposure of felsic rock (sample locality IA-NS-4; Fig. 1) preserves evidence of felsic-felsic magma interactions in the form of two thoroughly mingled, very fine-grained felsic units (Fig. 3).

The MFCZ is surrounded by a mafic, or *gabbroic*, complex composed of the coarse-grained, layered Hvalnesfjall gabbro (sample locality IA-G-3; Fig. 1; Furman *et al.*, 1992a). A different gabbroic complex is locally exposed along the coast within the MFCZ and unlike the mafic sheets it is relatively coarse-grained and gradational with the surrounding felsic units (sample locality IA-G-1, Fig. 1). Dikes, apophyses, and thin veins of felsic rock are exposed intruded into the gabbro. We term this the *coastal* gabbro.

Petrography

All felsic samples collected display micrographic intergrowth of quartz and feldspar, with individual large feldspar crystals and crystalline quartz also present and common in the same matrix. We thus use the term “granophyre” rather than “granite” to describe these more evolved

Figure 3 – Texture interpreted as preserved felsic-felsic magmatic interactions at outcrop IA-NS-4.

felsic units found within the MFCZ. Sample IA-NS-4B (very fine-grained homogeneous granophyre) contains the best-developed micrographic texture and is composed of ~98-99% intergrown quartz and feldspar. It also contains small patches of microcrystalline quartz. Minor amounts of fresh, prismatic clinopyroxene (CPX), which we interpret as a primary magmatic phase, and amphibole are present in most felsic samples. A large portion of amphibole crystals are fibrous in texture and usually occur as rims surrounding primary CPX cores. We interpret these to be a secondary phase resulting from subsolidus hydrothermal alteration of CPX. Zircon and sphene are common accessory phases in all felsic units as well as two of the mafic samples.

Sample IA-NS-2 (heterogeneous granophyre) contains abundant microenclaves with diffuse boundaries, abundant CPX phenocrysts, and a plagioclase microlite groundmass.

All mafic samples have similar mineral assemblages, composed mainly of very coarse plagioclase, CPX, Fe-Ti oxides, and minor amounts of biotite. Amphibole is also present, though often mainly as a secondary phase from the alteration of CPX. Some of the Fe-Ti oxides from the coastal gabbro (sample IA-G-1) display an acicular habit that is absent in the other gabbros. The Hvalnesfjall gabbro (sample IA-G-3) is the coarsest sample and also displays the least amount of alteration. Most samples display a significant amount of subsolidus alteration, and secondary phases such as epidote, chlorite, and calcite are present in all units. A summary of the AIC petrography is found in Table 1. Representative photomicrographs can be found in appendix C.

Whole-Rock Geochemistry

We obtained whole-rock major oxide and trace element abundances from 11 representative samples in order to characterize the rock types found within the AIC. Of the 11 samples, 9 encompass the range of felsic textures and compositions we found in the granophyre zone and within the MFCZ while the other two represent the gabbroic complex surrounding the MFCZ. Full whole-rock geochemical data for all AIC samples are presented in appendix B.

Major Oxides

Major oxides in the felsic samples display typical trends in Harker plots, showing a general increase in K_2O and decrease in TiO_2, Al_2O_3, Fe_2O_3, MnO, MgO, CaO and P_2O_5 with increasing SiO_2 content (Fig. 4). SiO_2 concentrations range from 61 to 78 wt.% for the felsic

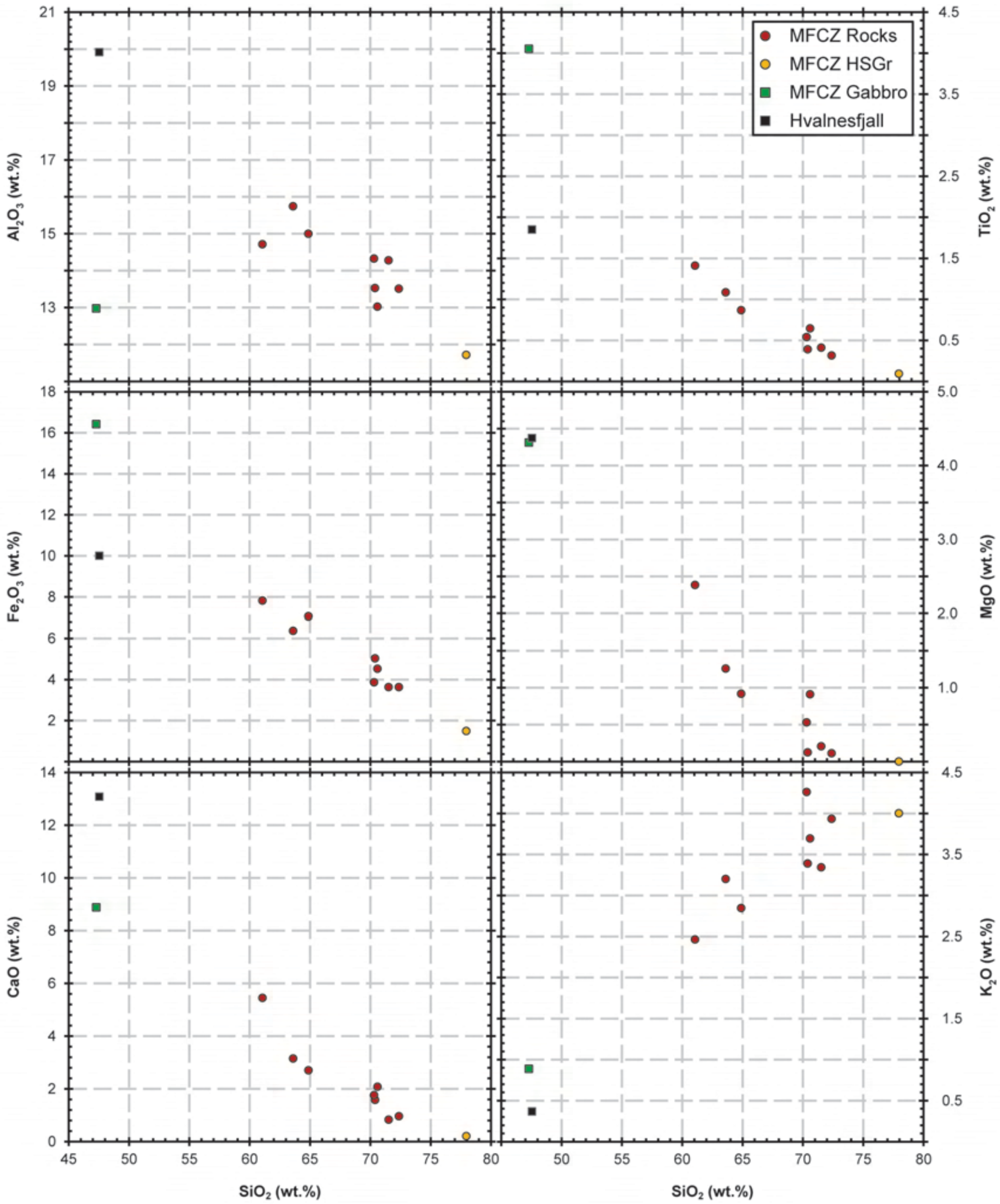

Figure 4 – Austurhorn intrusive complex whole-rock major oxide geochemistry.

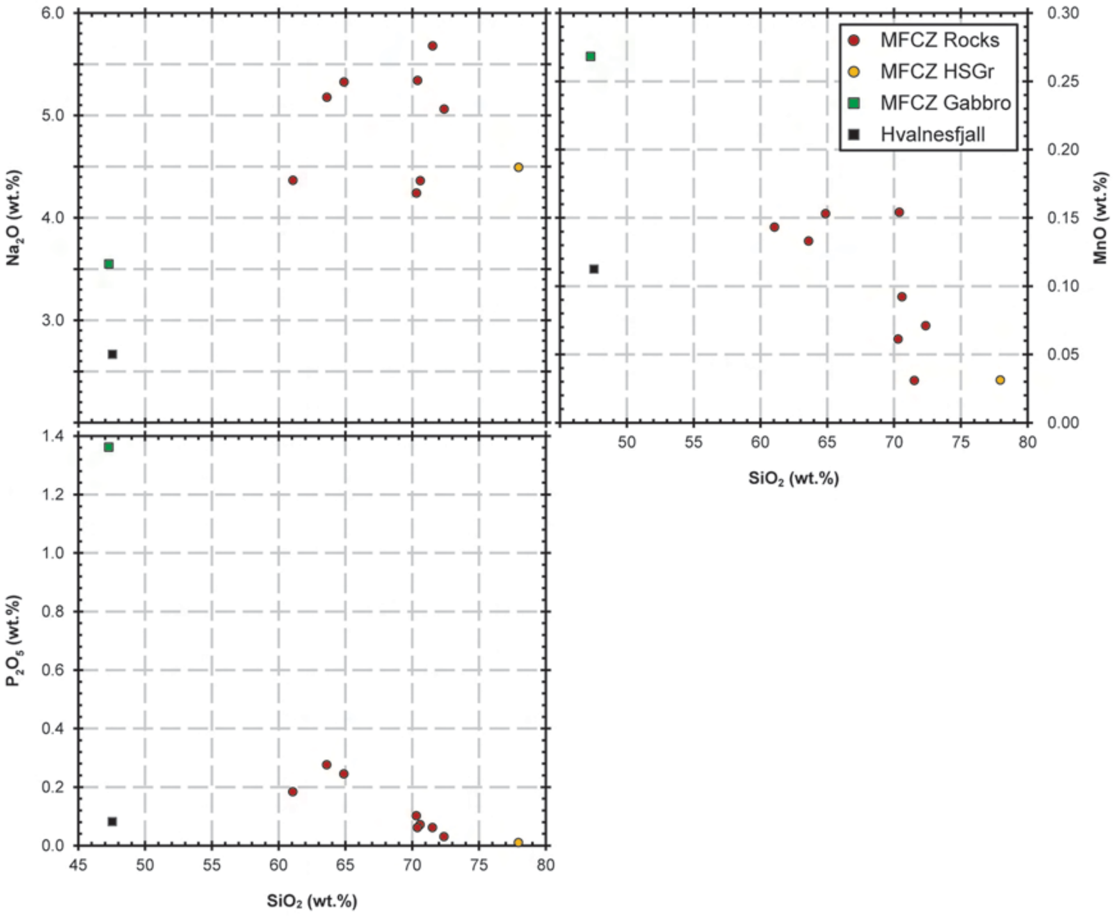

Figure 4 (continued) – Austurhorn intrusive complex whole-rock major oxide geochemistry.

samples, and the mafic samples are both near 47 wt.%. All AIC samples are tholeiitic and metaluminous (Furman *et al.*, 1992a; 1992b).

The two mafic samples differ significantly from each other in their major oxide abundances. Sample IA-G-3 (Hvalnesfjall gabbro) generally contains much lower TiO_2, Fe_2O_3, K_2O, Na_2O, MnO, and P_2O_5 abundances, and higher Al_2O_3 and CaO than the coastal gabbro (sample IA-G-1), though their MgO abundance is essentially the same.

Rare Earth Elements (REE)

With the exception of the highest-Si granophyre (IA-NS-4B), all intermediate to felsic AIC samples display LREE-enriched REE patterns with negative Eu anomalies (Fig. 5). Compared to typical felsic igneous rocks of continents and island arcs, these samples have relatively high REE concentrations (similar to A-type granites). Most also have a small but discernible positive Ce anomaly. Sample IA-NS-4B displays a flat chondrite-normalized pattern except for a strong negative Eu anomaly and an extremely large positive Ce anomaly.

Both gabbro samples are also relatively LREE-enriched, but they have lower REE concentrations than the intermediate to felsic samples. Sample IA-G-1, from the coastal gabbro, displays slightly elevated MREE concentrations and lacks discernible Eu or Ce anomalies. The Hvalnesfjall gabbro (IA-G-3) has much lower REE than IA-G-1 and displays a noticeable positive Eu anomaly.

Other Trace Elements

Whole-rock trace element abundances within the AIC generally display expectable trends when plotted against one another or against SiO_2. For example, Sr concentrations fall as rock compositions become silicic (consistent with its compatibility with feldspars), Zr and Hf generally increase as SiO_2 and other indicators of magma evolution rise but fall in the most evolved samples (consequence of zircon saturation), Ba follows a similar trend (apparent response to late saturation in alkali feldspar), and U, Th, and Rb appear to behave incompatibility throughout, except that they are slightly lower in the most silicic sample, granophyre IA-NS-4B.

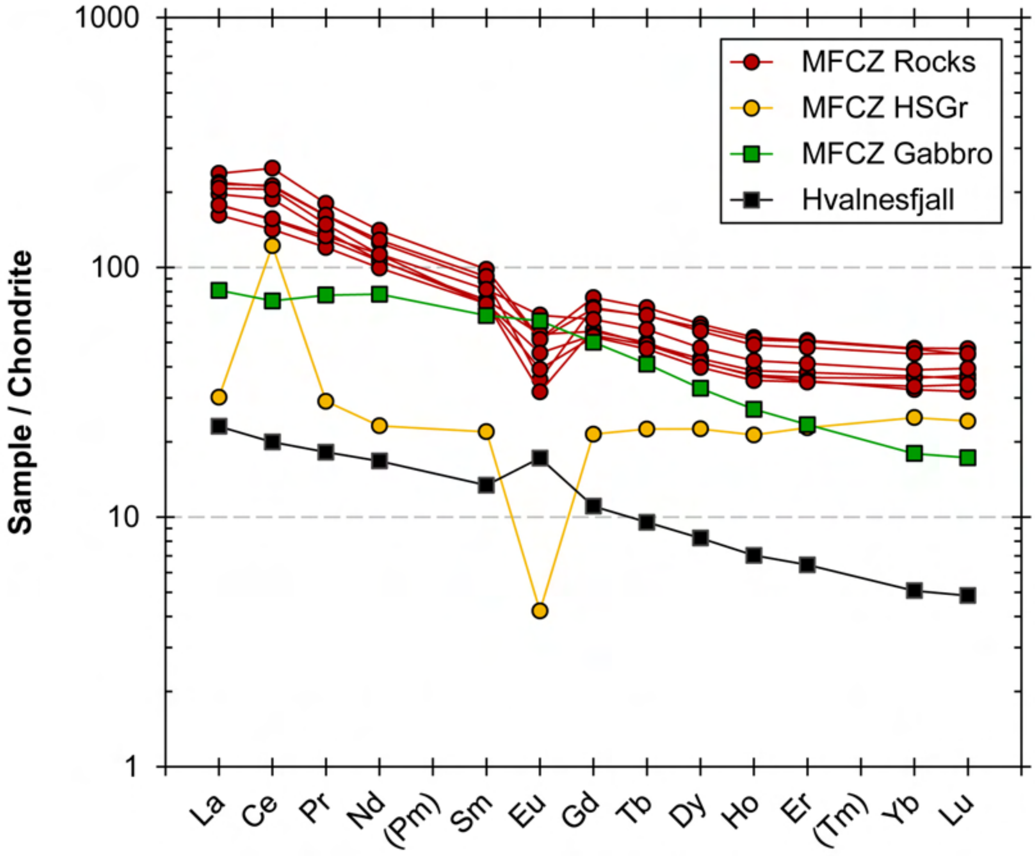

Figure 5 – Austurhorn intrusive complex whole-rock rare earth element geochemistry.

Zircon Results: Morphology, Elemental Compositions, U-Pb Ages

Samples Investigated

We extracted zircon from five samples for SHRIMP elemental analyses. The four felsic samples encompass the range of textures and rock-types found within the MFCZ: a heterogeneous granophyre (IA-NS-2) that contains all mafic-clast types and displays extensive hybridization between mafic input and felsic host; a homogeneous fine-grained and clast-free high-Si granophyre (IA-NS-4B) that displays extensive felsic-felsic melt interactions; a homogeneous, fine-grained diorite (IA-NS-6) that hosts abundant mafic enclaves (large, diffuse pillows, as well as smaller angular clasts); and a homogeneous, medium-grained and enclave-free micrographic granodiorite (IA-NS-7) characterized by abundant acicular amphibole phenocrysts. The selected mafic sample is IA-G-1, the homogeneous, relatively coarse-grained gabbro from the coastal gabbroic complex within the MFCZ.

Zoning and Morphology

In contrast to zircon extracted from Icelandic volcanic rocks (Carley *et al*., 2011), zircon grains from the AIC are typically larger with more distinct and complex zoning. Zoning patterns range from complex oscillatory, to patchy, striped, sector, and simple zoning. Crystals are dominantly euhedral and prismatic, often acicular or subequant, though slightly rounded grains are also present in all samples (see Figs. 6-8). A small number of grains preserve evidence of resorption and re-crystallization events in the form of anhedrally-shaped cores surrounded by prismatic zircon overgrowth.

Granophyres (samples IA-NS-2 and IA-NS-4B) have the highest abundance of euhedral and oscillatory-zoned crystals, although a small proportion of grains from sample NS-2 contain broad zoning and resemble zircon grains from Icelandic volcanic rocks (see Fig. 6). Additionally, a large group of grains from sample NS-4B are zoned in a convolute pattern and appear to have "spongy" or porous texture (Fig. 6b). These zircon crystals belong to sample group NS-4Bb, which are highly enriched in Hf (see *Trace Elements* section under *Zircon Elemental Geochemical Analyses* above).

Crystals in the intermediate samples (IA-NS-6 and IA-NS-7) display the greatest amount of rounding and resorption, and a large proportion of grains from the diorite sample (NS-6) are anhedral (see Fig. 7).

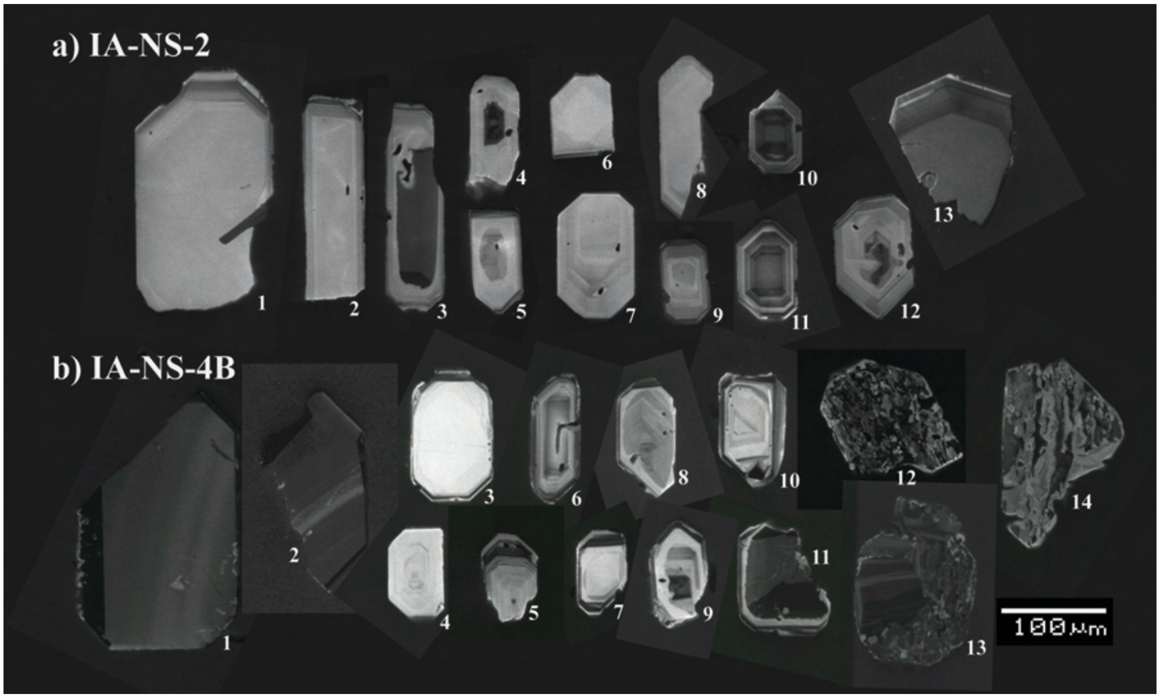

Figure 6 – Scanning electron microscope cathodoluminescence (CL) images of zircon from the Austurhorn granophyre (a) and high-Si granophyre (b). a) Zircon morphologies in sample IA-NS-2 include large euhedral (1, 13), small euhedral (5-12), acicular (1-2), and slightly rounded (3-4) grains, while zoning ranges from simple and broad (1-2, 6-9, 13) to oscillatory (10-11), and some grains contain anhedrally-shaped cores surrounded by zircon overgrowth (3-5, 12). B) Zircon morphologies in sample IA-NS-4B also include large euhedral (1-3), small euhedral (4-10), slightly rounded (8, 11), and zoning ranges from simple and broad (1-4, 11) to oscillatory (5-10). A large population of grains in this sample display *convolute* zoning (12-14).

Zircons from the gabbro (IA-G-1) are significantly larger than those from felsic samples, and display the greatest diversity of internal patterns, ranging from oscillatory, sector-, striped, and patchy zoning, to unzoned homogeneous interiors, and "spongy" textures (see Fig. 8).

General Elemental Characteristics

The elemental compositions of our AIC zircons generally form a broad but coherent array and fall within the fields established by Carley *et al.* (2011) for silicic volcanic rocks of Iceland (Figs. 10, 12-13). This field is enclosed within a much larger field that spans the compositions of zircons from volcanic and plutonic rocks from continents (subduction arcs and extension zones) (Carley *et al.*, 2011; Grimes *et al.*, 2007). A few analyses from IA-NS-2 (granophyre) and many

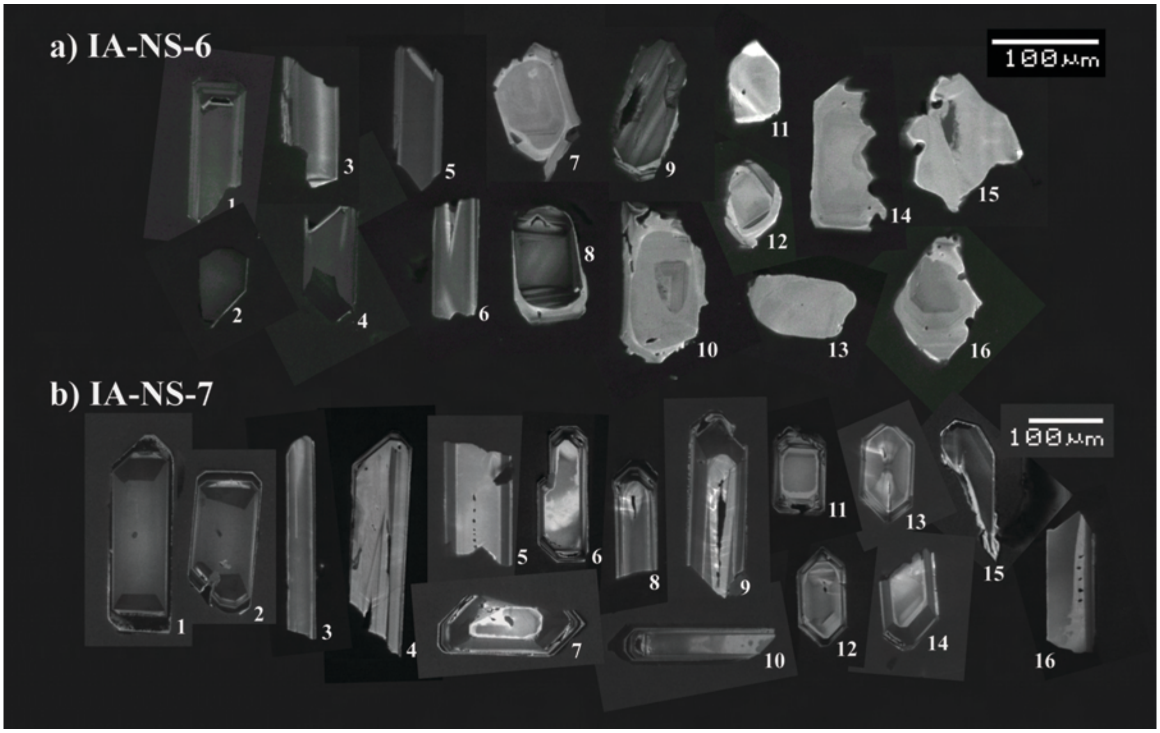

Figure 7 – Scanning electron microscope cathodoluminescence (CL) images of zircon from the Austurhorn diorite (a) and granodiorite (b). a) Zircon morphologies in sample IA-NS-6 are dominated by acicular (1-6), rounded (7-9, 11-13), and anhedral grains (10, 14-16). Zoning patterns range from simple (14-15), broad (1-2), and striped (3, 5-6), to oscillatory (10, 12, 16), sector-zoned (4), and even relatively unzoned (13). Grains containing anhedrally-shaped cores surrounded by zircon overgrowth are common (7-10,12), and some contain multiple anhedral zones (10). B) Zircon morphologies in sample IA-NS-7 mostly include acicular (1-10, 16) and small euhedral grains (11-14), but some with resorbed and rounded edges are found (5-6, 11, 15). Zoning patterns range from sector-zoning (1-2), to simple and broad (3-4, 16), striped (5), and oscillatory (6-15).

analyses from IA-NS-4B (high-Si granophyre) fall outside of this field, distinguished primarily by higher Hf. The full zircon elemental data suite can be found in appendix B.5.

Rare Earth Elements (REEs)

With notable exceptions (see below), all zircons from the AIC contain REE abundances that are within the typical range for silicic rocks (Carley *et al*., 2011; Grimes *et al*., 2007), displaying chondrite-normalized trends of extreme enrichment in heavy rare Earth elements (HREE)

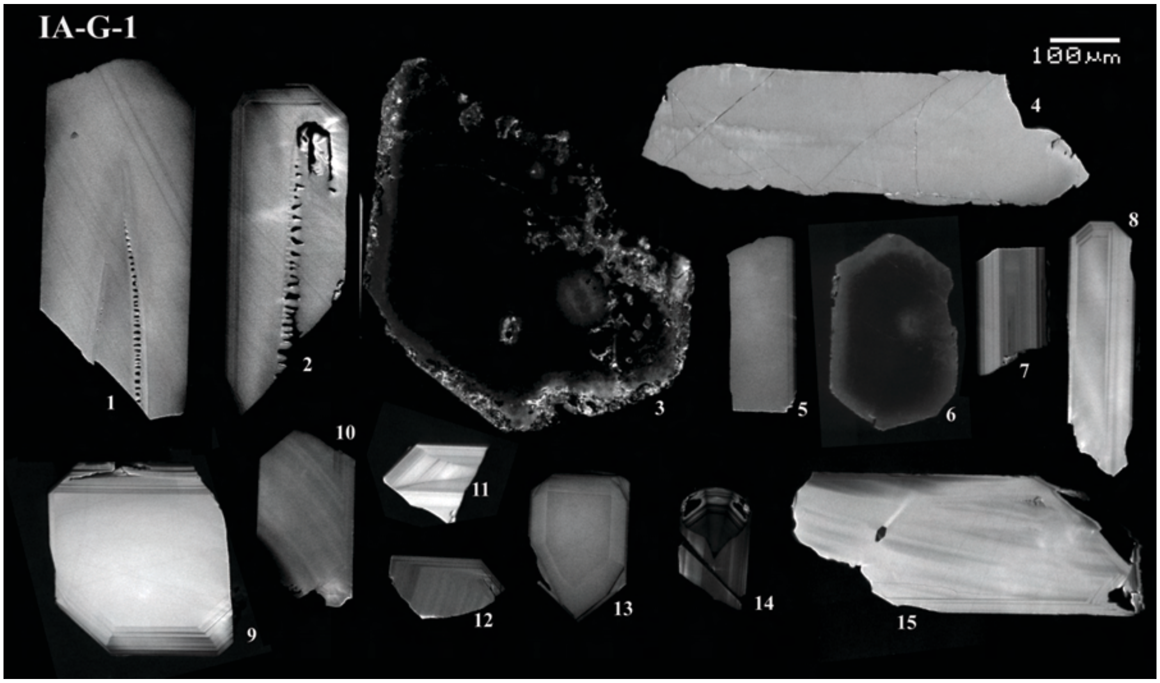

Figure 8 – Scanning electron microscope cathodoluminescence (CL) images of zircon from the Austurhorn coastal gabbro. Zircon grains in sample IA-G-1 are generally larger than those found in intermediate and silicic samples, and their morphologies range from acicular (1-2, 4-5, 7-8), to euhedral (3, 6, 9-14), and rounded and resorbed (3-6, 15). Zoning patterns include simple (1-2, 10), broad (13), striped (7), sector-zoned (14), oscillatory (8-9, 11, 14), patchy (15), diffuse (3, 6), and unzoned (4-5). Some grains display porous texture and higher levels of resorption (3).

relative to light rare Earth elements (LREE) and strong positive Ce and negative Eu anomalies (Fig. 9).

Three zircon grains from sample IA-NS-2 and one from IA-NS-6 show distinct LREE enrichment. Zircon from samples IA-NS-4B and IA-NS-7 can be divided into two coherent groups based on some of their trace element characteristics.

We distinguish two zircon groups in sample IA-NS-4B based primarily on their Hf content (see below). Group NS-4Ba (normal-Hf) displays the typical silicic trend described above and has a characteristically smaller Eu anomaly. Two grains in this group contain elevated LREE concentrations. Group NS-4Bb (Hf-enriched) also displays a typical trend, though with a greater range in concentrations and a characteristically larger Eu anomaly.

Sample IA-NS-7 can be split into groups NS-7a and NS-7b based on REE abundances. Group NS-7a generally has higher REE abundances, a smaller Ce anomaly, and a larger Eu anomaly, whereas group NS-7b generally has lower REE abundances, a larger Ce anomaly, and a smaller Eu anomaly.

Other Trace Elements

Generally, zircons from all samples contain U, Th, and Hf abundances that are consistent with the typical range for zircon from silicic rocks (Carley *et al.*, 2011). The exceptions are sample groups NS-4Bb and NS-7a: zircons from group IA-NS-4Bb are highly enriched in Hf (up to 24,000 ppm, much higher than any other analyzed Icelandic zircon, which are characteristically low in Hf - Carley *et al.*, 2011) and contain elevated U and Th concentrations, and zircons from group IA-NS-7a contain elevated U and Th abundances. Most grains display core-to-rim increase in Hf concentration.

Ti Temperature

Our estimates of crystallization temperature, based on Ti abundance in zircon, yield a range of ~730-870 °C (5.6-24.6 ppm Ti) for most zircons, with a few analyses from all samples falling outside of this range (Fig. 10). Zircons from sample group IA-NS-4Bb (Hf-enriched) are depleted in Ti and thus have a distinctly lower temperature range of mostly 630-760 °C (1.9-7.6 ppm Ti). In general, crystallization temperatures decrease with increasing Hf-concentrations, a trend most noticeable in sample IA-G-1.

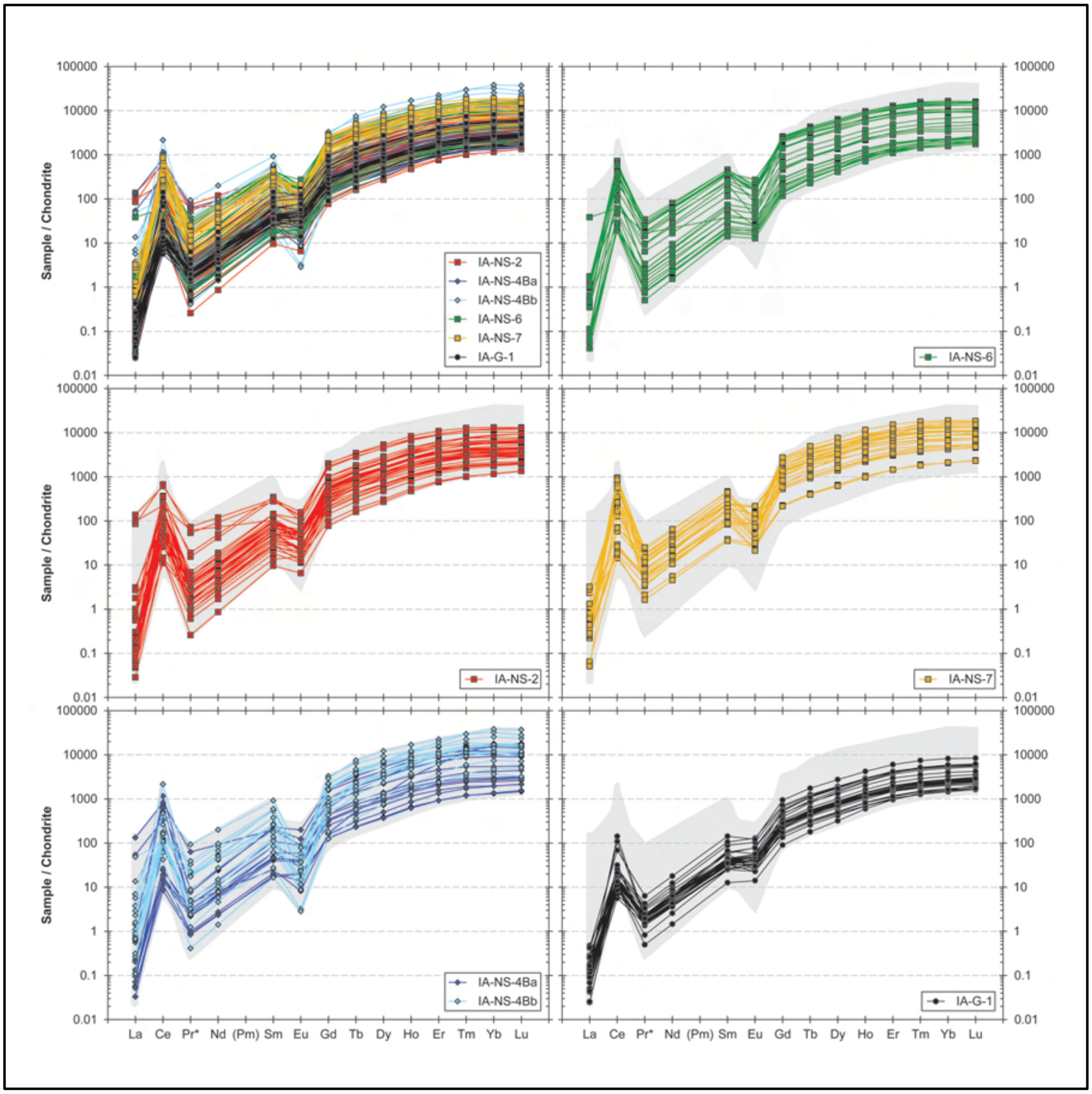

Figure 9 – Zircon rare earth element geochemistry. Grey shadow in individual sample plots represents the range of REE abundances found within Austurhorn plutonic zircons.

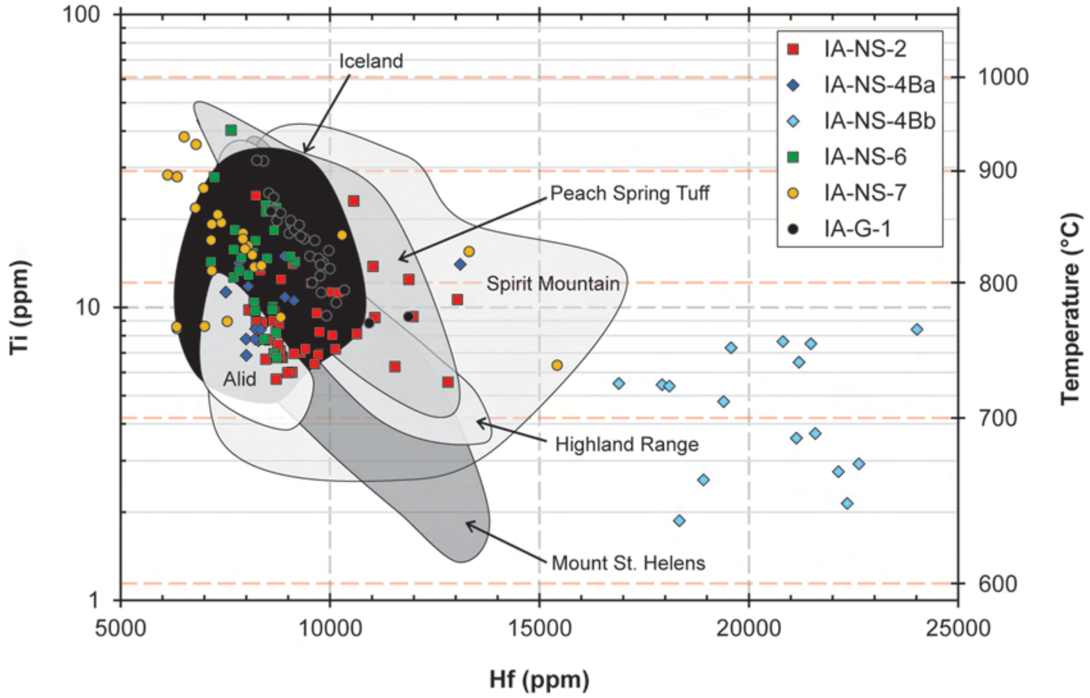

Figure 10 –Hf vs. Ti abundances in AIC zircon (modified after Carley *et al*., 2011). Shaded areas represent zircon geochemistry ranges for respective tectonic settings (labeled); zircon crystallization temperatures calculated using the Ti-in-quartz thermometer of Ferry & Watson, 2007, using an a_{TiO2} value of 0.7. While most AIC zircon fall within the coherent low-Hf Iceland field, a group of hydrothermal-like grains from the high-Si granophyre, labeled IA-NS-4Bb, fall well outside this field with elevated Hf and generally lower Ti.

U-Pb Geochronology

We obtained U and Pb data from all zircon samples in order to estimate the ^{206}Pb/^{238}U age of the MFCZ. All samples yielded reliable ages with few rejections, and the mean ages, corrected for common lead (^{207}Pb), range from 6.26±0.10 (MSWD = 3.23) to 6.54±0.07 Ma (MSWD = 0.98) for the intermediate to felsic samples while the gabbro, IA-G-1, gives a mean age of 5.99±0.10 Ma (MSWD = 0.64) (Table 2). The ages from all samples can be grouped into two coherent populations, which record mean ages of 6.45 ± 0.04 Ma (MSWD = 1.3) and 5.99 ± 0.06 Ma (MSWD = 1.17) (Fig. 11). With the exception of a few analyses from the gabbro, all ages in the older population are from zircon in intermediate to felsic rocks, whereas the younger population contains all but a few gabbro analyses and approximately one third of all ages from zircon in intermediate to felsic rocks. A detailed summary of all ages can be found in appendix B.4.

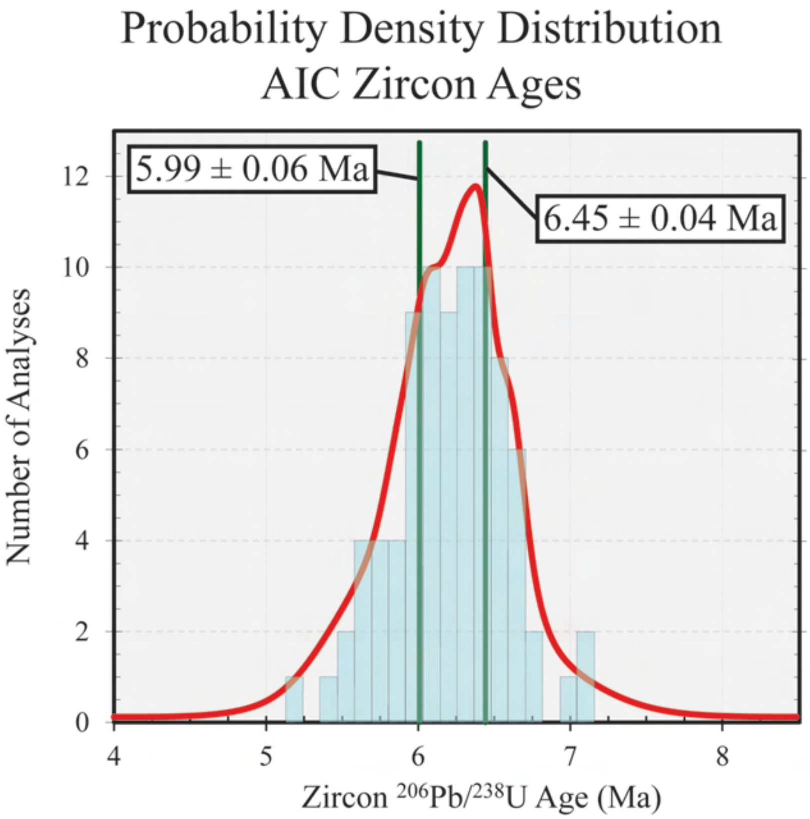

Figure 11 –Probability density distribution for zircon ages from the Austurhorn Intrusive Complex. Two coherent age populations are identified at 6.45 ± 0.04 Ma (MSWD = 1.3) and 5.99 ± 0.06 Ma (MSWD = 1.17). While zircons from the coastal gabbro (sample IA-G-1) alone yield a mean age of 5.99 Ma, approximately one third of zircon from intermediate to silicic samples fall within the same younger age population as zircons from the coastal gabbro.

Table 2

AUSTURHORN INTRUSIVE COMPLEX
Zircon $^{206}Pb/^{238}U$ Ages (corrected for common lead, ^{207}Pb)

Sample	Rock Type	No. of Grains	MSWD	Mean $^{206}Pb/^{238}U$ Age (Ma)	± (1s)
IA-NS-2	Granophyre	10	1.73	6.37	0.10
IA-NS-4B	Granophyre	14	0.98	6.54	0.07
IA-NS-6	Diorite	13	0.84	6.28	0.08
IA-NS-7	Granodiorite	15	3.23	6.26	0.10
IA-G-1	Gabbro	16	0.64	5.99	0.10
Ages of Intrusion of the MFCZ:					
Group A	--	41	1.17	**5.987**	0.06
Group B	--	42	1.3	**6.449**	0.044

CHAPTER IV

DISCUSSION

Zircon Abundance, Size, and Morphology

In a pilot study, Carley *et al.* (2009; 2011) demonstrated that zircons from silicic volcanic rocks from Holocene Icelandic eruptions record relatively brief, high-temperature histories. Like most silicic rocks in Iceland, these volcanic rocks are rich in Zr, and yet zircon is extremely sparse. In contrast, we have found that both mafic and silicic rocks from the mafic-felsic composite zone at the Austurhorn Intrusive Complex contain a vastly greater abundance of zircon, suggesting that most zircon in Iceland may be stored and preserved within rocks from silicic plutonic complexes.

Zircon crystals from the AIC are generally larger than the volcanic crystals investigated by Carley et al. (2009; 2011), and they display more distinct and complex zoning (see Figs. 6-8). These differences likely reflect slow and full crystallization of their parent magmas, down to the solidus, in intrusive complexes, whereas silicic volcanic rocks are crystal-poor and are most likely to have erupted at temperatures near to or above zircon saturation (Carley *et al*., 2011).

Although grain zoning and morphology are widely varied throughout the MFCZ samples, oscillatory-zoned euhedral grains, which are considered to be characteristic of igneous growth under a high degree of zircon-saturation (Hoskin & Schaltegger, 2003), are common in zircon from all MFCZ rock types. Crystals with large aspect ratios and acicular habit, as well as sector- and broad zoning, are also common in all samples. These features typically represent rapid crystallization of zircon (Hoskin & Schaltegger, 2003; Hanchar & Miller, 1993), commonly in volcanic environments.

A significant number of grains preserve evidence of resorption and recrystallization events in the form of anhedrally-shaped cores with truncated internal zoning surrounded by prismatic zircon overgrowth (Fig. 7). These features reflect zircon-undersaturated conditions in the melt from which the zircons were crystallizing (Hoskin & Schaltegger, 2003; Corfu *et al.*, 2003). Such conditions likely represent thermal and chemical fluctuations of the melt within an open system that mark repeated stages of mafic-felsic magma interactions and mafic magma replenishment and recharge into the felsic pluton throughout the history of the complex.

Zircon Elemental Compositions

The elemental compositions of plutonic zircon at Austurhorn form a broad and coherent geochemical array with a trend consistent with fractional crystallization, from high-temperature down to the low-pressure wet solidus. Following the work of Grimes *et al.* (2007), Carley *et al.* (2011) established geochemical fields for zircon formed in silicic rocks from a range of continental settings in other tectonic environments, based on the abundance of Hf, U, Yb, and Ti in zircon (see Figs. 10 and 12). Despite crystallizing in a mid-oceanic ridge setting, the Austurhorn zircon array mostly falls within the low-Hf and low-U/Yb section of the silicic field (Fig 13; Carley *et al*., 2011). With some exceptions, rare Earth element (REE) patterns for Austurhorn zircon are also consistent with those of silicic rocks, displaying

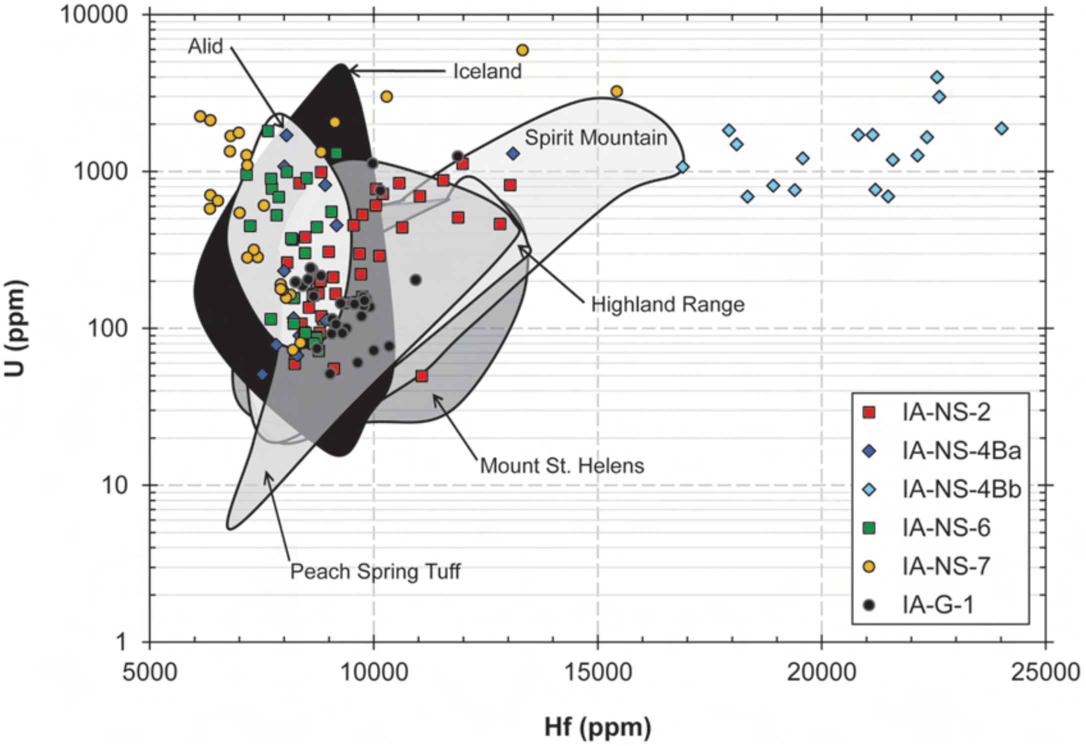

Figure 12 –Hf vs. U abundances in AIC zircon (modified after Carley *et al*., 2011). Shaded areas represent zircon geochemistry ranges for respective tectonic settings (labeled); While most AIC zircon fall within the coherent low-Hf Iceland field, a group of hydrothermal-like grains from the high-Si granophyre, labeled IA-NS-4Bb, fall well outside this field with elevated Hf and generally higher U.

extreme HREE enrichment relative to LREE and strong positive Ce and negative Eu anomalies.

Temperature estimates (based on Ti-in-zircon thermometer of Ferry and Watson, 2007, with an assumed $a_{TiO2} = 0.7$) are generally consistent with those in the Icelandic silicic volcanic field, ranging from ~730 to 870°C. Similarly, U concentrations in Austurhorn zircons are consistent with those in continental silicic rocks, ranging mainly from 50 to 1000 ppm U, and Hf concentrations, though they fall within the silicic field, are mostly restricted to the low end of the range at 6000 to 10000 ppm Hf.

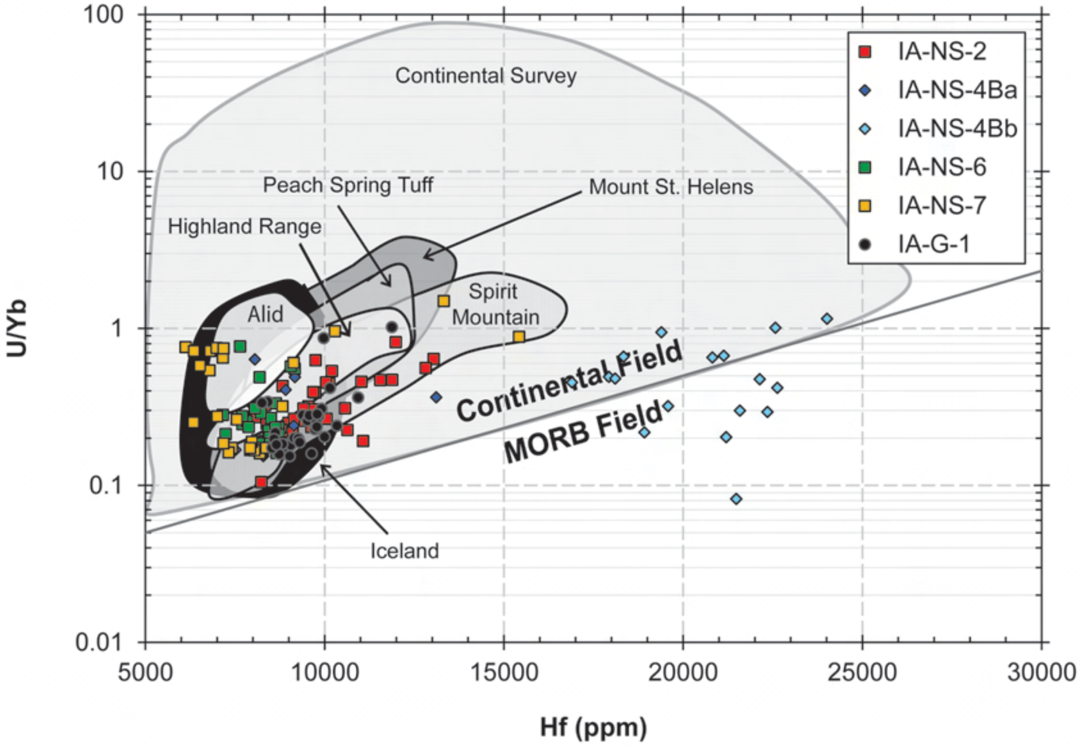

Figure 13 –Hf abundances vs. U/Yb in AIC zircon (modified after Carley *et al*., 2011). Shaded areas represent zircon geochemistry ranges for respective tectonic settings (labeled); Despite forming in an oceanic setting, most AIC zircon fall within the continental field described by Grimes *et al.* (2007), with the exception of the higher-Hf hydrothermal-like grains from the high-Si granophyre, labeled IA-NS-4Bb.

The exception among AIS zircon compositions to the generalizations described above is a group of grains from the high-Si granophyre (sample IA-NS-4B, ~78 wt.% SiO_2), which we have designated as zircon group NS-4Bb. The high-Si granophyre is composed of 98-99% quartz and feldspar, and some zones of extensive mingling within the outcrop preserve evidence for felsic-felsic melt interactions, perhaps reflecting late-stage or subsolidus processes (e.g. hydrothermal activity). Titanium concentrations within zircon from this group indicate a lower crystallization temperature range than those of most Austurhorn zircon, at ~635-765°C (see Fig. 10). The analyses were mostly from CL-dark, “spongy” or convolute zones that are rich in U and Th, poor in Ti, generally display elevated REE concentrations, and contain much higher Hf than any other analyzed Icelandic zircon (group NS-4Bb was defined as spots with abundance of Hf >15000 ppm). Corfu *et al*. (2003) attribute "spongy" texture and significant enrichment in elements such as Hf, U, and Th and REE, to crystallization (or re-crystallization) from low-pressure, relatively low-temperature aqueous fluids. Thus, these zones may represent near- or subsolidus processes such as hydrothermal episodes of growth or local re-crystallization (*cf* Grimes *et al.*, 2009; Corfu *et al.*, 2003; Hoskin & Schaltegger, 2003), likely due to the shallow emplacement of plutonic complexes in the Icelandic crust.

In addition to zircon from group NS-4Bb, a number of CL-dark zircon analyses from other felsic rock samples also display LREE enrichment (see Fig. 9), but they lack the "spongy" textures or convolute zoning pattern present in NS-4Bb grains, perhaps reflecting a much lower degree of hydrothermal influence on late-stage melts than in the high-Si granophyre or a relatively higher amount of contamination by LREE-rich inclusions. With the exception of the LREE enrichment, all other trace element abundances in these zircons are consistent with the AIC magmatic zircon array (excluding zircon from the sample group NS-4Bb).

U-Pb Geochronology

The range of mean ages we obtained from zircons for the intermediate to felsic samples (diorite, granodiorite, and granophyres; 6.26-6.54 Ma) differ from that of the gabbro by 0.27-0.55 m.y. (5.99 Ma) (see Table 2). Zircon ages in intermediate to felsic rocks span 1.4 Ma (mainly from ~5.6 to ~7.0 Ma). The data permit the interpretation that zircon growth was continuous throughout the evolution and lifespan of the AIC magmatic system. This timescale is consistent with a model in which the longevity of a magmatic system is prolonged by the repeated input of younger and hotter mafic magmas into the system (*cf* Claiborne *et al.*, 2010a). However, all ages (from mafic, intermediate, and felsic) can be grouped into two coherent age populations at 6.45 ± 0.04 Ma (MSWD = 1.3) and 5.99 ± 0.06 Ma (MSWD = 1.17) (Fig. 11). The older population is dominantly composed of zircons in intermediate to felsic rocks, with few analyses coming from the coastal gabbro, and thus we interpret the older age (6.45 Ma) to represent the emplacement of the MFCZ. Since the gabbro alone gives a mean age of 5.99 Ma, the younger population, which includes one third of zircons in intermediate to felsic rocks, likely reflects a major episode of mafic magma replenishment. This episode generated the coastal gabbro and may have partially remobilized felsic material within the MFCZ magma reservoir with attendant growth of a second generation of zircon. The MFCZ was probably nearly and possibly entirely solid at the time of gabbro intrusion, but field evidence suggests magmatic interactions between the coastal gabbro and the felsic rocks with which it is associated. Our established $^{206}Pb/^{238}U$-age of intrusion for the MFCZ, at 6.45 ± 0.04 Ma, is consistent with a previously published K-Ar age of 6.6 ± 0.4 Ma for the Austurhorn Intrusive Complex (Moorbath *et al.*, 1968).

CHAPTER V

CONCLUSIONS

With this study, we present the first physical and geochemical characterization of what is likely Iceland's dominant zircon population: plutonic zircon.

In comparison to Iceland's silicic volcanic rocks, both mafic and silicic rocks from the mafic-felsic composite zone at the Austurhorn Intrusive Complex contain a vastly greater abundance of zircon. These plutonic zircons are generally larger and display more distinct and complex zoning than volcanic zircon. These differences likely reflect full crystallization of parent magmas, down to the solidus, in intrusive complexes, whereas silicic volcanics are crystal-poor and likely erupted at temperatures above zircon saturation. Though grain morphology is varied, oscillatory-zoned euhedral grains are common in all samples. A large number of zircon grains retain evidence, as cores that we interpret to be antecrystic, for thermal and chemical fluctuations that mark repeated mafic-felsic magma interactions in the history of the complex.

With the exception of hydrothermal-like zircon from sample group IA-NS-4Bb, the elemental compositions of plutonic zircon at Austurhorn form a broad and coherent array with a trend consistent with fractional crystallization, from high-temperature down to the low-pressure wet solidus. This array falls within falls primarily within the field established by Carley *et al.* (2011) for zircon from silicic volcanic rocks of Iceland, which represents a low-Hf portion of the larger field of zircon from continental settings in other parts of the world. Zircons from group

NS-4Bb likely represent subsolidus processes such as hydrothermal re-crystallization of MFCZ zircon.

Based on our results, we establish the age of intrusion of the MFCZ at 6.45 ± 0.04 Ma (consistent with a previously published K-Ar age of 6.6 ± 0.4 Ma for the Austurhorn Intrusive Complex (Moorbath *et al.*, 1968)). Furthermore, a younger population of zircon from the MFCZ, which includes one third of zircon from intermediate to felsic rocks and essentially all zircons from the gabbro, records a major event of mafic magma replenishment into the MFCZ at 5.99 ± 0.06 Ma, which generated the coastal gabbroic complex and partially remobilized the MFCZ.

PART II

The Highland Range Silicic Volcanic Sequence, southern Nevada

CHAPTER I

INTRODUCTION

The northern Colorado River Extensional Corridor (CREC) has been a site of extensive research on felsic plutonic and volcanic systems in recent years (Olson *et al.*, 1999; Bachl *et al.*, 2001; Faulds *et al.*, 2002; Miller & Miller, 2002; Claiborne *et al.*, 2006; Miller *et al.*, 2007; Walker *et al.*, 2007; Colombini, 2009; others), and many exposed volcanic rocks display potential links to felsic plutons within the area. It has been proposed that much of the Highland Range sequence erupted from the Searchlight system (e.g. Colombini *et al*., 2008; Colombini, 2009; Faulds *et al*., 2001, 2002b; Miller *et al*., 2007). Composite andesite dikes and rhyolite intrusions, as well as mingled rhyolitic lavas with mafic enclaves, and a transition from silicic to intermediate volcanism, may represent the last eruptive stage of a silicic magma system (in this case, presumably that of Searchlight pluton). This site presents a great opportunity to investigate and gain a better understanding of the processes that mingle compositionally differing magmas as well as the processes that terminate silicic magmatism, and to investigate relationships between the volcanic units present at this locality and units from Searchlight pluton.

Geologic Setting: The Highland Range, southern Nevada

The northern Colorado River Extensional Corridor (CREC), a 50-100 km wide region of moderate to large-magnitude crustal extension along the eastern margin of the Basin and Range province in the southwestern USA (Nevada, California, Arizona), has been a site of extended research on felsic plutonic and volcanic systems (e.g. Olson *et al.*, 1999; Bachl *et al.*, 2001; Faulds *et al.*, 2002; Miller & Miller, 2002; Claiborne *et al.*, 2006; Miller *et al.*, 2007; Walker *et al.*, 2007; Colombini, 2009; Colombini *et al.*, in press). Voluminous magmatism in the region, manifested as both intrusive and extrusive sequences that range from mafic to felsic in composition, began around ~18 Ma and terminated at ~8 Ma (e.g. Feuerbach 1998; Larsen and Smith 1990; Metcalf et al., 1995; Faulds et al., 1995; Miller and Miller, 2002; Metcalf, 2004; Walker et al., 2007).

Domino-style rotation of large fault blocks during CREC regional extension exposed thick crustal sections, including intrusive and extrusive felsic sequences that are interpreted to be parts of the same magmatic system (e.g. Honn and Smith 2008; Faulds et al., 2001; Metcalf, 2004). In particular, it has been proposed that much of the volcanic rock sequence exposed in the Highland Range (HR) and adjacent northern Newberry Mountains erupted from the nearby Searchlight pluton (SLP) system (Fig 14), correlated on the basis of proximity, ages, and lithologic sequence (Fig. 15; e.g. Ruppert and Faulds 1998; Faulds, 1999; Faulds *et al.*, 2001, 2002b; Bachl et al., 2001; Miller *et al.*, 2007; Colombini, 2009; Colombini *et al.*, 2008, 2011). The volcanic sequence here is an extension of the Miocene section exposed in the nearby Eldorado Mountains, the base of base of which is intruded by the SLP (Bachl *et al.*, 2001; Faulds *et al.*, 2002a). The pluton and a major part of the volcanic section are 16-17 Ma and range in composition from early high silica trachyandesite and trachydacite (quartz monzonite) to late high-silica rhyolite (leucogranite).

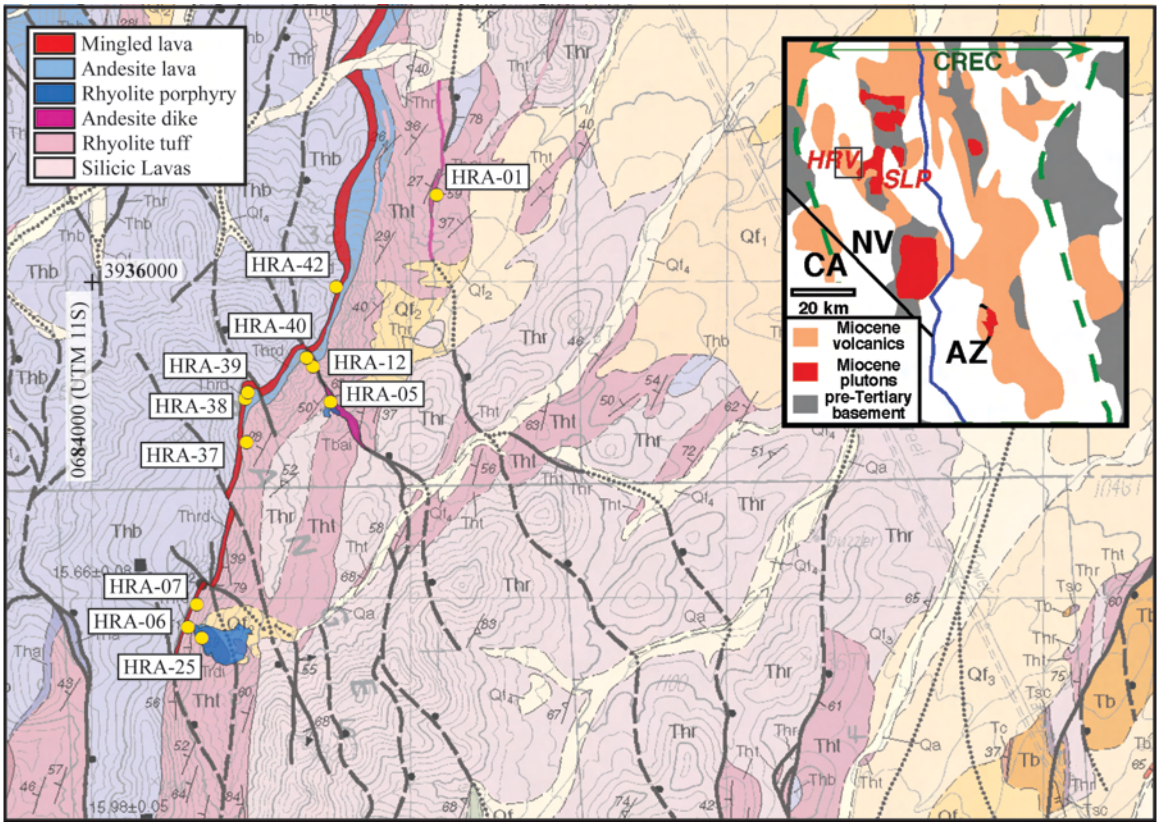

Figure 14 – Geologic map of the southern Highland Range Silicic Volcanic Sequence (HRSVS). Inset: regional map of the southwestern U.S. and the Colorado River extensional corridor (CREC); California (CA), Nevada (NV), Arizona (AZ), the Highland Range (HRV), and Searchlight Pluton (SLP) are indicated (modified after Faulds *et al.*, 2002a,b).

The southern Highland Range Silicic Volcanic Sequence (HRSVS)

This study is confined to four units (a mingled rhyolite lava, a rhyolite porphyry intrusion, an andesite dike, and an overlying andesite lava) exposed within the youngest (uppermost ~0.6 km) and most felsic portion of the ~2 km-thick southern Highland Range silicic volcanic sequence (HRSVS; Fig 14) in the northern CREC. Our aim is to investigate the petrogenetic connection between these units in an effort to better understand their significance within the Highland Range-Searchlight Pluton system as the final expression of silicic magmatism.

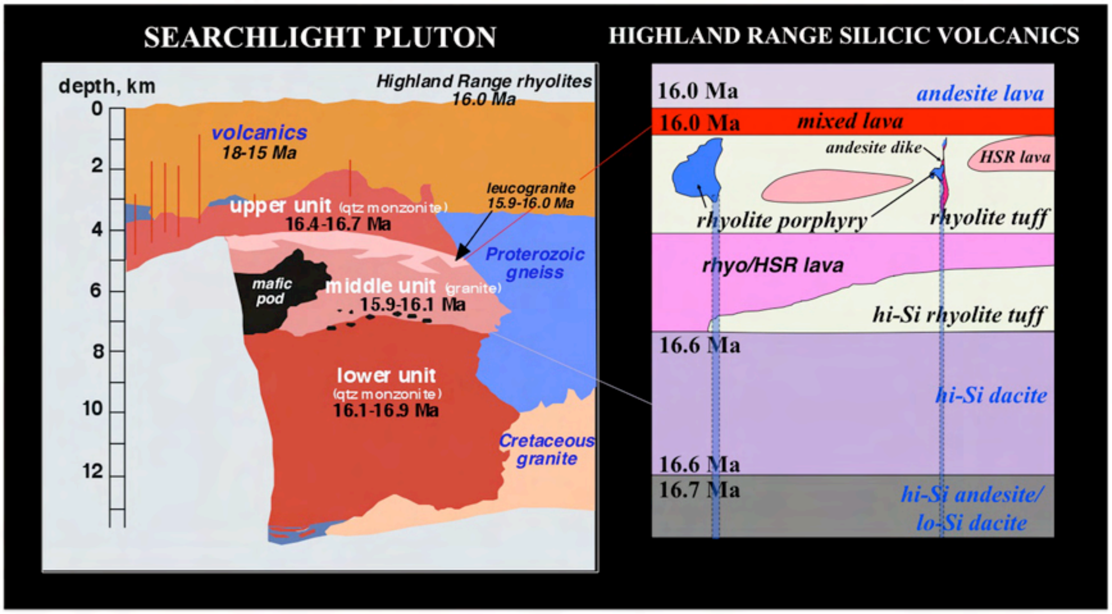

Figure 15 – Stratigraphic correlation between the Highland Range silicic volcanic sequence and the middle unit of nearby Searchlight Pluton (modified after Colombini, 2009).

Like the underlying Searchlight Pluton to the east, the HRSVS is tilted moderately to very steeply westward. Building upon the mapping and field descriptions of Faulds *et al.* (2002b), Colombini (2009) divided the HRSVS into six extrusive units plus small intrusions (Fig. 15). The lower section lava is a thick coulee of mostly high-SiO_2 rhyolite, but low-SiO_2 dacite, similar to lava underlying the silicic section, mingled extensively with and apparently contaminated the rhyolite (Kelly *et al*., 2010). Sparse, discrete enclaves of andesite are also present in this coulee. The uppermost section is roughly equally divided between mostly high-SiO_2 rhyolitic tuff and silicic lavas. Some lavas that inter-finger with the tuff are “clean” high-SiO_2 rhyolites, lacking any less silicic mingled material. The section is capped by a 16.0-16.1 Ma rhyolite lava (U-Pb, Ar-Ar; Colombini, 2009) that is mingled with andesite. This contaminated rhyolite is characterized by coarse, resorbed and rimmed phenocrysts of feldspar and quartz as well as xenocrysts of altered olivine. A small plug of rhyolite porphyry that intrudes the uppermost part of the tuff is almost identical to the capping mingled lava above it, except that it contains fewer andesite enclaves and reaction textures are less extreme. The age of the porphyry plug is essentially identical to that of the capping lava at 16.0-16.1 Ma (U-Pb, Ar-Ar; Colombini, 2009). A dike of andesite that engulfs a smaller pod of similar rhyolite porphyry also intrudes the upper part of the tuff. This section of rhyolites is younger than 16.6 Ma (age of the underlying trachydacite lava; Colombini, 2009), and older than an overlying andesite lava (16.0 Ma, Faulds *et al.*, 2002**b**). The major phenocryst phases in the rhyolite lavas and tuffs and the rhyolite porphyry intrusions are plagioclase, sanidine, quartz, clinopyroxene, and biotite. Sphene is evident in most thin sections and all samples from which mineral separates were obtained. Zircon, apatite, and opaque oxides (magnetite and ilmenite) are also present (Colombini, 2009).

The rocks of the uppermost HRSVS form a generally continuous and coherent geochemical array extending from 67 to 77 wt% SiO_2, excluding mafic enclaves and samples heavily contaminated by microenclaves (Fig. 20). They are all relatively potassic (K_2O 4.2-5.7 wt%, excluding enclave-rich material) and metaluminous to weakly peraluminous, as is typical of CREC rocks. Rare earth element patterns display light-REE enrichment and negative Eu anomalies of variable magnitude. The most notable trends in REE are generally diminishing concentrations and, especially, relative depletion in middle-REE in more silicic samples (Fig. 22). Colombini and Padilla *et al.* (2010) have shown that the elemental chemistry of the rhyolites is strikingly similar to the most fractionated rocks in the SLP and to rhyolite dikes that intrude the roof of the pluton, all of which are of similar age (Colombini *et al.*, 2008; Colombini, 2009).

CHAPTER II

METHODS

Fieldwork

Our research team (hereafter “we”) spent a total of 6 days in the field, making careful observations on the contact relationships between the units of interest in the HRSVS (porphyry intrusions, capping lava flows, andesitic dike, and host tuff), the extent of interaction between units, and the abundance and distribution of mafic magmatic enclaves within units, as well as any indicators on the nature and style of emplacement for both the intrusions and lava flows. Our study built upon previous field observations provided by Faulds *et al.* (2002a) and Colombini (2009). We collected a total of 23 samples from well-exposed outcrops in the sequence, including 5 from mingled lava and 10 from the rhyolite porphyries (see Fig. 14 and Table X for locations and sample descriptions). Samples were selected based on diversity of rock texture, abundance of mafic enclaves (for felsic samples), and/or phenocryst content, and aim at characterizing the internal variation of the rhyolite porphyry intrusions and the mingled capping lava, as well as the diversity of related mafic units exposed within the HRSVS.

Thin Section Petrography

Thin-sections were prepared by Idaho Petrographics (Grangeville, ID). I used a Zeiss Axioskop 40 petrographic microscope, equipped with an AxioCam MRc 5 camera, at Vanderbilt

Table 3

HIGHLAND RANGE SILICIC VOLCANIC SEQUENCE

Thin Section Petrography

Sample	Lithology	Location (UTM 11S)		Petrographic Summary			
		Easting	Northing	Major Mineral Phases[a] (approx. modal abundances)	Accessory Phases	Textural Features	Mafic Content
HRA-05a	Rhyolite porphyry	684753	3935617	Qtz (~10%), sanid (~55%), plag (~20%), biot (5-10%), CPX (<5%), oxides (<5%)	sphene (sub- to euhedral), zircon	--	MMEs, micro-enclaves
HRA-05c	Andesite dike	684753	3935617	Plag (~30-40%), iddings (<5%), CPX (~60%), oxides (<5%)	--	glassy matrix, plag microlites	n/a
HRA-05d	Hybrid	684753	3935617	Qtz (<5%), iddings (5-10%), sanid (10-15%), plag (~35%), CPX (~40%)	sphene (euhedral)	glassy matrix, plag microlites	absent
HRA-05f	MME	684753	3935617	Qtz (~10%), sanid (~15%), plag (~30%), CPX (~20%), iddings (~10%), biot (<5%), oliv (<5%), oxides (~5%)	sphene (reaction rims), zircon	glassy matrix	n/a
HRA-05g	Rhyolite porphyry	684753	3935617	Qtz (10-15%), sanid (~50%), plag (10-15%), biot (5-10%), CPX (<5%), oxides (~5%)	sphene (sbu- to euhedral), zircon	--	MMEs (diffuse)
HRA-06a	Mingled lava	684304	3934907	Qtz (10-15%), plag (~45%), sanid (5-10%), CPX (~20%), biot (~5%), iddings (<5%), oxides (~5%)	sphene (sub- to euhedral), zircon	glassy matrix, plag microlites	MMEs
HRA-06b	MME	684304	3934907	Plag (~55%), CPX (~25%), iddings (15-20%)	--	glassy matrix	n/a

[a] See notes on page 50.

Table 3 (continued)

HIGHLAND RANGE SILICIC VOLCANIC SEQUENCE

Thin Section Petrography

Sample	Lithology	Location (UTM 11S)		Petrographic Summary			
		Easting	Northing	Major Mineral Phases[a] (approx. modal abundances)	Accessory Phases	Textural Features	Mafic Content
HRA-12	Rhyolite porphyry	684697	3935728	Qtz (~20%), sanid (~40%), plag (~15%), biot (<10%), CPX (~10%), oxides (~5%), iddings (<5%)	sphene (subhedral), zircon	--	micro-enclaves, microlite-rich
HRA-25c	MME	684347	3934874	Plag (60-65%), CPX (~25%), iddings (<10%), sanid (<5%), oxides (1-2%)	--	plag microlite matrix	n/a
HRA-25d	Rhyolite porphyry	684347	3934874	Qtz (10-15%), plag (30%), sanid (~35%), biot (5-10%), CPX (<10%), iddings (~5%), oxides (<5%)	sphene (sub- to euhedral)	--	MMEs
HRA-37	Andesite lava	684488	3935490	Plag (35%), CPX (~40%), iddings (15-20%), sanid (<5%), oxides (5-10%)	--	plag microlite matrix	n/a
HRA-38	Mingled lava	684485	3935626	Plag (~35%), CPX (20-25%), iddings (~15%), sanid (~10%), biot (<5%), qtz (~5%), oxides (~5%)	sphene (sub- to euhedral)	devitrified glass	MMEs
HRA-40	Andesite lava	684678	3935756	Plag (30-35%), CPX (30-35%), sanid (~10%), iddings (~15%), biot (~5%), qtz (<5%), oxides (~5%)	sphene (thick reaction rims)	glassy matrix	n/a
HRA-42	Andesite lava	684771	3935978	Plag (~40%), CPX (~40%), iddings (~10%), oxides (~10%)	--	plag microlite matrix	n/a

Notes: [a] Mineral phases: quartz (qtz), sanidine (sanid), plagioclase (plag), clinopyroxene (CPX), Fe-Ti oxides (oxides), biotite (bio), and iddingsite (iddings).

University's Earth & Environmental Sciences Department to examine each thin-section and characterize its mineral assemblage and textural relations.

Whole-Rock Geochemistry

I selected fifteen samples of the rhyolitic porphyries, mingled lava, mafic magmatic enclaves, and intermediate lavas from the Highland Range and powdered them using shatterboxes (alumina for trace element analysis, zirconia for major element analysis) at Middle Tennessee State University. Samples powdered in the zirconia shatterbox were fused into glass discs to analyze for their whole-rock major element composition. Samples powdered in the alumina shatterbox were pressed into pellets to analyze for their whole-rock trace element abundances. All samples were analyzed using an Oxford Instruments MDX^{1080+} multi-dispersive X-ray fluorescence (MD-XRF) spectrometer. Standards *RGM-1*, *QLO-1*, *AGV-1*, *GSP-2*, *G-2*, and *BCR-2* were used for calibration.

Twenty to thirty grams of powder from nine of the Highland Range samples, powdered in the alumina shatterbox to avoid contamination in key trace elements, were mailed to the Michigan State University Geological Analytical Services Laboratory (East Lansing, MI) for further analyses of major and trace element abundances (including the rare earth elements) by a combination of x-ray fluorescence, using a Bruker S4 Pioneer wavelength dispersive X-ray fluorescence (WD-XRF) spectrometer, and laser ablation, using a Micromass Platform Inductively-Coupled Plasma-Mass spectrometer (ICP-MS). Standards *RGM-1*, *W-2*, *JA-2*, and *BHVO-1* were used for calibration.

Quartz Analyses

Separation and Imaging

I identified quartz phenocrysts from three different rock samples using a Zeiss Stemi 2000-C stereomicroscope. I then obtained in-situ crystals (to preserve rim textural context) by clipping ~5 mm^3 chips of rock containing the desired quartz crystals using a set of electrical pliers.

The clipped rock chips were mounted in epoxy and polished down to expose crystal interiors. I then imaged them by reflected light (RL), using a Leitz petrographic microscope equipped with a Paxcam digital camera, and cathodoluminescence (CL), using a JEOL 5600LV Scanning Electron Microscope (SEM) with custom Photo Multiplier Tube assembly, at the Stanford/USGS Micro Analysis Center (SUMAC). Quartz CL images primarily served as a guide in selecting spot placement in individual crystals for microprobe analyses using any presence of zoning as main criteria for spot selection.

SHRIMP-RG Analyses

We determined titanium (Ti) abundances of individual mounted quartz crystals using the SUMAC Reverse Geometry Sensitive High Resolution Ion Microprobe (SHRIMP-RG). Standard BT (Bishop Tuff, avg. 39.0 ppm Ti) was analyzed for calibration on a separate mount. The operating microprobe beam size was 15-20 µm. We used quartz CL images as a guide in determining spot placement on each grain, and since all grains were large enough multiple spots were placed on grains to discern any changes in Ti concentration between grain cores/interiors and rims/edges. We carried out a total of 61 Ti analyses on 20 grains. Data tables containing all quartz SHRIMP Ti analyses can be found in Appendix B.7.

Ti-in-Quartz Thermometry

Wark & Watson (2006) use the temperature dependence of the substitution of titanium (Ti) for silica (Si) in quartz to establish a quantitative relationship between Ti concentrations in quartz and its temperature of crystallization in the form of the TitaniQ thermometer, which can be stated as

$$T(°C) = \left(\frac{-(3765)}{\log[(Ti-in-quartz)/(a_{TiO_2})] - [5.69]}\right) - 273 \ ,$$

in which *Ti-in-quartz* is in parts per million (ppm). We use the above equation to estimate the crystallization temperature for all analyzed HRSVS quartz (see above section, *Quartz SHRIMP-RG Ti Analyses*, on methodology for obtaining Ti concentration in quartz). Using this method, the obtained temperature estimates are dependent on a well-constrained activity of TiO_2 (a_{TiO2}) in the melt at the time of quartz crystallization.

Choosing accurate values for a_{TiO2} is challenging since a_{TiO2} may vary throughout the crystallization history of quartz. However, the presence of Ti-essential phases, such as sphene, in the Highland Range suggests a_{TiO2} >0.5, and since no Highland Range rocks contain rutile it can be assumed that a_{TiO2} is <1.0, yielding a range of values consistent with those in a typical silicic magma at geologically relevant temperatures (0.6-0.9; Wiebe *et al.*, 2007; Watson *et al.*, 2006; Ferry and Watson, 2007; Hayden and Watson, 2007, Wark *et al.*, 2007). Thus, we find it appropriate to set a_{TiO2} to a uniform value of 0.7 in all our calculations of quartz crystallization temperatures.

We use the TitaniQ thermometer with caution, choosing a uniform value of a_{TiO2} for all our calculations to ensure that any quantitative error in our data processing is systematic, allowing us to qualitatively and reliably interpret the internal thermal variation and range of quartz crystallization temperatures within the Highland Range Silicic Volcanic Sequence.

CHAPTER III

RESULTS

Field Observations

Four different units exposed within the Highland Range silicic volcanic sequence (HRSVS) are of particular importance to this project (Figs. 14, 16, 17), and following the work and nomenclature provided by Faulds *et al.* (2002a) and Colombini (2009) we have re-defined, based on additional field observations and whole-rock geochemistry results, and grouped them as follows:

1) Intrusions:
   - Rhyolite porphyries (~71-74 wt. % SiO_2): A large isolated plug and two smaller individual pods, which I collectively term the "rhyolite porphyries," are exposed in the uppermost section of the HRSVS. All pods intrude into tuff and are surrounded by quenched vitrophyric margins against the tuff. "Mafic" magmatic enclaves (MMEs – in this case trachyandesitic), commonly with chilled and crenulate margins, are abundant in all the porphyries and they range in appearance from very mafic to hybrid and sometimes skialithic ("double enclaves" or "enclave within an enclave," usually a chilled dark mafic enclave surrounded by a lighter hybrid diffuse, though sometimes also chilled, outer zone, all surrounded by the host silicic rock; Mattson *et al.*, 1986), and are distributed unevenly throughout the porphyries. Large felsic phenocrysts (quartz and feldspar, up to 1 cm in length) are abundant in all porphyries. The largest of the three porphyries sits approximately 20m below the contact between tuff and the overlying mingled capping lava. The second largest pod

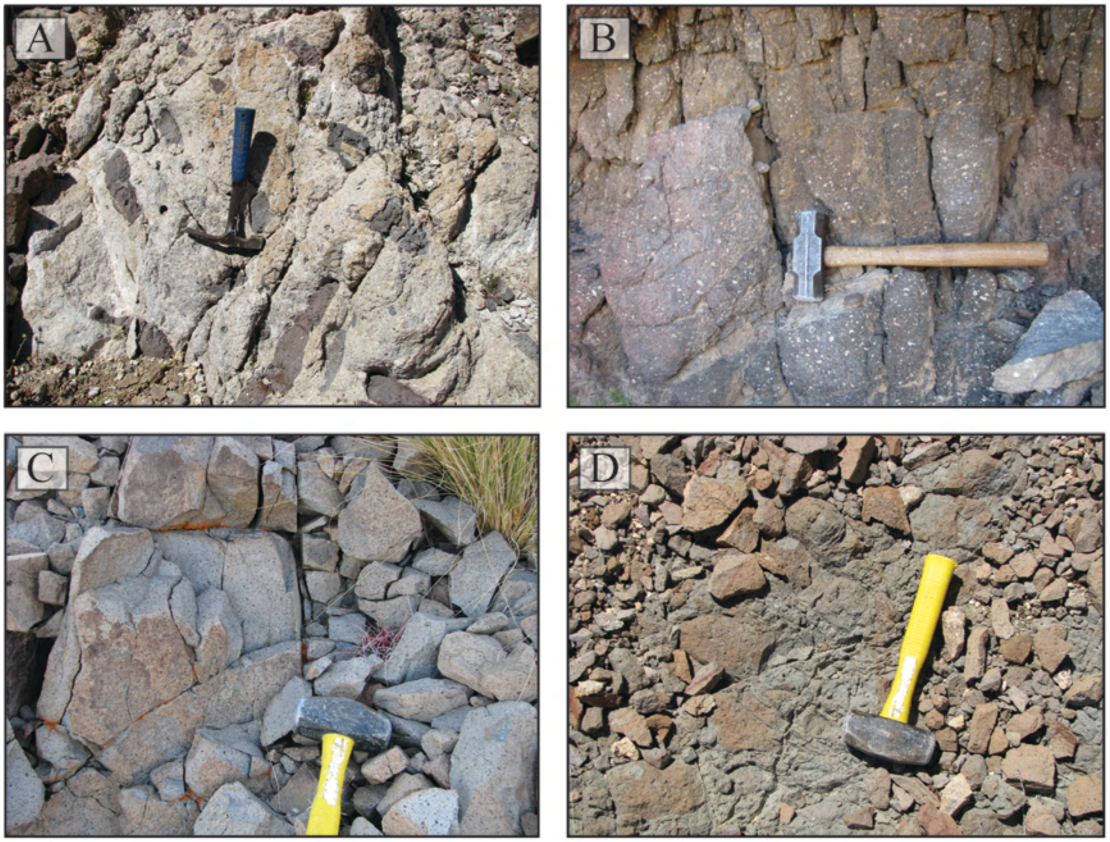

Figure 16 – Units of the uppermost Highland Range silicic volcanic sequence: A) rhyolite porphyry intrusion (locations HRA-05, -12, and -25 in Fig. 14); B) capping mingled lava (HRA-06, -07, -37, -38, and -39); C) andesite lava (HRA-40 and -42); and D) andesite dike (HRA-01 and -05).

preserves evidence of magma interactions between the rhyolite and a mafic dike that intersected the pod. The contact between the two units is mostly diffuse and gradational over 10s of cm, but in some areas the dike and porphyry are separated by a 1-2 m-wide zone of hybridization.

- Dikes (~58 wt. % SiO_2): Two prominent fine-grained, mafic dikes that intruded into the tuff are exposed within the upper HRSVS, one of which preserves magmatic interaction with a rhyolite porphyry pod (see *Intrusions* part 1 on rhyolite porphyries above). The margins of the dikes are quenched and glassy where they are in contact with tuff, and the tuff displays a 10-20 cm baked zone along the margins of the dikes.

2) Capping Mingled Lava

- A 20-25 m-thick trachydacitic (in bulk composition) lava (~60-65 wt. % SiO_2) caps the HRSVS. MMEs with crenulate, chilled, quenched, and diffuse margins, including skialiths, are common, and large felsic phenocrysts are very abundant. The lava resembles the rhyolite porphyries very closely in texture, phenocryst- and MME-content, and its appearance suggests it is the result of extensive mingling and mixing between a mafic magma and a rhyolite porphyry-like component. The base of the lava is vitrophyric (quenched) in some places, and it was partly emplaced above a ~1-2 m-thick tuffaceous paleosol. Sedimentary-like structures, such as flame-like apophyses and load casts, are preserved along this contact, and it resembles lava-wet sediment interactions similar to those described by Duffield *et al.* (1986). The lower part of the lava is a basal breccia (*cf* McPhie *et al.*, 1993), and in some places the lava is brecciated from top to bottom. The upper part of the lava is partly mingled with overlying andesite lava, and in some locations both lavas are brecciated together within a common fine-grained paleosol matrix (Fig. XX -- field picture of mingling capping lava + andesite lava). Similarly, in the northernmost exposed section, where the mingled lava is locally underlain by andesite lava, the basal breccia preserves partial mingling between the two lava flows.

3) Andesite Lava

- Thick andesitic lavas (~58-61 wt. % SiO_2) overlying the capping mingled lava overlie the Highland Range Silicic Volcanic Sequence (cf. Feuerbach, 1998; Faulds *et al.*, 2002a,b). They are homogeneous, and contain small phenocrysts of pyroxene. In the northernmost section, where andesite lava locally underlies the capping mingled lava, it is in direct contact with the tuffaceous paleosol making up the uppermost section of the tuff.

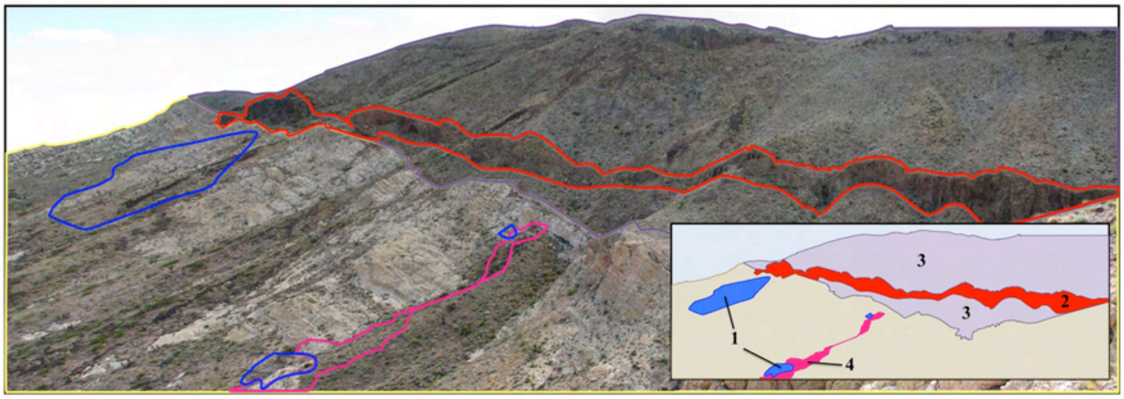

Figure 17 – Field view of the uppermost section of the Highland Range silicic volcanic sequence (HRSVS), with the units of importance to this study outlined as indicated. Inset: Schematic representation of the field relationships and stratigraphy of the uppermost HRSVS; outlined units are 1) rhyolite porphyries, 2) capping mingled lava, 3) andesite lavas, and 4) andesite dike.

Petrography

Rhyolite Porphyries and Capping Mingled Lava

A key characteristic of the rhyolite porphyries and the capping mingled lava is their high phenocryst content, mainly composed of quartz, plagioclase (up to 1cm in length), and sanidine in a very fine-grained matrix. Resorption of quartz and reaction rims on plagioclase and sanidine crystals are common in both units, though reaction rims are generally thicker and more pronounced in the capping mingled lava (Fig. 18). Plagioclase in the capping mingled lava displays more extensive embayment and dissolution (Fig. 18). In thin section, the vitrophyric porphyries and vitrophyric mingled capping lava are virtually indistinguishable from each other.

While quartz, plagioclase, and sanidine make up the main phenocryst assemblage in the rhyolite porphyries, clinopyroxene (CPX), biotite, and iddingsite (pseudomorphs after olivine,

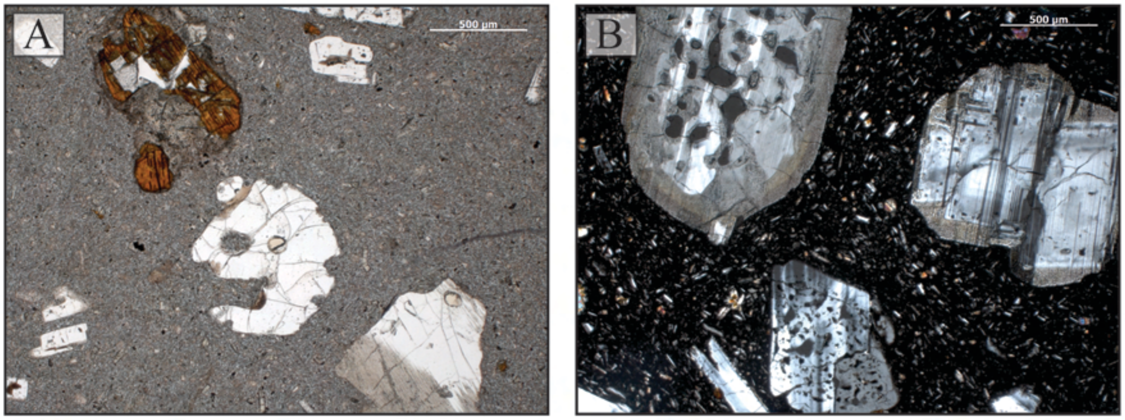

Figure 18 – A) Plane-light photomicrograph (magnified at 5x) of the rhyolitic porphyry, showing highly resorbed, rounded, and embayed quartz phenocrysts (center) and inherited iddingsite phenocrysts (top left) in a fine-grained glassy matrix. B) Crossed-polarized light photomicrograph (magnified at 5x) of the mingled lava, showing highly resorbed and embayed plagioclase and sanidine crystals with thick alteration rims in a fine-grained glassy matrix.

resulting from oxidative alteration; *cf* Delvigne *et al.*, 1979; Smith *et al.*, 1987) are also present in smaller abundance (usually <10% of total phenocrysts). In comparison, biotite, CPX, and pseudomorphs after olivine are much more abundant in the capping mingled lava. These phenocrysts are typically altered, although fresh olivine cores are occasionally preserved within iddingsite. Mafic micro-enclaves, commonly associated with large, altered CPX and plagioclase phenocrysts, are abundant in both units. When present, biotite crystals are commonly rimmed by opaque minerals. Zircon and euhedral sphene are common accessory phases in the porphyries and capping mingled lava alike, and sphene in the capping mingled lava usually displays very thick alteration jackets.

Andesite Lava, Mafic Dikes, and MMEs

The andesite lava, mafic dikes, and MMEs share a very similar main phenocryst assemblage, usually consisting of abundant small-to-medium CPX, plagioclase, and iddingsite. In rare instances, fresh olivine cores are preserved in the cores of iddingsite. MMEs in the rhyolite porphyries and capping mingled lava usually contain minor abundances of quartz and sanidine in addition to CPX, plagioclase and iddingsite. The groundmass in all three units is dominantly composed of plagioclase microlites, and is usually indistinguishable between units in thin section (Fig. 19). Phenocrysts in all units typically display some degree of alteration, and fresh, unaltered crystals are extremely rare to non-existent. A summary of the HRSVS petrography can be found in Table 3, and additional photomicrographs of the units described above are included in appendix C.

Whole-Rock Geochemistry

We obtained whole-rock major oxide and trace element abundances from 15 samples representative of the upper HRSVS units described above in order to characterize the geochemical diversity within each unit. Of these, 4 encompass the internal variation of the rhyolite porphyries, 6 characterize the range in compositions of the mafic dike as well as MMEs within the porphyries, 2 represent the capping mingled lava, and 3 represent the andesite lava that caps the HRSVS. Full whole-rock geochemical data for our samples are presented in appendix B.

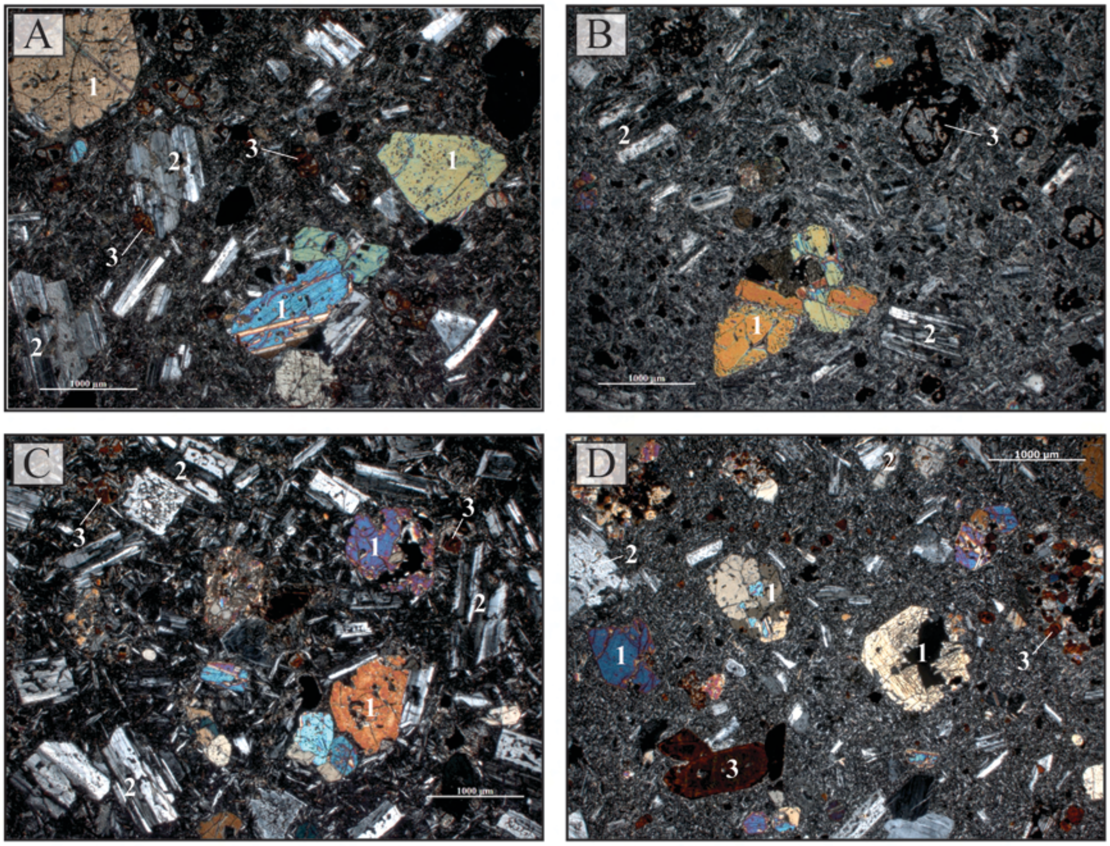

Figure 19 – Crossed-polarized light photomicrographs (magnified at 2.5x) of the intermediate units of the uppermost Highland Range silicic volcanic sequence: A) andesitic dike (sample HRA-01); B) mafic magmatic enclave (MME) in the rhyolite porphyry intrusion (sample HRA-05f); C) MME in the rhyolite porphyry intrusion (sample HRA-25c); and D) andesite lava (sample HRA-40). All samples contain plagioclase microlite matrix, with abundant CPX (1), plagioclase (2), and iddingsite (3) phenocrysts..

Major Oxides

Our HR whole-rock data display typical major oxide trends in Harker plots, showing a general increase in K_2O and decrease in TiO_2, Al_2O_3, Fe_2O_3, MnO, MgO, CaO and P_2O_5 with increasing SiO_2 content (Fig. 20). The data display a coherent linear trend for most major oxides and fit well into a mixing line with other units of the Highland Range, including high-Si rhyolite and trachyandesite lavas (HRL), as well as units from the middle section of nearby Searchlight Pluton (middle SLP - which we believe is the source for the felsic units of the HRSVS),

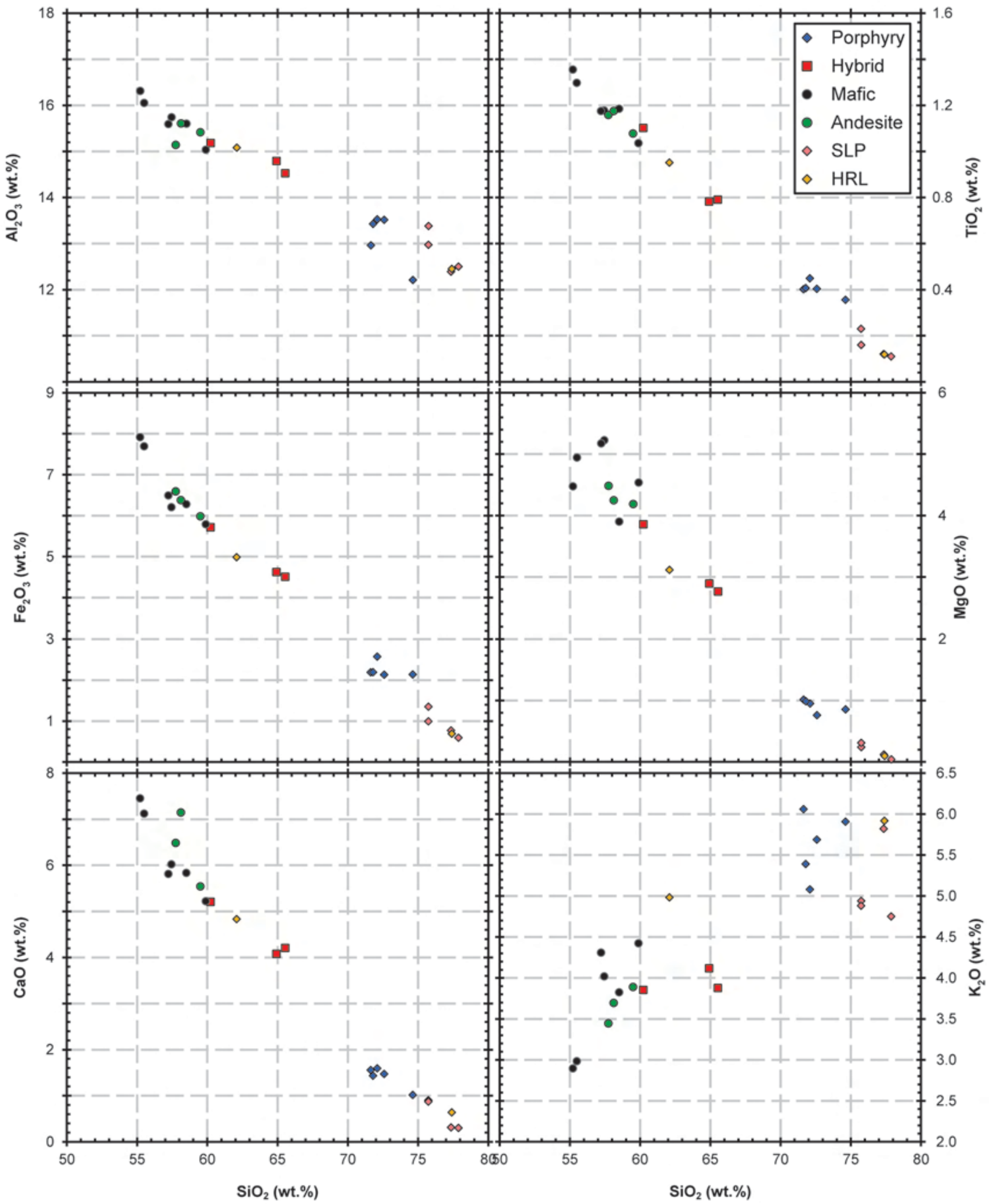

Figure 20 – Highland Range silicic volcanic sequence and related Searchlight Pluton whole-rock major oxide geochemistry.

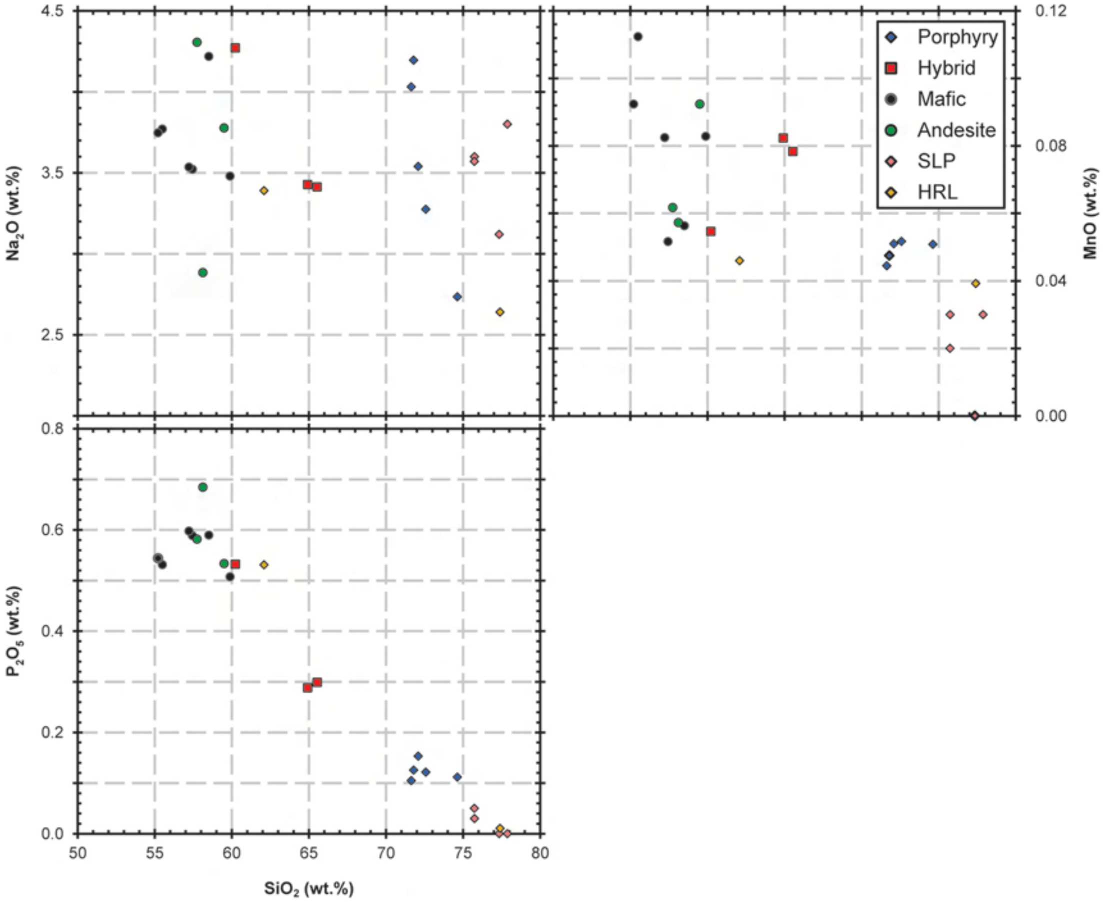

Figure 20 (continued) – Highland Range silicic volcanic sequence and related Searchlight Pluton whole-rock major oxide geochemistry.

including leucogranites and high-Si rhyolites. The evolved units of middle SLP are relatively higher in K_2O and contain lower TiO_2, Al_2O_3, Fe_2O_3, MnO, MgO, CaO and P_2O_5 abundances, consistent with the HR geochemical trends described above. We divide the samples into three distinct compositional groups, each of which is distinguishable in the above Harker diagrams (Fig. 21):

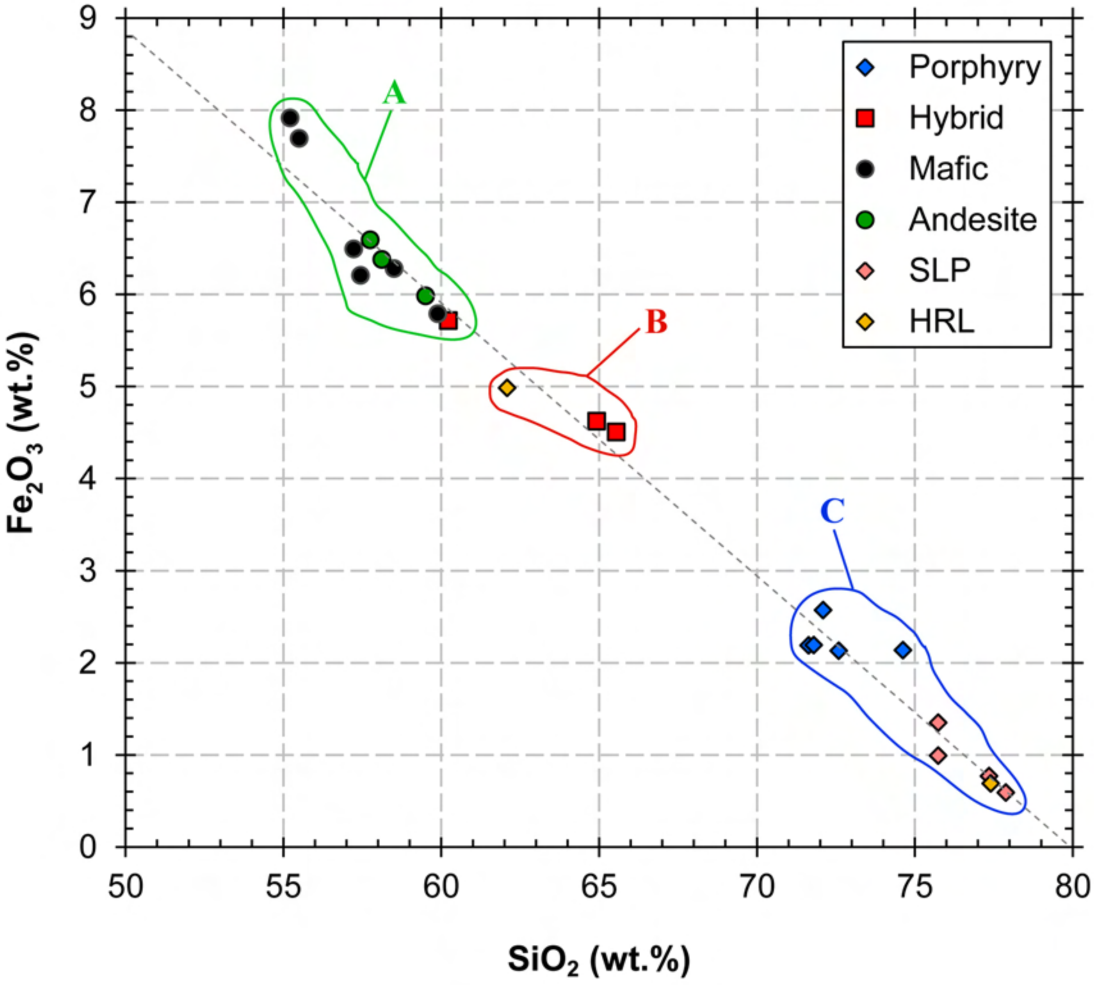

Figure 21 – Highland Range silicic volcanic sequence samples can be divided into three compositional groups based on their whole-rock major oxide abundances: A) mafic end-members, which includes andesite lavas, andesite dikes, and MMEs in the rhyolite porphyries and capping mingled lava; B) intermediate units, which includes the capping mingled lava; and C) felsic end-members, which includes the rhyolite porphyries, silicic lavas from the HRSVS, and silicic units from the middle section of Searchlight Pluton.

1) *Mafic end-members* (~55-60 wt. % SiO_2): includes the overlying andesite lava, mafic dikes, and MMEs in both the porphyries and the capping mingled lava
2) *Intermediate units* (~62-66 wt. % SiO_2): includes the capping mingled lava

3) *Felsic end-members* (~71-78 wt. % SiO_2): includes the rhyolite porphyries, a high-Si rhyolite lava from the HRSVS, and felsic units from the middle section of Searchlight Pluton (SLP)

All samples are relatively potassic (K_2O ~3.0-6.0 wt%) and metaluminous to weakly peraluminous, a typical characteristic of rocks from the Colorado River Extensional Corridor.

Rare Earth Elements (REE)

All HRSVS samples have chondrite-normalized rare earth element patterns that display light-REE enrichment relative to heavy-REE and negative Eu anomalies, as is typical for felsic igneous rocks. Most notably, middle-REE concentrations generally diminish and are relatively depleted with increasing SiO_2 content (Fig. 22). Similarly, the magnitude of the negative Eu anomaly increases with increasing SiO_2 content. Some of the rhyolite porphyries and capping mingled lava analyses display slightly higher heavy-REE enrichment than all other units, particularly in Yb and Lu. Similar heavy-REE enrichment is observed in more evolved rocks of the HR-SLP system, namely in HR high-Si rhyolite and middle SLP leucogranite. These more evolved units display stronger middle-REE depletion and generally contain lower REE abundances than any of our other samples.

Other Trace Elements

Whole-rock trace element abundances within the HRSVS generally display linear

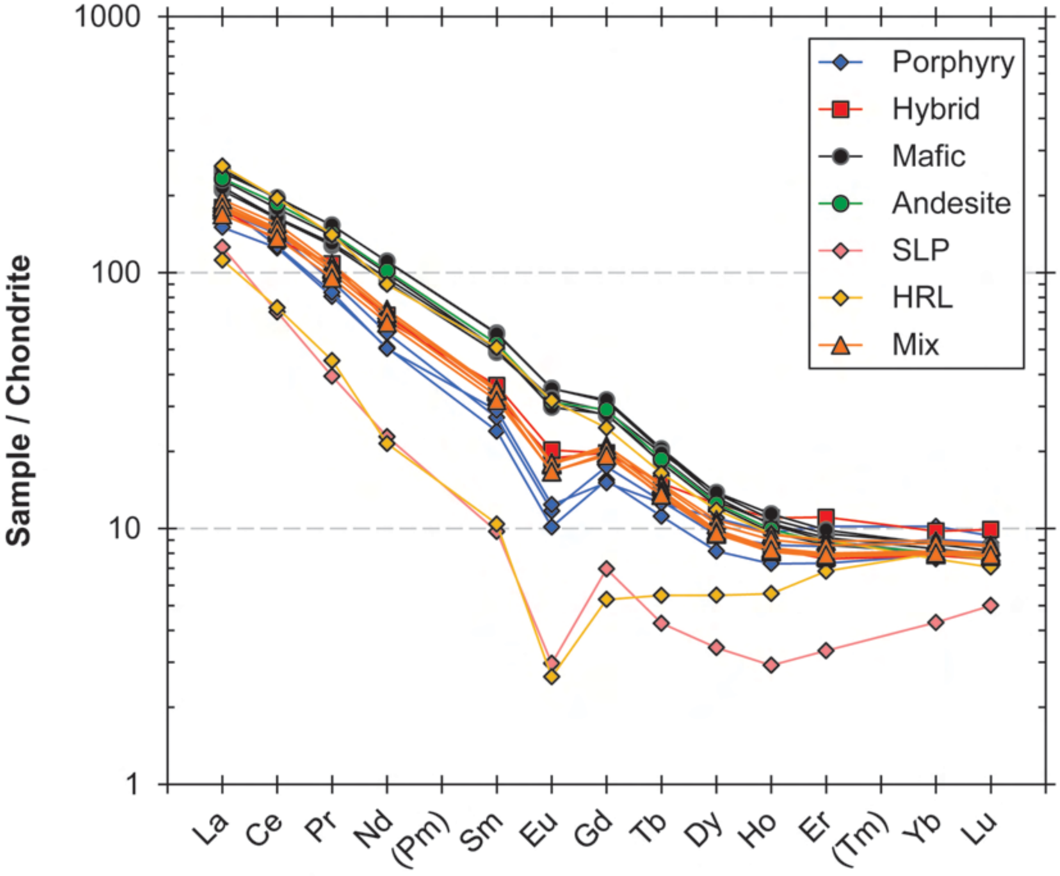

Figure 22 – Whole-rock rare earth element geochemistry for rocks of the Highland Range silicic volcanic sequence and related Searchlight Pluton units.

trends on element-element diagrams (Fig. 23). Sr and Ba decrease linearly with increasing SiO_2 concentrations, while Rb, Th and U generally increase (Fig. 23). Trace element abundances in middle-SLP units are consistent with these trends, with low Sr and Ba, and generally higher Rb, Th and U concentrations. Mafic end-members (see Major Oxides section above) can be split into two coherent groups (high- and low-concentration) based on their Cr and Ni abundances, both of which display a negative linear correlation with SiO_2. One of our capping mingled lava samples also falls within the low-Cr/low-Ni group (Fig. 24). Zr and Hf, which typically increase with increasing SiO_2 due to their incompatibility in mafic to intermediate magmas, display negative correlations with SiO_2 in our HRSVS samples.

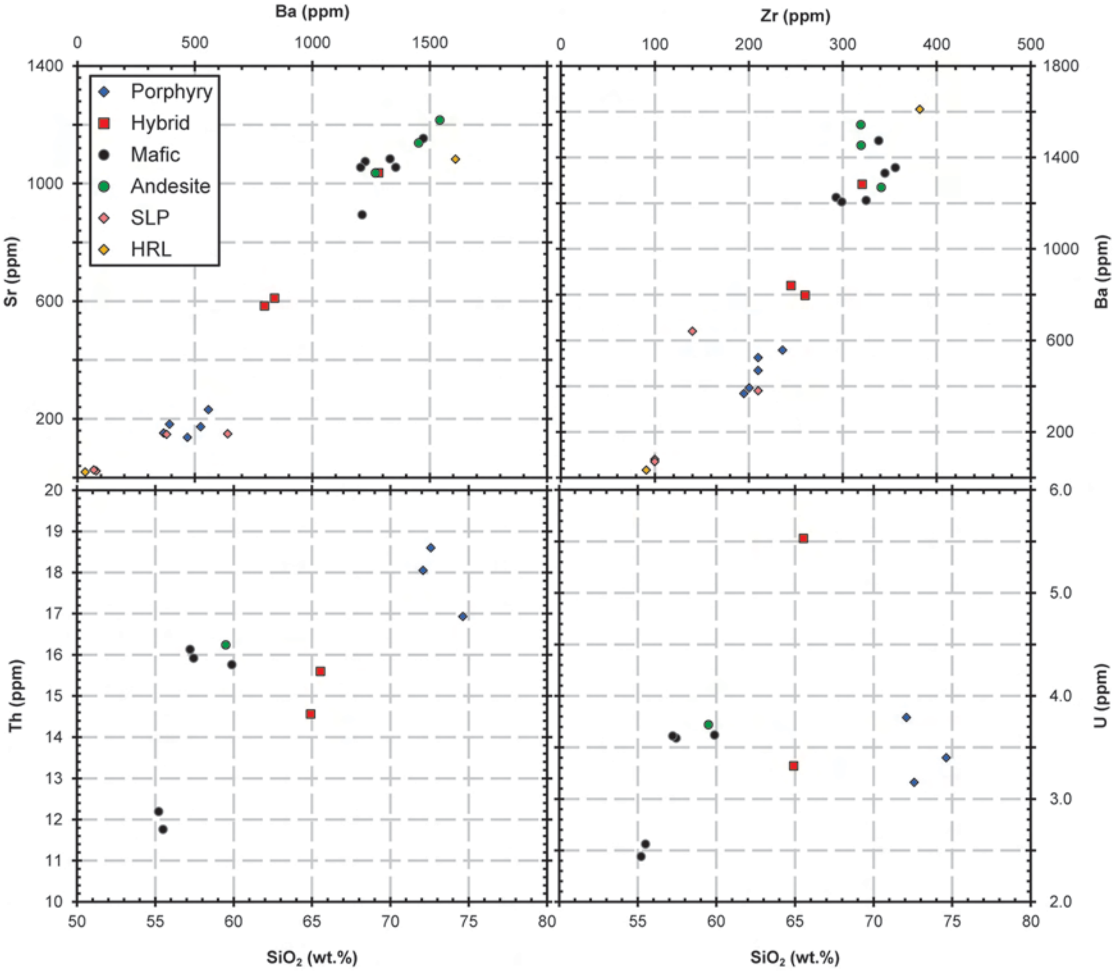

Figure 23 – Selected whole-rock trace element geochemistry for rocks of the Highland Range silicic volcanic sequence and related Searchlight Pluton units.

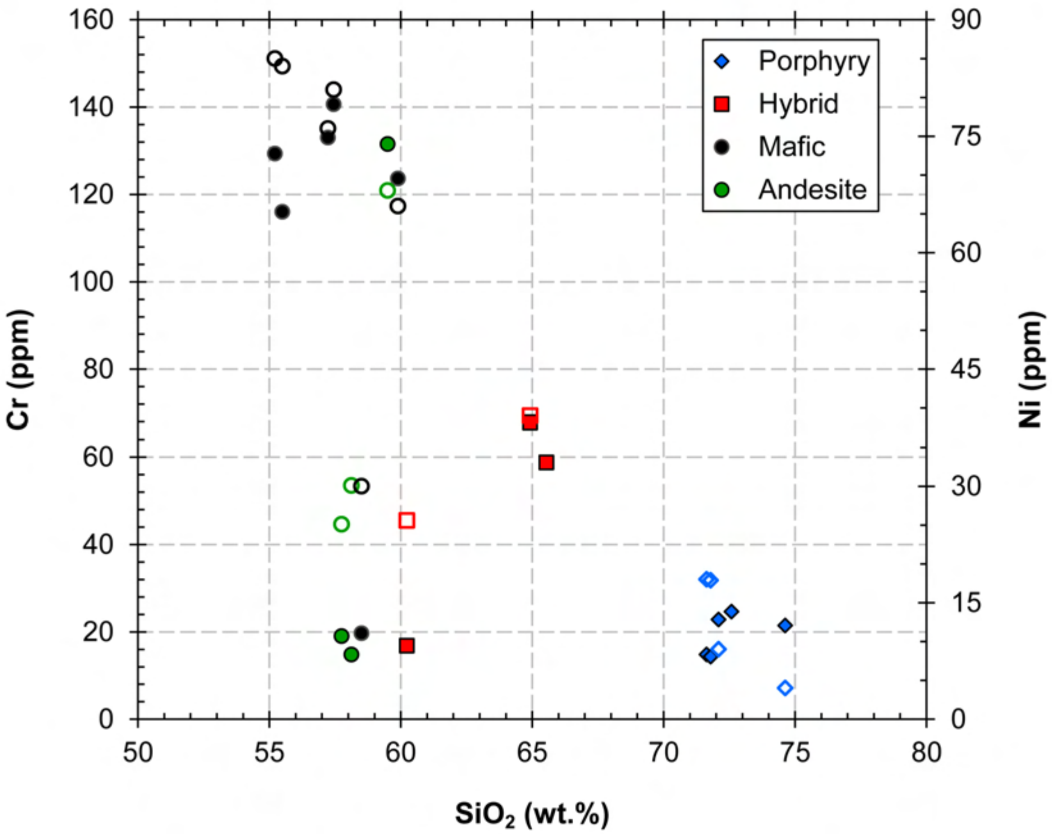

Figure 24 – Whole-rock SiO$_2$ vs. Cr (filled symbols) and Ni (open symbols) abundances in the main units of the upper Highland Range silicic volcanic sequence presented in this study.

TitaniQ Temperatures

We clipped individual in-situ quartz crystals from three samples for SHRIMP analyses. Two of our samples come from the rhyolite porphyry intrusions (HRA-25d and HRA-05a) while the third one is representative of the capping mingled lava (HRA-06a).

Our estimates of crystallization temperature, based on quartz Ti abundances, yield a range of ~725-800 °C (55-95 ppm Ti) for most quartz, with few analyses falling outside this range (Fig. 25). Grains from one porphyry (sample HRA-05a) fall into a narrower temperature

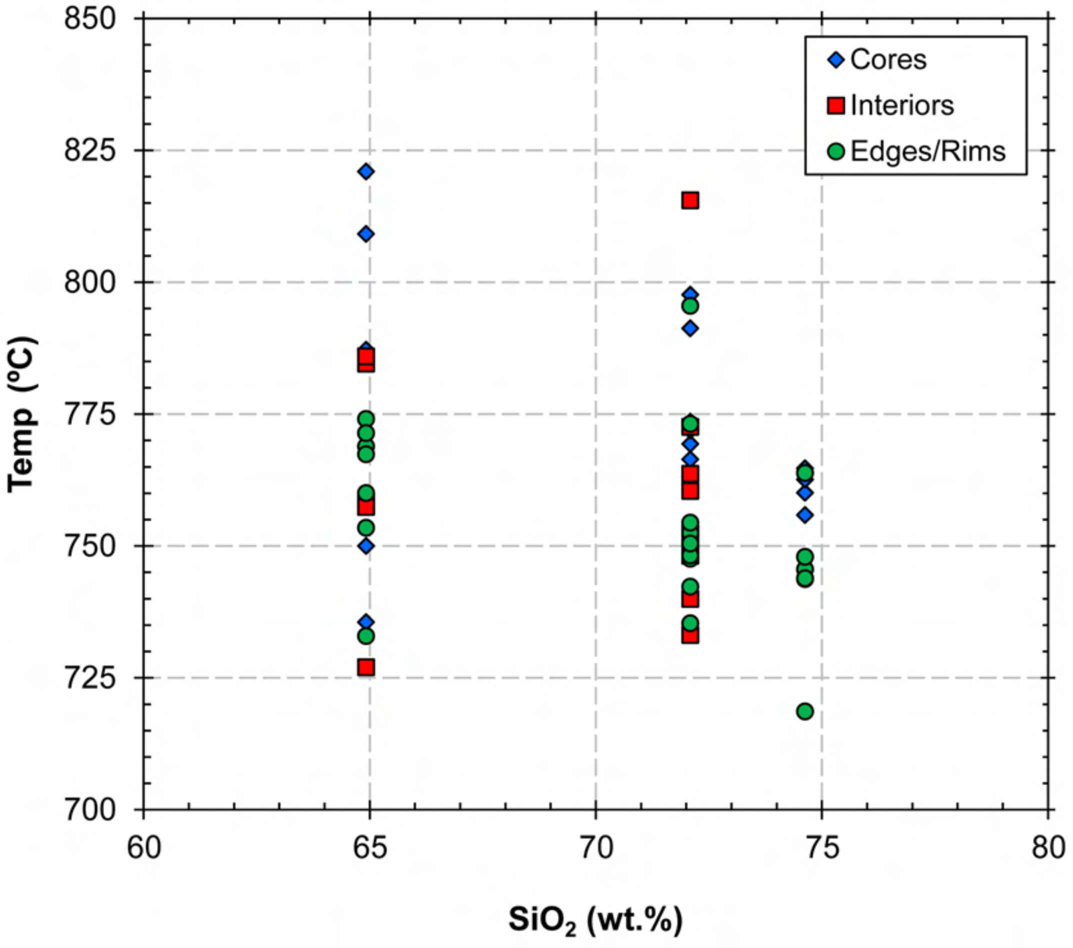

Figure 25 – Calculated quartz crystallization temperatures from in-situ SHRIMP-RG Ti analyses in individual crystals from samples HRA-05a (rhyolite porphyry, ~75 wt.% SiO_2), HRA-06a (capping mingled lava, 65 wt.% SiO_2), and HRA-25d (rhyolite porphyry, 73 wt.% SiO_2). Temperatures calculated using the TitaniQ thermometer of Wark & Watson (2006).

range of ~740-765 °C (63-75 ppm Ti), with only one analysis outside this range, while grains from the capping mingled lava (sample HRA-06a) display the largest temperature variation (~725-820 °C, or 55-115 ppm Ti). Some grains with multiple analyses show a slight core-to-rim increase in Ti. However, the general trend observed in most quartz grains is that of decreasing core-to-rim Ti concentrations. The full data suite for quartz Ti analyses can be found in appendix B.9.

CHAPTER IV

DISCUSSION

Field Relationships

The host tuff displays a zone of baking (contact alteration) along the margins of the mafic dikes and the rhyolite porphyries and the margins of the porphyries and dikes themselves are vitrophyric, both of which indicate a significant difference in temperature between the units upon the emplacement of the porphyry and intrusion of the dike.

Mafic magmatic enclaves within the porphyry commonly have chilled, crenulate, and quenched margins, indicating that the enclave magma source was hotter than its host when it was injected into the porphyry magma. Some enclaves have diffuse boundaries and higher SiO_2 content, and skialiths are present throughout. These features are typically indicative of extensive magma mingling between the mafic component and the host porphyry magma (*cf* Vernon, 1984; Mattson *et al*., 1986; Falkner *et al*., 1995; Harper *et al*., 2004). Furthermore, a 1-2 m wide gradational zone of hybridization is present along the boundary where the mafic dike intersected the rhyolite porphyry, providing further evidence for the occurrence and extent of magma mingling as well as mixing between the porphyries and intruded mafic magmas. The dike is seen disaggregated into hybrid enclaves along the edge of this zone, suggesting the dikes are the source of the MMEs that were injected into and dispersed throughout the porphyry magma.

The presence of the hybrid zone and the enclaves within the rhyolite porphyries gives us a clue about the rheology of the two magmas at their time of interaction: in order for mixing to take place (as it did in the hybrid zone), both components must have been relatively mobile and hot (i.e. magmas; *cf* Vernon, 1990; Frost and Mahood, 1987). This would have allowed a large enough volume of mafic (dike-like) magma rising through the crust to interact with a ponded rhyolitic magma (porphyry-like) and hybridize prior to reaching the surface and erupting as an intermediate product (i.e. the compositionally dacitic capping mingled lava).

Petrography

One of the most noteworthy characteristics of the rhyolite porphyry and the capping mingled lava is their high content of quartz, plagioclase and sanidine phenocrysts. The size (up to 1cm across for plagioclase) and abundance of the phenocrysts indicates that the parent magma for both of these units underwent substantial crystallization prior to the intrusion of the porphyry and extrusion of the mingled lava.

The extent of resorption, embayments, and reaction rims on the felsic phenocrysts, as well as other mineral phases such as sphene, are typically indicators of a heating event, and may have been due to replenishment by hotter, more mafic magma into the silicic system. Plagioclase phenocrysts in the mingled lava display more extensive embayment and dissolution, and reaction rims are generally thicker and more pronounced than in the porphyries. These features likely reflect a greater magnitude of heating for the mingled lava.

In addition to re-heating, the mineral assemblage in the capping mingled lava supports extensive mingling prior to emplacement. Phases that do not typically coexist in a melt, especially olivine with quartz, sphene, and sanidine, are found in great abundance within a shared matrix. The phenocryst assemblage of plagioclase, sanidine, quartz, biotite, clinopyroxene, sphene, and iddingsite (often with unaltered olivine cores) can be easily achieved by mixing the large felsic phenocrysts from the rhyolite porphyry (sanidine, quartz, sphene) with mafic phenocrysts from the dike or andesite lava (CPX, iddingsite).

Quartz and feldspar phenocrysts are also present in MMEs, and the fine-grained plagioclase microlite matrix in the MMEs is likely a result of quenching and rapid crystallization within a plutonic environment due to temperature contrasts between magmas during mixing or mingling, which resulted in a strongly undercooled enclave magma (Vernon, 1986). These textures and phenocryst assemblage, along with the abundance and distribution of MMEs within the porphyry, indicate that mixing and mingling of their mafic precursor with a rhyolitic magma occurred prior to the emplacement of the porphyry. Similarly, iddingsite phenocrysts that are present, though not common, in the porphyry were likely inherited through prior mixing.

Whole-Rock Geochemistry

Whole-rock geochemistry of the HRSVS displays well-defined linear trends for all major oxides and various trace elements (see Figs. 20, 21 and 23). The three distinct mafic, felsic, and intermediate geochemical groups (see *Major Oxides* in Results) fit well into a mixing line with other units of the Highland Range (high-Si rhyolite and trachyandesite lavas) and the middle section of Searchlight Pluton (leucogranites and hi-Si rhyolite dikes).

Two distinct mafic end-member groups can be identified on the basis of their Cr and Ni concentrations (Fig. 24): a high-Ni and high-Cr group, and a low-Ni and low-Cr group. One of our capping mingled lava samples overlaps with the low-Cr/Ni group on Ni/Cr vs. SiO_2 plots, suggesting it was derived from one of the mafic components within that group. We use Ni and Cr abundances as a proxy for the extent of evolution of magma, with higher abundances interpreted to represent a more primitive magma or magmatic source. Thus, the distinction between these two mafic groups may indicate replenishment by distinguishable relatively mafic magmas that took place throughout the history of the HRSVS and generated the enclaves within the porphyry and mingled lava, as well as the mingled lava itself.

The rare earth element (REE) patterns of the HR and middle SLP units also support multi-component mixing between felsic and mafic end-members. Simple theoretical mixing calculations using a range of combinations of the mafic HRSVS units and the rhyolite porphyries can yield accurate approximations of the intermediate (capping mingled lava) REE concentrations. Similarly, the major element abundances of the capping mingled lava can be approximated to within 10% by using the exact same mixing proportions as for REE (see Fig. 22).

Interpretations

We interpret the compositionally dacitic capping mingled lava to be a product of two-end-member mixing between a porphyry-like rhyolitic magma, and a hotter, and perhaps younger, andesitic magma. The proximity, similarity, and stratigraphic relationship between the rhyolite porphyry and the capping mingled lava support a genetic connection between the two units, which are also essentially identical in age at 16.0-16.1 Ma (Colombini, 2009).

The geochemical data support our proposed origin of the rhyolite porphyry, previously based on field observations and petrography, by mingling between a *more mafic end-member* (such as the trachyandesitic dike) and a high-SiO_2 *felsic end-member* (such as the SLP leucogranites and Highland Range high-silica rhyolites), and similarly the origin of the capping mingled lava by mixing of a *mafic end-member* (such as the andesite lava) with an already mingled *felsic end-member* (such as the rhyolite porphyries). We argue, based on age, geochemistry, and stratigraphic location, that the silicic magmas that generated the felsic units of the HRSVS were all derived from the middle section of SLP.

The capping mingled lava is the last silicic unit to appear in the Highland Range Silicic Volcanic Sequence (HRSVS), representing the final episode of silicic magmatism and volcanism within the HR-SLP system. The andesite lava that overlies the capping mingled lava and HRSVS is the first andesitic lava to appear in the Highland Range since the emplacement of the 16.5 Ma high-silica trachyandesite lava that defines the base of the HRSVS, and thus marks the final silicic gasp and solidification of the Searchlight Pluton, and the transition to mafic volcanism at the Highland Range.

CHAPTER V

CONCLUSIONS

Our whole-rock geochemistry data, field observations, and textural evidence support the generation of the felsic units exposed in the Highland Range Silicic Volcanic Sequence (HRSVS) by multi-component mixing of felsic and andesitic magmas derived from the Searchlight Pluton (SLP), including the origin of the rhyolite porphyries by mingling of evolved leucogranites from the middle section of SLP with mafic magma recharge within a crystal-mush setting, and of the capping dacitic lava by chemical and mechanical mixing of a rhyolite porphyry-like magma with intruding andesitic magmas on their way to eruption. The petrography of our samples indicates that extensive re-heating of magmas took place, contributing to the mobilization of crystal-rich magmas within the SLP-HR system.

We argue that the size and abundance of quartz, plagioclase, and sanidine phenocrysts in the porphyries, portions of the andesite dike, and the capping mingled lava were products of prolonged crystallization of highly evolved melt, likely as a leucogranite crystal-mush within the middle section of SLP during its waning stages. This crystal-mush was then re-heated by the intrusion of younger, hotter andesite magma. Andesite had not previously erupted as lava in the HRSVS, but had been entrained as small enclaves in earlier rhyolite (Kelly *et al*., 2010). The solidifying SLP, which had previously formed a low-density, low-strength cap, was probably dense and rigid enough to permit intrusion by andesite at the stage marked by the mingled porphyry and lava. This re-heating allowed the dense and rigid crystal mush to mobilize, and eventually be partially emplaced as the rhyolite porphyry intrusions and erupt at the surface as the capping mingled lava. This capping mingled lava is the last felsic unit exposed in the HRSVS sequence; all overlying (younger) units within the HRSVS are mafic in composition (basaltic to andesitic lavas). Thus, this rhyolite-to-andesite transition represents the final episode of SLP-HR magmatism, and the capping mingled lava contains the very last felsic magma to be mobilized and extracted from SLP: it is the death rattle of the SLP-HR silicic system.

CONCLUSIONS

Austurhorn Intrusive Complex and the youngest rocks of the Highland Range silicic volcanic sequence both reveal extensive interaction (mingling as well as partial mixing) between mafic and silicic magmas. Together, they thus provide a useful comparison of the manifestation and consequences of mafic recharge in silicic systems at depth and in erupted products.

Zircon from the AIC records a very complex and long-lived silicic magmatic system, characterized by multiple episodes of mafic magmatic replenishment. In particular, zircon U/Pb data reveal a major recharging event a half million years after growth of most of the zircon in the felsic rocks. Based on field relations and the presence of some younger zircon in the felsic rocks, we infer that this event reactivated the resident felsic material in the intrusion. Furthermore, comparing zircon compositions from the AIC, where silicic, continental-like magma formed in a dominantly mafic oceanic tectonic environment, with those of zircon from other systems and environments sheds light on the role that the processes evident here may have played in the evolution of Earth's crust over geologic time.

The Highland Range serves as an excellent example of the close connection and complex relationship between underlying plutons and eruptive centers on the Earth's surface. Perhaps most uniquely, the HRSVS records the very last stages of life, or the *death throes*, of a silicic plutonic system and its volcanic counterpart. We infer that this final burst of silicic volcanism was a consequence of mafic recharging and remobilization of crystal-rich mush. Thus, the two case studies – one of an intrusive complex, the other of a volcanic sequence – may be linked by the shared process of mafic recharge-induced remobilization of a moribund, silicic crystal mush.

REFERENCES

Anders, E., and Grevesse, N., 1989. Abundances of the elements: Meteoritic and solar. *Geochimica et Cosmochimica Acta* 53:197-214.

Bachl, C.A., Miller, C.F., Miller, J.S., and Faulds, J.E., 2001. Construction of a pluton: Evidence from an exposed cross section of the Searchlight pluton, Eldorado Mountains, Nevada. *Geological Society of America Bulletin* 113(**9**): 1213-1228.

Blake, D.H., 1966. Net-veined complex of Austurhorn Intrusion, Southeastern Iceland. *Geology* 74(**6**): 891-907.

Bromley, S.A. *et al*., 2007. Record of hybridization preserved in zircon, Aztec Wash Pluton, NV. *Eos Trans.* AGU 88(52), Abstract V51C-0705.

Carley, T.L., Miller, C.F., Wooden, J.L., and Barth, A.P., 2009. Using zircon to reconstruct the magmatic history of Iceland rhyolite. *Eos Trans.* AGU 90(52), Abstract V51A-1661.

Carley, T.L., Miller, C.F., Wooden, J.L., Bindeman, I.N., and Barth, A.P., 2011. Zircon from historic eruptions in Iceland: Reconstructing storage and evolution of silicic magmas. *Mineralogy and Petrology* (in press).

Cherniak, D.J., and Watson, E.B., 2003. Diffusion in zircon. In: Hanchar, J.M., Hoskin, P.W.O. (Eds.), *Zircon*. Reviews in Mineralogy and Geochemistry, vol. 53. Mineralogical Society of America, Washington DC, pp. 113–143.

Claiborne, L.L., Miller, C.F., Walker, B.A., Wooden, J.L., Mazdab, F.K., and Bea, F., 2006. Tracking magmatic processes through Zr/Hf ratios in rocks and Hf and Ti zoning in zircons: an example from the Spirit Mountain batholith, Nevada. *Mineralogical Magazine* 70(**5**): 517-543.

Claiborne, L.L., Miller, C.F., Flanagan, D.M., Clynne, M.A., and Wooden, J.L., 2010a. Zircon reveals protracted magma storage and recycling beneath Mount St. Helens. *Geology* 38(**11**): 1011–1014.

Claiborne, L.L., Miller, C.F., and Wooden, J.L., 2010b. Trace element composition of igneous zircon: a thermal and compositional record of the accumulation and evolution of a large silicic batholith, Spirit Mountain, Nevada. *Contributions to Mineralogy and Petrology* 160: 511–531.

Coleman, D.S., Gray, W., and Glazner, A.F., 2004. Rethinking the emplacement and evolution of zoned plutons: geochronologic evidence for incremental assembly of the Tuolumne intrusive suite, California. *Geology* 32(**5**): 433–436.

Colombini, L.L., *et al.*, 2008. Mid-Miocene rhyolite sequence, Highland Range, NV: Record of magma evolution and eruption from the Searchlight Pluton magma chamber. *Eos Trans.* AGU 89(**53**), Abstract V21C-2125.

Colombini, L.L., 2009. *Mid-Miocene Rhyolite Sequence, Highland Range, NV: Record of magma evolution and eruption from the Searchlight Pluton magma chamber.* Master's Thesis, Vanderbilt University, Nashville.

Colombini, L.L., Miller, C.F., Gualda, G.A.R., Wooden, J.L., and Miller, J.S., 2011. Sphene (Titanite) and zircon in the Highland Range Volcanic Sequence (Miocene, southern Nevada, USA): Elemental partitioning, phase relations, and influence on evolution of silicic magma. *Mineralogy and Petrology* (in press).

Corfu, F., Hanchar, J.M., Hoskin, P.W.O., and Kinny, P., 2003. Atlas of zircon textures. In: Hanchar, J.M., Hoskin, P.W.O. (Eds.), *Zircon*. Reviews in Mineralogy and Geochemistry, vol. 53. Mineralogical Society of America, Washington DC, pp. 27–62.

Darling, J., Storey, C., and Hawkesworth, C., 2009. Impact melt sheet zircons and their implications for the Hadean crust. *Geology* 37(**10**): 927-930.

Delvigne, J., Bisdom, E.B.A., Sleeman, J., and Stoops, G., 1979. Olivines, their pseudomorphs and secondary products. *Pedologie* 29(**3**): 247-309.

Duffield, W.A., Bacon, C.R., and Delaney, P.T., 1986. Deformation of poorly consolidated sediment during shallow emplacement of basaltic sill, Coso Range, California. *Bulletin of Volcanology* 48: 97-107.

Falkner, C.M., Miller, C.F., Wooden, J.L., and Heizler, M.T., 1995. Petrogenesis and tectonic significance of the calc-alkaline, bimodal Aztec Wash Pluton, Eldorado Mountains, Colorado River extensional corridor. *Journal of Geophysical Research* 100(**B6**): 10,453-10,476.

Faulds, J.E., Feuerbach, D.L., Miller, C.F., and Smith, E.I., 2001. Cenozoic evolution of the northern Colorado River Extensional Corridor, southern Nevada and northwest Arizona. *Utah Geological Association Publication* 30-*American Association of Petroleum Geologists Publication* GB78, 239-271.

Faulds, J.E., Olson, E.L., Harlan, S.L., and McIntosh, W.C., 2002a. Miocene extension and fault-related folding in the Highland Range, southern Nevada: a three-dimensional perspective. *Journal of Structural Geology* 24(**4**): 861-886.

Faulds, J.E., Bell, J.W., and Olson, E.L., 2002b. *Geologic Map of the Nelson SW Quadrangle, Clark County, Nevada*. U.S. Geological Survey Nelson SW 7.5' Quadrangle.

Ferry, J.M., and Watson, E.B., 2007. New thermodynamic models and revised calibrations for the Ti-in-zircon and Zr-in-rutile thermometers. *Contributions to Mineralogy and Petrology* 154: 429–437.

Feuerbach, D.L., 1998. *Relationships between mid-Miocene volcanism and deformation of the lithosphere in the northern Colorado River extensional corridor.* Ph.D. Dissertation, University of Iowa, Iowa City.

Flinter, B.H., 1959. The magnetic separation of some alluvial minerals in Malaya. *The American Mineralogist* 44(**7-8**): 738-751.

Frost, T.J. and Mahood, G.A., 1987. Field, chemical, and physical constraints on mafic-felsic magma interaction in the Lamarck Granodiorite, Sierra Nevada, California. *Geological Society of America Bulletin* 99: 272-291.

Fu, B. *et al*., 2008. Ti-in-zircon thermometry: applications and limitations. *Contributions to Mineralogy and Petrology* 156: 197-215.

Furman, T., Meyer, P.S., and Frey, F.A., 1992a. Evolution of Icelandic central volcanoes: evidence from the Austurhorn intrusion, southeastern Iceland. *Bulletin of Volcanology* 55: 45-62.

Furman, T., Frey, F.A., and Meyer, P.S., 1992b. Petrogenesis of evolved basalts and rhyolites at Austurhorn, southeastern Iceland: the role of fractional crystallization. *Journal of Petrology* 33: 1405-1445.

Gale, N.H., Moorbath, S., Simons, J., and Walker, G.P.L., 1966. K-Ar ages of acid intrusive rocks from Iceland. *Earth and Planetary Science Letters* 1: 284-288.

Glazner, A.F., Bartley, J.M., Coleman, D.S., Gray, W., and Taylor, R.Z., 2004. Are plutons assembled over millions of years by amalgamation from small magma chambers? *GSA Today* 14: 4–11.

Grimes, C.B. *et al*., 2007. Trace element chemistry of zircons from oceanic crust: a method for distinguishing detrital zircon provenance. *Geology* 35(**7**): 643-646.

Gunnarson, B., Marsh, B.D., and Taylor, H.P., 1998. Generation of Icelandic rhyolites: silicic lavas from the Torfajokull central volcano. *Journal of Volcanology and Geothermal Research* 83: 1-45.

Harper, B.E. *et al.*, 2004. Granites, dynamic magma chamber processes and pluton construction; the Aztec Wash Pluton, Eldorado Mountains, Nevada, USA. *Transactions of the Royal Society of Edinburgh: Earth Sciences* 95(**1-2**): 277-295.

Hayden, L.A., Watson, E.B., and Wark, D.A., 2008. A thermobarometer for sphene (titanite). *Contributions to Mineralogy and Petrology* 155: 529-540.

Hoskin, P.W.O. and Schaltegger, U., 2003. The composition of zircon and igneous and metamorphic petrogenesis. In: Hanchar, J.M., Hoskin, P.W.O. (Eds.), *Zircon*. Reviews in Mineralogy and Geochemistry, vol. 53. Mineralogical Society of America, Washington DC, pp. 27–62.

Hoskin, P.W.O., 2004. Trace-element composition of hydrothermal zircon and the alteration of Hadean zircon from the Jack Hills, Australia. *Geochimica et Cosmochimica Acta* 69(**3**): 637-648.

Kelly, E.A., *et al.*, 2010. Multi-component magma mingling revealed in a rhyolite-dacite-andesite coulee, southern Highland Range (southern Nevada). GSA *Abstracts with Programs* 42(**5**): 471.

Martin, E. and Sigmarsson, O., 2007. Crustal thermal state and origin of silicic magma in Iceland: the case of Torfajökull, Ljósufjöll and Snæfellsjökull volcanoes. *Contributions to Mineralogy and Petrology* 153: 593-605.

Mattson, S.R., Vogel, T.A., and Wilband, J.T., 1986. Petrochemistry of the silicic-mafic complexes at Vesturhorn and Austurhorn, Iceland: evidence for zoned/stratified magma. *Journal of Volcanology and Geothermal Research* 28: 197-223.

Mazdab, F.K., Wooden, J.L., and Barth, A.P., 2007. Trace element variability in titanite from diverse geologic environments. GSA *Abstracts with Programs* 39(**6**): 406.

McPhie, J., Dole, M., and Allen, R., 1993. *Volcanic Textures: A guide to the interpretation of textures in volcanic rocks.* University of Tasmania. Centre for Ore Deposits and Exploration Studies, Hobart, 196 pp.

Michel, J., Baumgartner, L., Putlitz, B., Schaltegger, U., and Ovtcharova, M., 2008. Incremental growth of the Patagonian Torres del Paine laccolith over 90 k.y.. *Geology* 36(**6**): 549-462.

Miller, C.F. and Miller, J.S., (2002). Contrasting stratified plutons exposed in tilt blocks, Eldorado Mountains, Colorado River Rift, NV, USA. *Lithos* 61: 209-224.

Miller, J.S. *et al.*, (2007). Growth, eruption, solidification, fractionation, and rejuvenation of a large felsic magmatic system, Eldorado-Newberry Mountains, Nevada (USA). *IUGG-International Association of Volcanology, Chemistry and the Earth's Interior*, Abstract.

Moorbath, S., Sigurdsson, H., and Goodwin, R., 1968. K-Ar ages of the oldest exposed rocks in Iceland. *Earth and Planetary Science Letters* 4: 197-205.

Olson, E.L., Faulds, J.E., and Harlan, S.S., (1999). *Miocene extension and extension-related folding in the Highland Range, southern Nevada: Implications for hydrocarbon exploration*, Cenozoic Geology of the Northern Colorado River Extensional Corridor, Southern Nevada and Northwestern Arizona: Economic Implications of Regional Segmentation Structures, Nevada Petroleum Society 1999 Field Trip Guidebook, pg. 97-114.

Padilla, A.J., *et al.*, 2010. Death throes of a silicic system: final re-activation of granitic crystal mush and transition to andesitic volcanism, Highland Range, southern Nevada. GSA *Abstracts with Programs* 42(**5**): 472.

Rosenblum, S., 1958. Magnetic susceptibilities of minerals in the Frantz isodynamic magnetic separator. *The American Mineralogist* 43(**1-2**): 170-173.

Smith, K.L., Milnes, A.R., and Eggleton, R.A., 1987. Weathering of basalt: formation of iddingsite. *Clays and Clay Minerals* 35(**6**): 418-428.

Thorarinsson, S.B. and Tegner, C., 2009. Magma chamber processes in central volcanic systems of Iceland: constraints from layered gabbro of the Austurhorn intrusive complex. *Contributions to Mineralogy and Petrology* 158: 223-244.

Vernon, R.H., 1984. Microgranitoid enclaves in granites – globules of hybrid magma quenched in a plutonic environment. *Nature* 309: 438-439.

Vernon, R.H., 1990. Crystallization and Hybridism in Microgranitoid Enclave Magmas: Microstructural Evidence. *Journal of Geophysical Research* 95(**B11**): 17,849-17,859.

Walker, B.A. Jr. *et al*., 2007. Geology and geochronology of the Spirit Mountain batholith, southern Nevada: Implications for timescales and physical processes of batholith construction. *Journal of Volcanology and Geothermal Research* 167: 239-262.

Wark, D.A., and Watson, E.B., 2006. TitaniQ: a titanium-in-quartz geothermometer. *Contributions to Mineralogy and Petrology 152*: 743-754.

Wark, D.A., Hildreth, W., Spear, F.S., Cherniak, D.J., and Watson, E.B., 2007. Pre-eruption recharge of the Bishop magma system. *Geology* 35(**3**): 235-238.

Watson, E.B., Wark, D.A., and Thomas, J.B., 2006. Crystallization thermometers for zircon and rutile. *Contributions to Mineralogy and Petrology* 151: 413-433.

Wiebe, R.A., Manon, M.R., Hawkins, D.P., and McDonough, W.F., 2004. Late-stage mafic injection and thermal rejuvenation of the Vinalhaven Granite, Coastal Maine. *Journal of Petrology* 45(**11**): 2133-2153.

Wiebe, R.A., Wark, D.A., and Hawkins, D.P., 2007. Insights from quartz cathodoluminescence zoning into crystallization of the Vinalhaven granite, coastal Maine. *Contributions to Mineralogy and Petrology* 154: 439-453.

APPENDIX A

Cathodoluminescence (CL) Images of Austurhorn Zircon

Appendix A.1

CL Images of Austurhorn Zircon: sample IA-NS-2

🔴 U-Pb analytical spot 🔵 Trace Element analytical spot

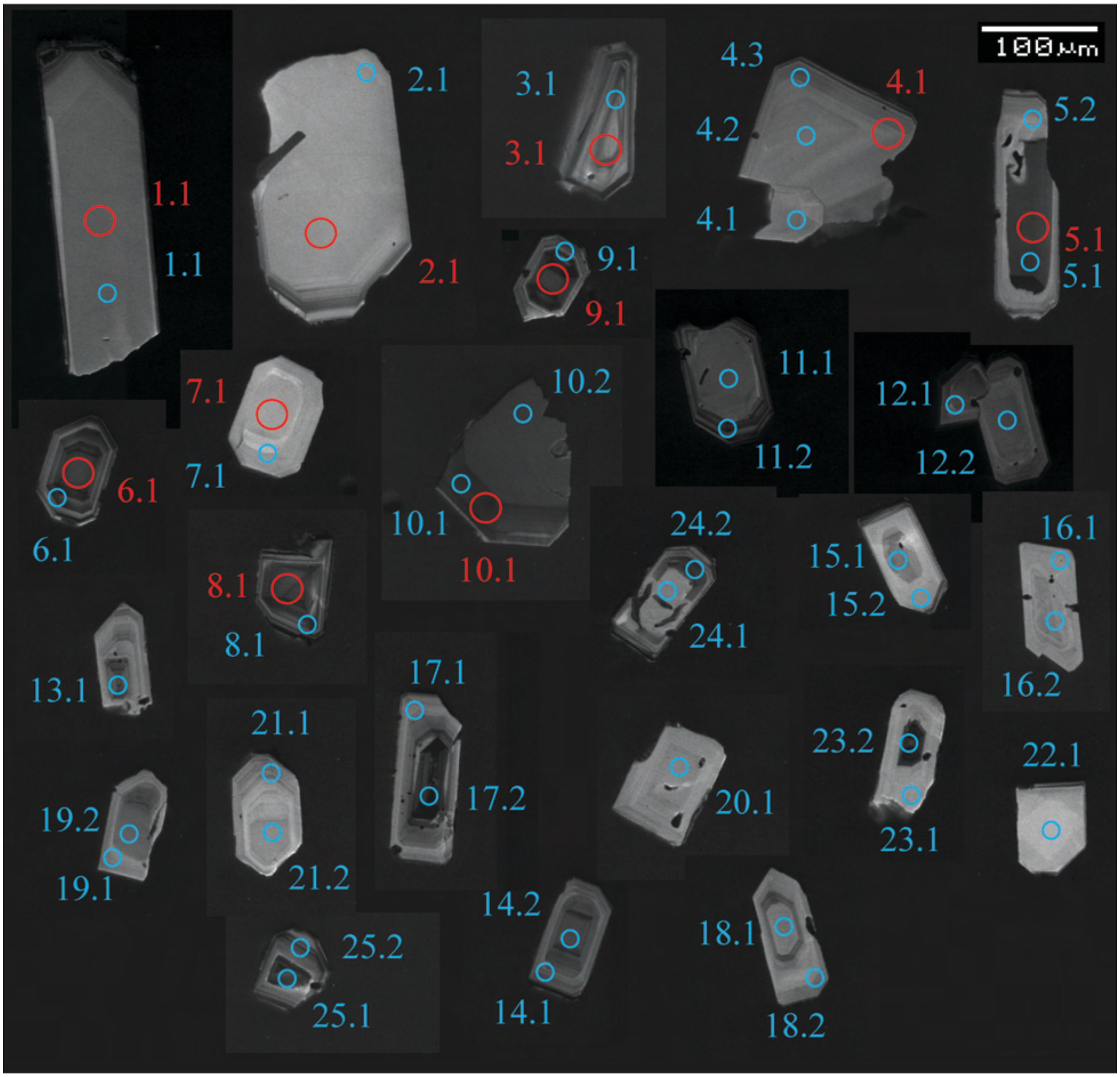

Each spot represents one SHRIMP-RG analysis. Grain labels correspond to individual IA-NS-2 analyses presented in Appendices B.3 (U-Pb) and B.4 (TE).

Appendix A.2

CL Images of Austurhorn Zircon: sample IA-NS-4B

○ U-Pb analytical spot ○○ Trace Element analytical spot*

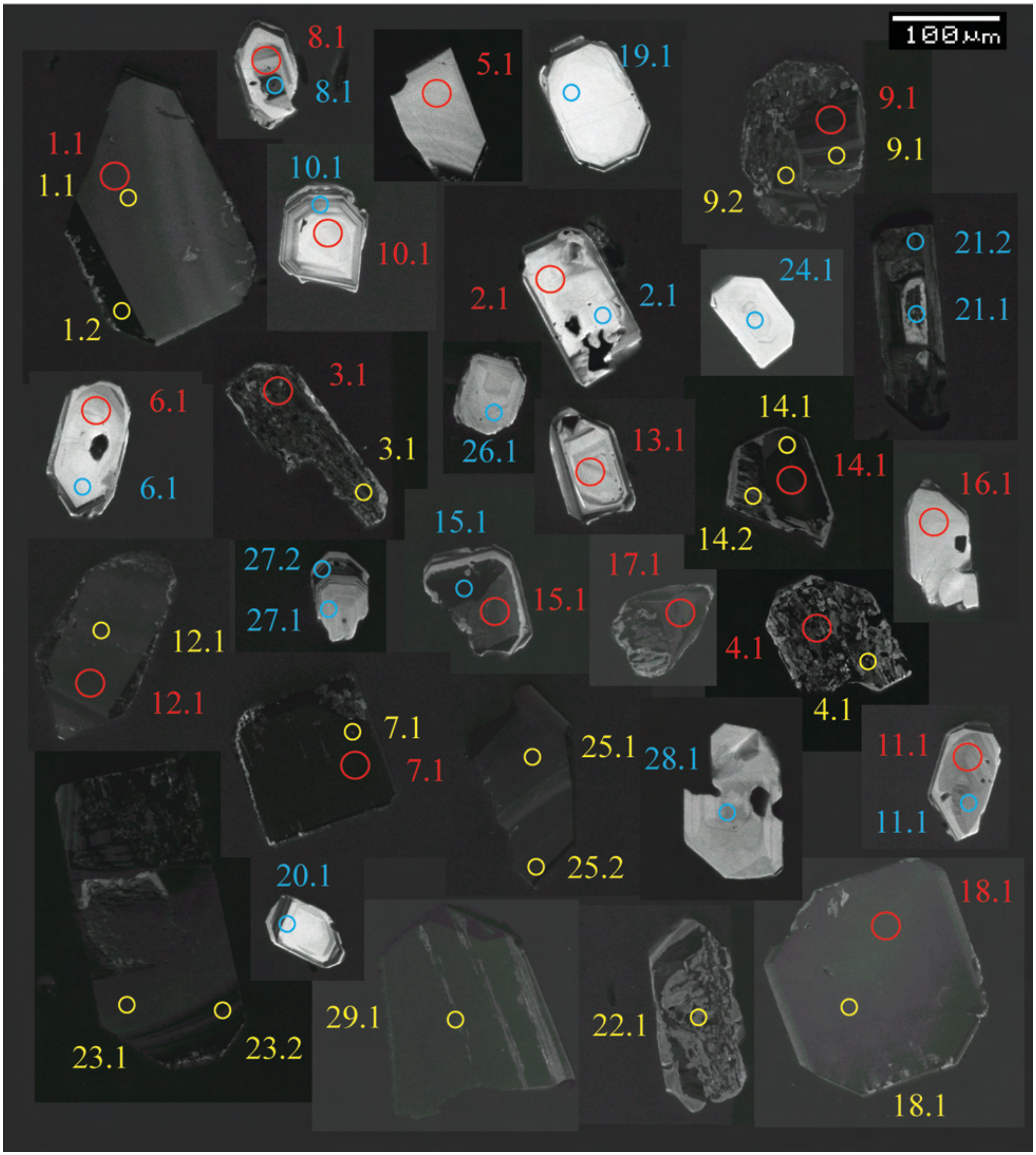

Each spot represents one SHRIMP-RG analysis. Grain labels correspond to individual IA-NS-4B analyses presented in Appendices B.3 (U-Pb) and B.4 (TE). *Groups: 4Ba (blue); 4Bb (yellow).

Appendix A.3

CL Images of Austurhorn Zircon: sample IA-NS-6

○ U-Pb analytical spot ○ Trace Element analytical spot

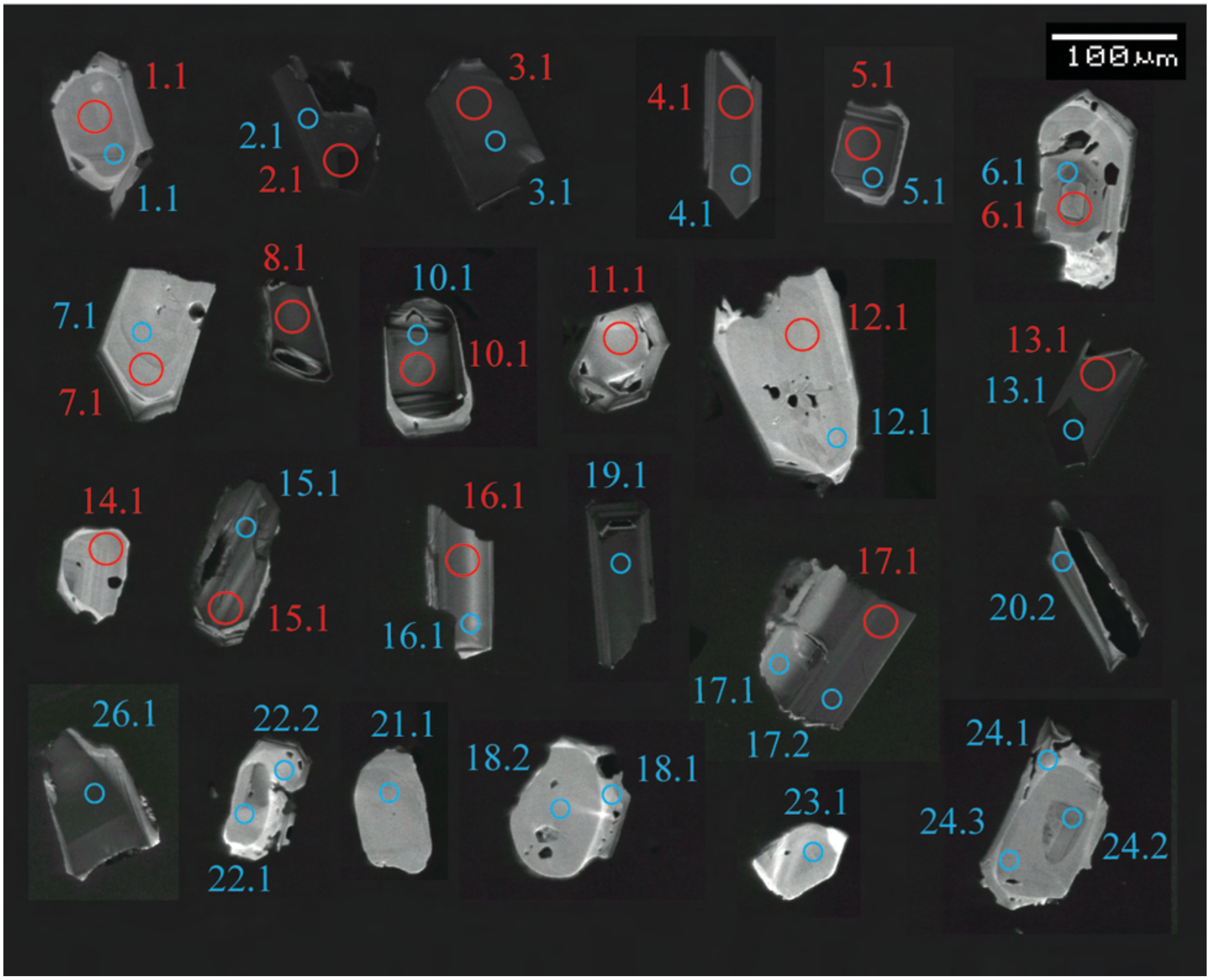

Each spot represents one SHRIMP-RG analysis. Grain labels correspond to individual IA-NS-6 analyses presented in Appendix B.3 (U-Pb) and B.4 (TE).

Appendix A.4

CL Images of Austurhorn Zircon: sample IA-NS-7

○ U-Pb analytical spot ○ Trace Element analytical spot

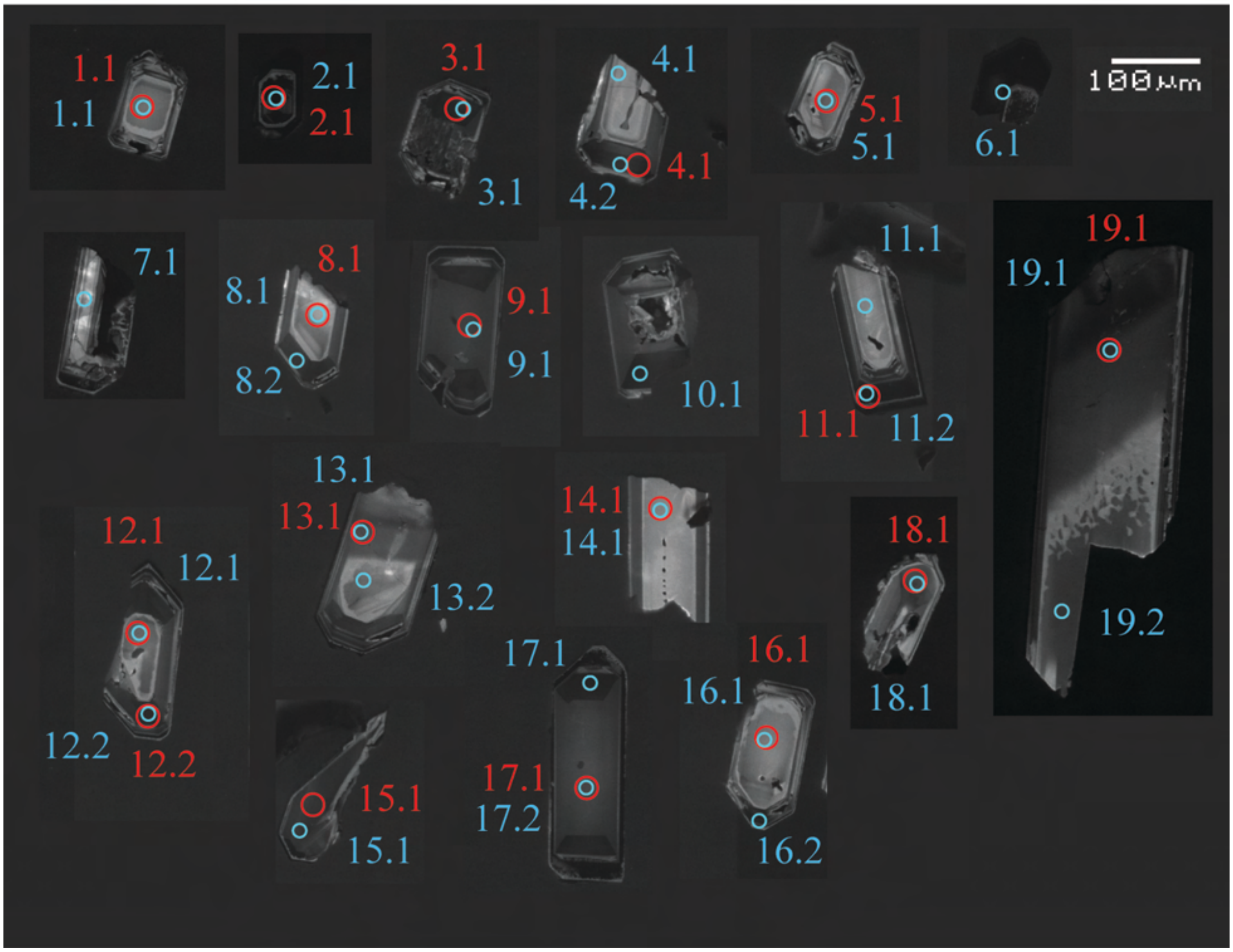

Each spot represents one SHRIMP-RG analysis. Grain labels correspond to individual IA-NS-7 analyses presented in Appendix B.3 (U-Pb) and B.4 (TE).

Appendix A.5

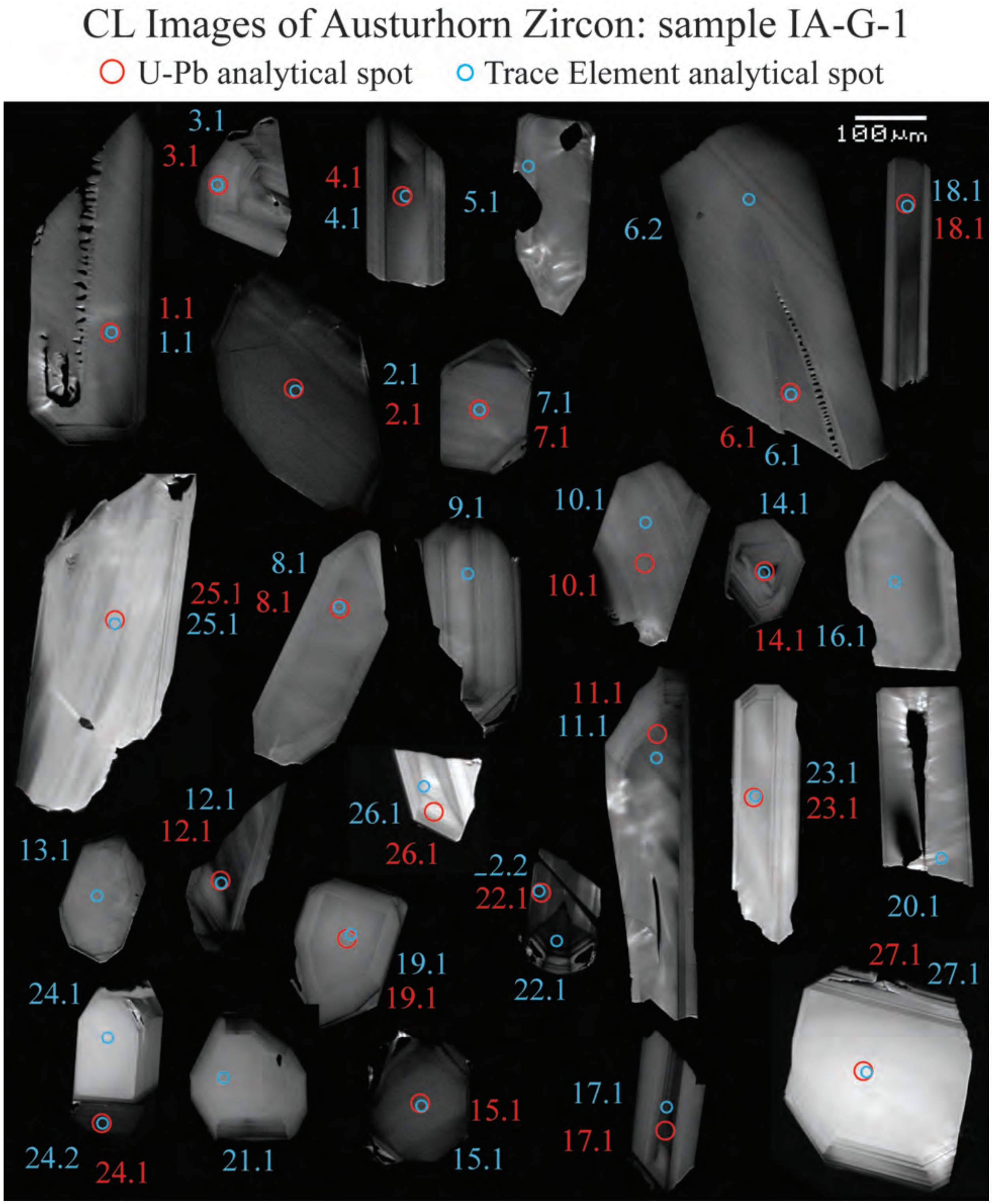

Each spot represents one SHRIMP-RG analysis. Grain labels correspond to individual IA-G-1 analyses presented in Appendix B.3 (U-Pb) and B.4 (TE).

APPENDIX B

Geochemical Data

Appendix B.1

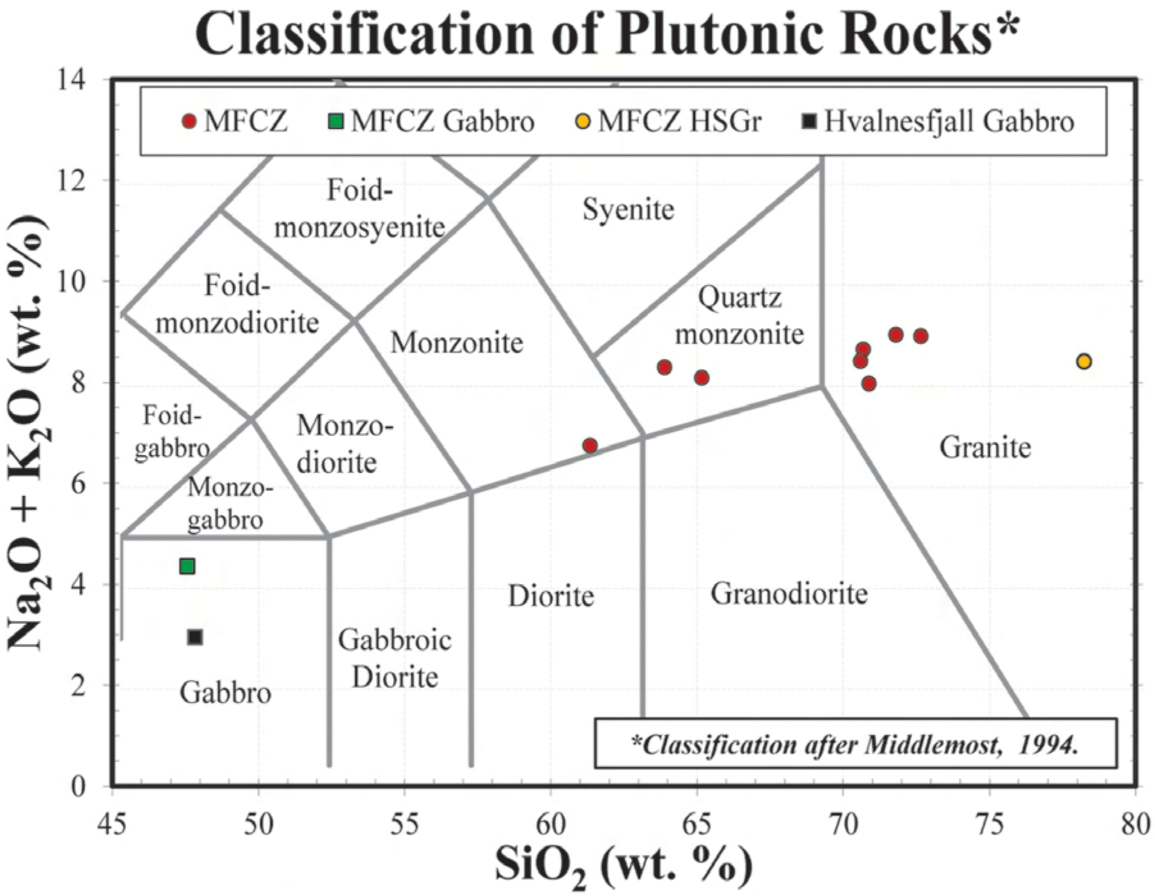

Whole-rock geochemical classification of sampled units from the Austurhorn Intrusive Complex.

Appendix B.2

AUSTURHORN INTRUSIVE COMPLEX
Whole-Rock Major Element Geochemistry

Sample	Rock Type	Major Oxide (wt.%)									
		SiO_2	TiO_2	Al_2O_3	Fe_2O_3	MnO	MgO	CaO	Na_2O	K_2O	P_2O_5
AIC Granophyre											
IA-NS-1	Granophyre	72.37	0.314	13.5	3.63	0.071	0.112	0.96	5.06	3.94	0.030
Mafic -Felsic Composite Zone (MFCZ) Felsic Units											
IA-NS-2	Granophyre	70.59	0.645	13.0	4.53	0.092	0.911	2.08	4.36	3.70	0.072
IA-NS-3	Granodiorite	63.60	1.084	15.7	6.37	0.133	1.258	3.15	5.18	3.20	0.276
IA-NS-4A	Granophyre	70.40	0.390	13.5	5.03	0.154	0.123	1.58	5.34	3.39	0.062
IA-NS-5	Granophyre	70.31	0.540	14.3	3.86	0.061	0.530	1.76	4.24	4.26	0.102
IA-NS-6	Diorite	61.06	1.411	14.7	7.82	0.143	2.383	5.45	4.37	2.46	0.184
IA-NS-7	Granodiorite	64.88	0.867	15.0	7.06	0.153	0.918	2.70	5.33	2.85	0.245
IA-NS-8	Granophyre	71.52	0.412	14.3	3.63	0.031	0.206	0.83	5.68	3.34	0.062
MFCZ High-Si Granophyre											
IA-NS-4B	Granophyre	77.96	0.094	11.7	1.49	0.031	0.000	0.21	4.49	4.00	0.010
MFCZ Coastal Gabbro											
IA-G-1	Gabbro	47.29	4.054	13.0	16.42	0.268	4.312	8.88	3.55	0.89	1.362
AIC Hvalnesfjall Gabbro											
IA-G-3	Gabbro	47.54	1.850	19.9	10.01	0.112	4.374	13.1	2.67	0.37	0.082

Appendix B.3

AUSTURHORN INTRUSIVE COMPLEX
Whole-Rock Trace Element Geochemistry

ELEMENT	Sample										
	IA-NS-1	IA-NS-2	IA-NS-3	IA-NS-4A	IA-NS-4B	IA-NS-5	IA-NS-6	IA-NS-7	IA-NS-8	IA-G-1	IA-G-3
Trace Element Abundance (ppm)											
La	75.9	69.8	56.9	68.6	9.6	62.7	51.6	56.6	66.1	25.8	7.36
Ce	205	172	127	174	100	154	116	128	168	60.2	16.4
Pr	21.8	19.5	15.7	19.6	3.52	16.8	14.5	16.2	18.0	9.37	2.20
Nd	86.5	77.0	65.2	79.1	14.3	65.6	61.1	69.5	69.2	48.0	10.3
Sm	19.6	17.6	14.8	18.4	4.39	14.4	14.3	16.3	14.3	12.8	2.68
Eu	3.94	2.70	4.10	3.91	0.32	2.41	3.45	4.89	2.97	4.64	1.31
Gd	20.2	18.4	14.8	18.2	5.73	15.1	14.3	16.5	14.1	13.4	2.95
Tb	3.40	3.15	2.47	3.17	1.11	2.43	2.41	2.78	2.32	2.02	0.47
Dy	19.6	18.9	13.7	18.3	7.44	14.2	13.8	15.7	13.1	10.8	2.72
Ho	3.96	3.87	2.80	3.69	1.61	2.91	2.77	3.19	2.66	2.04	0.53
Er	11.0	10.9	7.82	10.3	4.92	8.19	7.60	8.90	7.50	5.06	1.39
Yb	10.5	10.4	7.96	10.0	5.53	8.10	7.16	8.58	7.37	3.97	1.12
Lu	1.56	1.48	1.22	1.49	0.80	1.18	1.05	1.30	1.12	0.57	0.16
Ni	1.00	8.00	3.00	1.00	--	2.00	17.0	1.00	--	1.00	55.0
Cu	10.0	14.0	23.0	4.00	5.00	5.00	26.0	10.0	7.00	33.0	147
Zn	107	102	90.0	135	40.0	34.0	110	79.0	25.0	133	55.0
Rb	74.0	77.0	51.0	63.0	67.0	76.0	40.0	51.0	45.0	16.0	5.00
Sr	90.0	96.0	207	146	20.0	136	253	243	125	410	462
Y	109	106	77.2	101	43.7	82.6	77.5	88.1	77.1	56.3	15.2
Zr	874	586	1213	889	369	607	593	1037	816	214	69.0
Nb	107	95.5	58.0	90.2	75.8	69.4	51.7	53.7	74.4	23.8	4.65
Ba	886	481	763	631	138	669	440	552	662	158	81.5
V	10.2	74.0	43.8	3.37	1.15	28.3	143	15.1	7.30	219	355
Cr	2.09	18.3	3.17	0.54	1.26	1.24	31.1	0.53	1.71	1.81	43.8
Ta	6.15	6.41	3.54	5.36	6.09	4.56	3.38	3.48	4.62	1.77	0.33
Hf	21.4	17.8	27.6	23.0	13.7	16.8	15.0	23.9	19.9	6.07	1.96
Pb	14.8	7.14	3.63	6.72	11.5	10.7	5.81	3.64	7.29	1.45	0.91
Th	9.19	9.61	7.22	8.57	9.72	10.3	5.66	5.99	9.45	1.78	0.98
U	6.35	4.69	3.01	3.90	3.96	4.69	1.92	2.23	4.62	0.56	0.31

Appendix B.4

AUSTURHORN INTRUSIVE COMPLEX
SHRIMP-RG Zircon U-Pb Isotope Ratio Data

Spot Name	U (ppm)	^{232}Th/^{238}U	^{238}U/^{206}Pb (Total)	± (%)	^{207}Pb/^{206}Pb (Total)	± (%)	^{206}Pb/^{238}U Age (Ma ^{207}Pb corr)	± (1σ)
IA-NS-2								
IA-NS-2-1.1	61	0.49	1026	6.5	.0756	24.5	**6.06**	**0.42**
IA-NS-2-2.1	43	0.53	1069	8.3	.0987	28.0	**5.64**	**0.51**
IA-NS-2-3.1	231	0.65	1029	3.4	.0590	14.7	**6.16**	**0.22**
IA-NS-2-4.1	210	0.54	992	3.8	.0537	16.7	**6.44**	**0.25**
IA-NS-2-5.1	799	1.16	1003	1.9	.0518	8.7	**6.38**	**0.13**
IA-NS-2-6.1	553	0.85	1018	2.2	.0583	11.2	**6.23**	**0.15**
IA-NS-2-7.1	87	0.52	1012	5.6	.0580	22.6	**6.27**	**0.36**
IA-NS-2-8.1	586	1.12	1038	2.3	.0671	8.9	**6.05**	**0.14**
IA-NS-2-9.1	521	1.12	969	2.2	.0535	9.7	**6.59**	**0.15**
IA-NS-2-10.1	1462	1.04	976	1.3	.0520	6.0	**6.55**	**0.09**
IA-NS-4B								
IA-NS-4B-1.1	1278	0.66	970	1.5	.0480	7.1	**6.63**	**0.10**
IA-NS-4B-2.1	114	0.57	894	5.8	.0631	20.3	**7.06**	**0.43**
IA-NS-4B-3.1	2002	1.48	896	1.3	.1069	10.5	**6.66**	**0.13**
IA-NS-4B-4.1	1583	0.69	881	1.2	.1447	14.8	**6.44**	**0.21**
IA-NS-4B-5.1	114	0.55	1014	5.2	.0675	21.1	**6.19**	**0.34**
IA-NS-4B-6.1	57	0.43	874	7.1	.1090	23.6	**6.81**	**0.54**
IA-NS-4B-7.1	3525	1.64	969	0.9	.0487	4.4	**6.63**	**0.06**
IA-NS-4B-8.1	342	0.58	1007	3.0	.0601	12.3	**6.29**	**0.20**
IA-NS-4B-9.1	2098	2.39	967	1.2	.0504	5.6	**6.63**	**0.08**
IA-NS-4B-10.1	114	0.43	956	5.0	.0766	18.1	**6.49**	**0.34**
IA-NS-4B-11.1	269	0.70	973	3.2	.0538	14.5	**6.56**	**0.22**
IA-NS-4B-12.1	986	2.28	979	1.8	.0569	7.6	**6.50**	**0.12**
IA-NS-4B-13.1	141	0.63	909	4.4	.0496	20.5	**7.06**	**0.32**
IA-NS-4B-14.1	1572	0.82	999	1.4	.0530	6.4	**6.40**	**0.10**
IA-NS-4B-15.1	686	0.82	1000	2.0	.0998	10.1	**6.02**	**0.14**
IA-NS-4B-16.1	95	0.39	1001	5.5	.0493	40.4	**6.41**	**0.38**
IA-NS-4B-17.1	1516	1.09	941	1.3	.0832	23.1	**6.54**	**0.18**
IA-NS-4B-18.1	1144	1.35	999	1.7	.0577	7.1	**6.36**	**0.11**

Appendix B.4 (continued)

AUSTURHORN INTRUSIVE COMPLEX
SHRIMP-RG Zircon U-Pb Isotope Ratio Data (continued)

Spot Name	U (ppm)	^{232}Th/^{238}U	^{238}U/^{206}Pb (Total)	± (%)	^{207}Pb/^{206}Pb (Total)	± (%)	^{206}Pb/^{238}U Age (Ma ^{207}Pb corr)	± (1σ)
IA-NS-6								
IA-NS-6-1.1	91	0.49	1075	5.7	.0887	19.8	**5.68**	**0.35**
IA-NS-6-2.1	1715	1.42	1013	1.4	.0498	6.3	**6.33**	**0.09**
IA-NS-6-3.1	755	0.99	1044	2.1	.0632	8.4	**6.05**	**0.13**
IA-NS-6-4.1	513	1.23	1030	2.6	.0538	12.2	**6.20**	**0.17**
IA-NS-6-5.1	718	0.87	1045	2.0	.0549	9.0	**6.10**	**0.13**
IA-NS-6-6.1	202	0.67	942	3.7	.0357	25.6	**6.93**	**0.27**
IA-NS-6-7.1	91	0.49	1002	5.5	.0392	28.4	**6.49**	**0.37**
IA-NS-6-8.1	674	1.04	1007	2.2	.0586	9.9	**6.30**	**0.14**
IA-NS-6-9.1	849	1.22	1006	1.9	.0604	8.1	**6.29**	**0.13**
IA-NS-6-10.1	502	0.87	1007	2.4	.0527	10.6	**6.35**	**0.16**
IA-NS-6-11.1	112	0.70	987	4.9	.0524	22.4	**6.48**	**0.33**
IA-NS-6-12.1	87	0.44	932	5.4	.0615	22.7	**6.78**	**0.39**
IA-NS-6-13.1	832	1.32	1025	2.0	.0576	8.5	**6.20**	**0.13**
IA-NS-6-14.1	103	0.56	1179	5.3	.0889	19.1	**5.18**	**0.30**
IA-NS-6-15.1	545	1.04	998	2.3	.0531	10.4	**6.40**	**0.16**
IA-NS-6-16.1	358	1.20	987	2.7	.0582	11.0	**6.43**	**0.18**
IA-NS-6-17.1	707	1.10	989	2.0	.0533	9.1	**6.46**	**0.14**
IA-NS-7								
IA-NS-7-1.1	165	0.74	1125	3.7	.0476	17.6	**5.72**	**0.22**
IA-NS-7-2.1	2154	1.48	1065	1.0	.0459	4.9	**6.05**	**0.06**
IA-NS-7-3.1	1607	1.13	1013	1.2	.0493	5.7	**6.33**	**0.08**
IA-NS-7-4.1	1314	1.13	1038	1.4	.0477	6.6	**6.20**	**0.09**
IA-NS-7-5.1	222	0.95	1051	3.2	.0619	13.1	**6.01**	**0.20**
IA-NS-7-8.1	124	0.71	1061	4.1	.0503	18.4	**6.04**	**0.26**
IA-NS-7-9.1	634	0.79	1036	2.0	.0458	9.4	**6.22**	**0.13**
IA-NS-7-11.1	4362	0.92	1001	0.7	.0480	3.9	**6.42**	**0.05**
IA-NS-7-12.1	1144	1.27	1100	1.4	.0464	6.8	**5.86**	**0.09**
IA-NS-7-12.2	1726	1.43	1006	1.2	.0444	5.7	**6.42**	**0.08**
IA-NS-7-13.1	442	0.83	927	2.2	.1541	31.3	**6.04**	**0.43**
IA-NS-7-14.1	140	0.70	1061	3.9	.0464	21.9	**6.07**	**0.25**
IA-NS-7-15.1	1239	1.05	1016	1.5	.0500	7.3	**6.32**	**0.10**
IA-NS-7-16.1	126	0.67	1066	4.1	.0398	20.0	**6.09**	**0.25**
IA-NS-7-17.1	463	0.82	1067	2.2	.0486	10.3	**6.02**	**0.14**
IA-NS-7-18.1	541	1.15	1087	2.0	.0485	9.2	**5.91**	**0.12**
IA-NS-7-19.1	436	0.76	648	2.0	.3786	6.1	**5.90**	**0.31**

Appendix B.4 (continued)

AUSTURHORN INTRUSIVE COMPLEX
SHRIMP-RG U-Pb Isotope Ratio Data (continued)

Spot Name	U (ppm)	^{232}Th/^{238}U	^{238}U/^{206}Pb (Total)	± (%)	^{207}Pb/^{206}Pb (Total)	± (%)	^{206}Pb/^{238}U Age (Ma, ^{207}Pb corr)	± (1σ)
IA-G-1								
IA-G-1-1.1	128	0.74	1068	4.1	.0498	18.5	**6.00**	**0.26**
IA-G-1-2.1	118	0.71	1148	4.4	.0200	46.1	**5.79**	**0.26**
IA-G-1-3.1	76	0.36	1066	5.1	.0573	23.6	**5.96**	**0.32**
IA-G-1-4.1	176	1.01	1180	3.7	.0561	15.9	**5.40**	**0.21**
IA-G-1-6.1	102	0.63	1128	4.6	.0515	27.6	**5.67**	**0.28**
IA-G-1-7.1	92	0.67	1102	4.9	.0586	20.7	**5.76**	**0.30**
IA-G-1-8.1	91	0.71	1111	4.8	.0488	22.4	**5.78**	**0.29**
IA-G-1-10.1	156	0.71	1021	3.8	.0466	17.6	**6.31**	**0.25**
IA-G-1-11.1	147	0.77	987	4.0	.0487	17.4	**6.51**	**0.27**
IA-G-1-12.1	157	0.98	1076	3.7	.0536	16.4	**5.93**	**0.23**
IA-G-1-14.1	133	1.18	1080	4.1	.0545	17.7	**5.91**	**0.25**
IA-G-1-15.1	100	0.69	1176	4.6	.0374	23.4	**5.54**	**0.26**
IA-G-1-17.1	209	1.04	1054	3.6	.0558	15.3	**6.04**	**0.22**
IA-G-1-18.1	184	1.03	1066	3.5	.0616	14.3	**5.93**	**0.22**
IA-G-1-19.1	85	0.71	1042	4.9	.0488	23.0	**6.16**	**0.32**
IA-G-1-22.1	530	1.09	1028	2.0	.0545	8.9	**6.20**	**0.13**
IA-G-1-23.1	116	0.82	1091	4.5	.0412	22.3	**5.94**	**0.27**
IA-G-1-24.1	1244	0.80	1069	1.4	.0495	6.8	**6.00**	**0.09**
IA-G-1-25.1	150	0.69	1152	3.9	.0604	16.1	**5.50**	**0.22**
IA-G-1-26.1	146	1.06	971	3.9	.0471	17.8	**6.63**	**0.27**
IA-G-1-27.1	128	0.70	1114	4.2	.0627	17.4	**5.67**	**0.25**

Appendix B.5

AUSTURHORN INTRUSIVE COMPLEX

SHRIMP-RG Zircon Trace Element Data

Sample:	**IA-NS-2**															
ELEMENT	NS-2-1.1	NS-2-2.1	NS-2-3.1	NS-2-4.1	NS-2-4.2	NS-2-4.3	NS-2-5.1	NS-2-5.2	NS-2-6.1	NS-2-7.1	NS-2-8.1	NS-2-9.1	NS-2-10.1	NS-2-10.2	NS-2-11.1	NS-2-11.2
Trace Element Abundance (ppm)																
La	0.016	0.062	0.087	0.036	0.035	0.015	0.267	0.017	0.041	0.009	0.324	0.020	0.019	0.077	0.059	0.285
Ce	11.8	9.04	150	31.1	21.3	56.1	201	46.4	290	12.0	280	151	178	100	35.7	151
Nd	0.53	4.03	9.01	2.26	4.82	1.89	30.8	2.68	6.72	1.05	7.86	4.17	4.30	9.22	5.77	3.68
Sm	1.92	10.3	22.6	5.91	10.2	7.09	69.7	7.56	18.7	2.70	20.5	12.7	11.8	19.6	13.8	10.5
Eu	0.500	3.97	3.66	1.98	2.78	1.38	7.44	1.84	3.82	1.18	3.92	2.66	1.46	2.43	3.47	1.58
Gd	20.6	86.6	217	59.2	94.8	71.5	537	79.9	194	26.5	203	129	120	189	137	116
Tb	7.89	27.6	75.6	19.9	32.1	27.5	166	28.4	65.1	9.43	68.2	45.9	43.2	65.0	45.9	44.6
Dy	89.5	282	836	220	346	309	1613	311	693	101	737	505	488	742	495	526
Ho	35.8	97.7	321	80.0	127	115	540	116	262	40.5	274	187	196	282	182	208
Er	165	392	1334	318	512	482	2020	477	1002	172	1097	763	849	1224	715	862
Tm	33.0	72.6	256	60.6	90.5	91.5	370	89.2	189	33.8	207	147	175	246	126	170
Yb	259	566	1954	433	651	649	2602	626	1347	256	1521	1083	1372	1878	885	1283
Lu	44.7	94.9	312	68.4	104	98.4	393	98.9	211	44.5	238	175	224	311	139	200
Al	15.2	14.9	14.0	12.3	14.4	17.7	17.8	16.9	15.3	15.3	25.4	10.7	14.9	16.3	9.1	313
Fe	0.355	0.272	0.342	0.861	0.434	0.485	0.412	0.326	0.368	0.366	3.76	0.207	4.19	0.298	0.278	16.2
Hf	11074	8236	10636	8384	8863	10129	8339	9633	10204	9107	11028	11882	11984	11551	8720	13044
Nb	5.03	5.87	108	28.0	15.1	86.9	51.2	36.2	224	10.3	206	95.4	64.5	24.5	27.3	299
Th	17.3	33.7	351	52.9	57.7	158	1042	62.3	887	27.6	768	552	862	656	101	625
Ti	9.22	24.0	8.12	8.88	6.74	7.21	13.4	6.42	11.2	14.0	13.8	12.5	9.29	6.27	5.69	10.6
U	49.6	59.3	439	107	114	290	841	147	719	55.2	695	508	1118	878	177	819
Y	851	2260	7733	1849	2888	2743	12914	2826	5963	945	6280	4419	4905	6891	4072	5074
Ferry & Watson (2007) Temperature [$a_{TiO2} = 0.7$]																
Temp (ºC)	772	877	760	769	742	749	810	738	792	816	814	803	773	736	727	787

Appendix B.5 (continued)

AUSTURHORN INTRUSIVE COMPLEX

SHRIMP-RG Zircon Trace Element Data

Sample:	**IA-NS-2 (Continued)**															
ELEMENT	NS-2-12.1	NS-2-12.2	NS-2-13.1	NS-2-14.1	NS-2-14.2	NS-2-15.1	NS-2-15.2	NS-2-16.1	NS-2-16.2	NS-2-17.1	NS-2-17.2	NS-2-18.1	NS-2-18.2	NS-2-19.1	NS-2-19.2	NS-2-20.1
Trace Element Abundance (ppm)																
La	0.057	0.071	0.86	0.218	0.077	0.044	0.025	0.235	0.57	0.024	0.177	0.029	0.031	0.029	0.249	0.097
Ce	28.6	39.1	141	96.4	117	85.2	36.1	25.2	34.0	43.0	301	45.1	74.2	61.6	64.5	33.4
Nd	4.33	6.31	11.7	3.06	10.2	6.83	1.68	1.41	5.47	2.10	25.5	6.62	3.02	2.94	7.86	6.15
Sm	10.4	15.9	28.8	9.9	28.3	16.4	4.58	3.68	12.2	5.61	59.9	14.3	8.18	7.47	18.8	14.5
Eu	2.92	4.28	8.38	1.86	5.84	4.88	1.11	0.86	3.42	1.31	9.21	3.73	1.88	1.78	4.24	3.90
Gd	107	161	267	100	268	160	47.4	38.1	123	56.4	533	151	87.2	74.2	190	142
Tb	35.0	51.8	83.2	36.0	90.2	54.6	16.7	13.6	41.3	20.0	170	49.7	31.7	26.9	65.3	48.6
Dy	374	557	859	410	960	548	186	156	436	226	1775	533	358	305	704	518
Ho	141	203	305	157	349	199	70.7	59.2	159	84.2	625	198	130	115	256	184
Er	560	792	1146	615	1371	781	287	260	632	343	2362	769	537	463	1009	727
Tm	101	141	201	119	244	137	55.6	51.1	113	65.1	421	138	98.2	87.8	180	131
Yb	695	1003	1423	844	1698	965	408	384	786	470	2920	955	726	627	1232	920
Lu	111	154	215	128	253	145	66.5	64.0	120	72.6	432	151	112	95.6	190	144
Al	13.6	14.8	26.6	59.7	21.1	17.5	18.1	13.5	52.8	15.2	16.3	13.0	14.7	16.7	20.9	27.1
Fe	0.346	2.62	19.4	8.68	0.503	0.408	0.386	0.580	4.30	0.328	0.439	0.275	0.308	0.449	0.860	6.89
Hf	8552	8809	9548	9749	8469	8069	9744	9307	8676	9409	10055	9094	9713	9149	8995	8762
Nb	24.5	30.8	106	130	77.6	66.7	40.0	40.4	28.7	46.0	145	32.0	77.9	63.4	49.4	26.5
Th	75.5	119	436	406	263	156	93.3	31.0	93.7	67.9	740	131	113	75.5	185	100
Ti	7.74	7.09	12.1	8.24	6.65	9.8	6.95	6.98	9.7	7.20	8.02	6.01	6.87	6.96	5.99	7.42
U	136	200	454	529	381	263	159	98.9	166	145	774	212	221	166	308	167
Y	3277	4548	7074	3713	7361	4519	1652	1398	3570	1942	13749	4383	2989	2701	5784	4165
Ferry & Watson (2007) Temperature [a_{TiO2} = 0.7]																
Temp (ºC)	755	747	800	761	741	778	745	746	778	749	759	732	744	745	731	751

Appendix B.5 (continued)

AUSTURHORN INTRUSIVE COMPLEX

SHRIMP-RG Zircon Trace Element Data

Sample:	IA-NS-2 (Continued)									IA-NS-4Ba						
ELEMENT	NS-2-21.1	NS-2-21.2	NS-2-22.1	NS-2-23.1	NS-2-23.2	NS-2-24.1	NS-2-24.2	NS-2-25.1	NS-2-25.2	NS-4Ba-2.1	NS-4Ba-6.1	NS-4Ba-10.1	NS-4Ba-11.1	NS-4Ba-15.1	NS-4Ba-19.1	NS-4Ba-20.1
Trace Element Abundance (ppm)																
La	31.3	0.083	0.016	0.040	43.8	0.067	0.037	27.2	1.00	0.043	0.017	0.023	0.065	0.179	0.030	0.036
Ce	184	50.3	11.9	31.8	502	22.2	171	554	68.1	19.8	6.99	94.5	58.0	951	11.6	14.3
Nd	44.8	6.57	3.75	2.02	73.4	4.84	5.93	57.0	2.57	5.10	1.44	4.24	8.73	14.7	3.56	3.97
Sm	20.6	16.1	8.22	5.14	62.9	10.3	16.3	55.6	5.83	12.1	3.61	12.3	22.1	45.8	8.00	8.70
Eu	2.71	4.19	2.88	1.53	11.9	2.83	2.54	10.2	0.90	4.48	1.59	2.15	6.65	15.1	2.80	3.00
Gd	116	159	68.4	51.2	463	96.3	171	433	68.0	117	34.4	123	219	452	67.0	84.0
Tb	37.9	51.3	21.7	17.9	144	32.5	63.1	140	27.9	36.9	11.4	43.8	70.2	163	22.4	28.5
Dy	404	556	229	198	1449	355	684	1467	335	383	122	462	734	1777	239	297
Ho	144	199	84.3	76.8	508	132	242	522	129	137	47.1	166	255	625	88.9	108
Er	580	765	332	307	1898	519	998	2042	567	536	199	664	990	2297	343	436
Tm	107	138	59.0	56.5	333	93.6	184	374	109	95.2	39.1	128	176	407	62.3	79.4
Yb	761	972	413	414	2308	669	1338	2715	826	670	302	926	1191	2675	435	544
Lu	117	151	67.0	67.7	341	105	209	418	130	107	51.3	146	185	354	70.5	86.5
Al	16.8	15.7	15.7	13.8	14.6	26.7	17.2	2809	31.0	13.4	14.2	11.5	14.5	31.6	11.8	15.2
Fe	2.13	10.3	0.249	0.262	3.35	0.461	0.231	384	5.88	0.361	0.272	0.254	0.283	2.30	0.244	0.375
Hf	9680	8650	8245	8792	8828	8829	10043	10570	12820	8226	7514	9170	7999	8055	8293	8345
Nb	88.9	36.5	6.56	28.2	312	16.0	151	275	146	14.5	11.4	97.5	39.9	1373	7.49	11.3
Th	184	135	31.7	40.5	1290	61.6	513	1119	235	58.0	15.2	354	151	2674	31.2	43.3
Ti	9.5	9.01	8.90	8.75	12.5	6.83	11.3	23.1	5.55	8.44	11.3	10.5	7.79	11.8	7.69	8.39
U	299	211	68.5	93.8	987	119	606	841	461	110	50.8	454	232	1695	66.9	89.6
Y	3478	4490	1829	1729	11495	2990	5570	11923	3045	3046	1132	3731	5777	14492	1991	2595
Ferry & Watson (2007) Temperature [a_{TiO2} = 0.7]																
Temp (ºC)	776	770	769	767	803	744	793	872	725	764	793	786	756	797	755	763

Appendix B.5 (continued)

AUSTURHORN INTRUSIVE COMPLEX

SHRIMP-RG Zircon Trace Element Data

Sample:	**IA-NS-4Ba (Continued)**							**IA-NS-4Bb**								
ELEMENT	NS-4Ba-21.1	NS-4Ba-21.2	NS-4Ba-24.1	NS-4Ba-26.1	NS-4Ba-27.1	NS-4Ba-27.2	NS-4Ba-28.1	NS-4Bb-1.1	NS-4Bb-1.2	NS-4Bb-3.1	NS-4Bb-4.1	NS-4Bb-7.1	NS-4Bb-9.1	NS-4Bb-9.2	NS-4Bb-12.1	NS-4Bb-14.1
Trace Element Abundance (ppm)																
La	0.452	17.3	0.072	0.011	0.035	42.4	0.018	1.21	2.23	15.5	1.80	0.288	0.035	0.252	0.506	0.223
Ce	591	272	12.7	15.9	21.6	669	9.46	49.9	418	82.7	111	385	81.8	96.2	129	145
Nd	6.78	4.94	4.34	1.68	3.90	56.9	1.49	26.4	123	3.54	4.81	41.0	2.81	7.76	50.9	30.6
Sm	16.9	4.99	9.6	4.12	9.17	40.1	3.38	48.9	183	5.56	17.0	116	12.4	24.5	107	75.0
Eu	3.38	0.62	2.81	1.04	3.15	6.70	1.49	1.15	4.36	0.243	0.70	3.70	0.66	0.86	2.85	1.79
Gd	169	44.1	89.4	42.2	91.4	280	33.9	274	880	48.3	159	777	114	198	575	443
Tb	76.8	25.7	30.8	15.2	30.7	93.9	11.7	119	317	28.2	79.6	370	61.9	102	228	176
Dy	1007	404	324	166	320	1033	128	1241	3056	371	988	4015	771	1245	2283	1750
Ho	436	235	117	64.5	120	384	49.5	401	921	165	355	1274	283	467	705	532
Er	2062	1355	472	288	476	1528	200	1593	3218	815	1545	4840	1322	2052	2616	1978
Tm	448	381	86.3	56.8	85.9	285	39.7	325	601	197	339	977	310	469	524	376
Yb	3373	3569	626	432	603	2014	292	2353	3947	1631	2665	7140	2554	3720	3769	2619
Lu	467	595	103	71.0	94.6	294	48.4	308	492	235	368	924	376	535	488	333
Al	616	389	15.0	13.4	12.5	110	15.6	19.5	18.6	20.3	14.9	12.5	14.4	46.5	16.0	11.4
Fe	33.5	829	0.302	0.202	0.263	2.62	0.264	3.22	8.58	106	5.09	1.22	0.551	2.10	2.15	1.30
Hf	8007	13113	8926	9144	8213	8916	7824	16898	22578	24018	22139	22628	21137	17930	21201	20815
Nb	369	1423	10.5	25.2	20.2	445	11.1	300	3272	594	643	1087	497	634	329	905
Th	745	3933	65.3	39.3	63.7	918	44.6	725	7063	962	1828	5273	2303	1887	1529	1969
Ti	6.86	14.0	10.8	10.5	7.79	15.0	14.2	5.49	24.3	8.40	2.75	2.92	3.58	5.45	6.49	7.64
U	1074	1298	112	104	116	819	78.4	1065	3985	1878	1262	2984	1710	1827	763	1709
Y	12095	8153	2532	1602	2736	8783	1129	5457	12779	2983	4156	15985	3008	5422	9637	7907
Ferry & Watson (2007) Temperature [$a_{TiO2} = 0.7$]																
Temp (ºC)	744	816	789	786	756	823	817	724	878	763	665	670	686	723	739	754

Appendix B.5 (continued)

AUSTURHORN INTRUSIVE COMPLEX

SHRIMP-RG Zircon Trace Element Data

Sample:	**IA-NS-4Bb (Continued)**								**IA-NS-6**							
ELEMENT	NS-4Bb-14.2	NS-4Bb-22.1	NS-4Bb-23.1	NS-4Bb-23.2	NS-4Bb-25.1	NS-4Bb-25.2	NS-4Bb-29.1	NS-4Bb-18.1	NS-6-1.1	NS-6-2.1	NS-6-3.1	NS-6-4.1	NS-6-5.1	NS-6-6.1	NS-6-7.1	NS-6-9.1
Trace Element Abundance (ppm)																
La	4.32	0.214	0.100	0.085	0.932	0.351	0.74	0.203	0.022	0.374	0.372	0.304	0.129	0.028	0.023	0.366
Ce	124	34.7	89.7	213	132	107	1763	94.4	37.6	528	495	184	300	95.9	17.5	451
Nd	25.4	0.870	6.45	16.7	59.6	33.0	26.4	9.19	2.37	45.6	39.1	40.9	16.6	4.39	1.31	38.8
Sm	35.0	3.31	22.1	54.1	119	75.6	52.2	27.7	6.48	92.5	82.5	77.7	42.9	11.8	3.40	79.7
Eu	0.85	0.216	0.88	1.91	2.79	2.24	5.99	1.13	1.96	13.9	11.8	20.6	2.96	3.52	1.14	11.2
Gd	144	33.2	187	419	596	461	435	224	65.9	697	670	549	384	122	36.2	625
Tb	45.6	17.9	94.0	203	233	197	185	115	22.2	214	209	160	125	42.4	13.8	194
Dy	440	250	1179	2405	2249	2059	2337	1417	238	2122	2121	1522	1296	444	160	1970
Ho	149	111	450	834	627	673	927	510	87.9	731	733	490	475	161	64.1	684
Er	546	516	2005	3473	2287	2572	4129	2243	355	2741	2796	1761	1801	611	276	2606
Tm	110	125	465	738	441	528	969	504	68.4	493	520	309	333	111	55.6	476
Yb	803	1044	3736	5624	3109	3783	8453	3955	486	3405	3667	2120	2364	751	423	3391
Lu	106	169	556	771	393	505	1225	566	76.2	507	530	299	366	114	71.8	500
Al	24.4	20.9	11.4	12.7	17.4	16.6	18.5	16.8	16.0	15.0	15.2	13.6	11.9	10.2	14.2	14.2
Fe	33.3	15.1	0.849	0.508	4.09	2.08	2.93	1.08	0.368	0.555	0.501	0.379	0.735	0.347	0.338	0.423
Hf	19398	18342	18920	22353	18104	19579	21483	21589	8638	7161	7708	7240	9165	8191	8431	8501
Nb	496	191	316	651	505	491	973	449	35.2	83.3	82.2	39.8	208	88.8	39.1	74.0
Th	901	821	1919	2928	1632	1619	5758	2020	108	1072	1082	500	1590	324	23.8	1182
Ti	4.77	1.87	2.58	2.14	5.38	7.28	7.50	3.71	10.0	14.3	12.7	27.8	14.3	10.4	7.77	14.7
U	758	690	812	1651	1486	1209	693	1184	162	956	898	449	1306	367	94.7	906
Y	3156	1291	4753	9885	9612	9209	31162	5826	2098	17041	17707	11322	11160	3628	1473	15701
Ferry & Watson (2007) Temperature [a_{TiO2} = 0.7]																
Temp (ºC)	711	635	660	646	722	750	752	689	781	818	805	894	818	784	756	820

Appendix B.5 (continued)

AUSTURHORN INTRUSIVE COMPLEX

SHRIMP-RG Zircon Trace Element Data

Sample:	**IA-NS-6**															
ELEMENT	NS-6-10.1	NS-6-12.1	NS-6-13.1	NS-6-15.1	NS-6-16.1	NS-6-17.1	NS-6-17.2	NS-6-18.1	NS-6-18.2	NS-6-19.1	NS-6-20.2	NS-6-21.1	NS-6-22.1	NS-6-22.2	NS-6-23.1	NS-6-24.1
Trace Element Abundance (ppm)																
La	0.036	0.019	0.129	0.171	0.117	0.111	0.321	0.030	0.019	0.480	0.212	0.023	0.025	0.023	12.3	0.013
Ce	86.9	17.5	594	222	75.5	81.0	328	15.6	16.9	376	132	17.7	16.1	19.7	49.8	18.0
Nd	4.58	3.49	29.4	25.0	14.8	10.3	36.6	0.94	3.40	49.9	23.3	1.36	1.68	1.39	13.5	2.73
Sm	13.5	8.69	69.3	47.2	32.1	22.8	73.3	2.82	8.65	90.9	51.8	3.91	4.71	3.64	7.62	6.26
Eu	1.86	2.55	11.3	8.17	8.83	4.99	13.2	0.97	2.56	15.6	11.9	1.48	1.57	1.25	2.65	1.79
Gd	131	79.0	509	372	247	181	565	31.3	77.1	642	397	39.4	49.5	37.1	52.9	55.2
Tb	42.7	26.5	153	117	78.3	59.2	174	11.2	26.0	196	119	14.0	16.3	14.4	17.9	18.3
Dy	463	286	1461	1174	787	599	1723	135	277	1888	1206	159	187	165	198	201
Ho	167	102	504	414	276	215	604	53.6	97.9	649	425	60.3	67.8	68.3	74.3	76.9
Er	693	404	1881	1568	1077	854	2279	236	382	2366	1595	260	269	303	280	312
Tm	135	71.3	341	288	203	160	415	47.7	70.6	433	294	50.6	51.2	60.8	57.0	60.9
Yb	970	513	2365	2051	1491	1178	2922	382	501	3006	2086	371	377	505	415	458
Lu	159	80.6	353	306	241	183	440	67.3	78.9	442	325	62.5	62.4	86.9	65.1	76.5
Al	11.5	15.5	13.8	11.5	12.3	13.1	14.6	27.2	16.9	13.8	163	15.3	19.4	15.7	16.4	11.3
Fe	0.284	0.546	0.315	0.449	0.309	6.61	0.273	5.57	0.450	0.383	0.453	0.346	0.366	0.354	2.79	0.195
Hf	9056	8730	7641	7834	8466	8158	7880	8772	8665	7728	8730	8218	8719	8476	7702	8668
Nb	57.9	12.1	207	42.3	18.2	15.3	60.5	8.86	9.9	59.6	38.5	28.1	11.9	11.6	17.6	8.23
Th	497	39.6	3199	512	294	320	793	33.6	41.6	964	513	50.3	40.2	48.9	79.1	43.3
Ti	14.9	6.73	40.2	13.3	22.3	15.3	14.8	21.1	6.95	18.4	21.9	9.73	8.19	21.2	15.7	18.3
U	554	86.9	1810	526	302	374	686	71.7	80.5	777	442	107	88.7	93.5	114	79.7
Y	4097	2326	11708	9679	6125	4265	13992	1372	2156	14369	9805	1409	1430	1635	1693	1779
Ferry & Watson (2007) Temperature [$a_{\mathrm{TiO2}} = 0.7$]																
Temp (ºC)	822	742	942	810	868	825	822	861	745	845	866	778	761	862	828	845

Appendix B.5 (continued)

AUSTURHORN INTRUSIVE COMPLEX

SHRIMP-RG Zircon Trace Element Data

Sample:	**IA-NS-6 (Continued)**			**IA-NS-7**												
ELEMENT	NS-6-24.2	NS-6-24.3	NS-6-26.1	NS-7-1.1	NS-7-2.1	NS-7-3.1	NS-7-4.1	NS-7-4.2	NS-7-5.1	NS-7-6.1	NS-7-7.1	NS-7-8.1	NS-7-8.2	NS-7-9.1	NS-7-10.1	NS-7-11.1
Trace Element Abundance (ppm)																
La	0.562	0.151	0.329	0.083	0.079	0.145	0.021	0.016	0.221	0.98	0.357	0.070	0.081	0.260	0.203	0.74
Ce	41.1	23.6	293	24.0	559	451	11.7	217	58.4	220	14.0	21.2	339	290	787	19.3
Nd	5.82	1.85	37.3	8.99	14.3	18.5	3.44	9.7	25.7	7.24	2.80	8.85	13.9	28.3	37.2	7.74
Sm	14.7	4.34	74.2	23.0	46.2	47.3	7.68	25.7	48.3	18.3	7.09	20.4	37.6	62.2	93.7	16.6
Eu	4.47	1.37	6.17	7.99	3.08	3.96	2.37	2.38	15.1	1.62	1.97	6.62	3.30	5.46	7.55	5.95
Gd	139	43.6	586	187	440	403	60.1	222	346	174	57.8	161	331	499	694	141
Tb	45.5	14.8	186	59.2	157	135	20.5	76.7	107	71.4	19.6	50.6	108	162	214	45.7
Dy	472	164	1876	592	1673	1401	217	792	1044	911	204	510	1110	1662	2028	460
Ho	179	61.5	647	213	597	481	79.1	273	342	400	73.7	174	388	569	658	164
Er	667	253	2454	810	2352	1901	313	1082	1275	1860	313	669	1467	2210	2410	655
Tm	123	47.1	450	150	433	348	62.3	203	226	434	59.9	125	272	397	409	122
Yb	841	346	3204	1136	3123	2488	455	1465	1643	3657	467	942	1954	2847	2952	935
Lu	134	57.6	486	182	455	370	78.1	230	251	558	76.0	151	295	428	421	150
Al	93.6	13.6	13.2	1.10	3.92	30.8	1.79	2.46	2.05	41.7	238	2.11	1.98	58.2	2.74	975
Fe	113	1.24	0.375	3.00	3.80	4.58	2.97	3.04	3.13	25.4	108	3.00	3.07	3.50	3.63	130
Hf	8221	8627	8056	7926	10290	6789	8196	7180	7411	15425	8366	8146	7162	6353	6127	8042
Nb	39.7	19.2	72.8	11.9	453	279	4.57	153	21.9	89.7	8.03	8.88	239	82.3	394	12.3
Th	92.5	35.3	1088	133	3769	1098	35.2	1000	258	3606	47.2	108	1305	523	2682	98.8
Ti	16.9	9.82	12.9	17.9	17.6	21.8	13.7	13.3	19.4	6.34	13.9	15.1	17.0	8.45	28.3	16.2
U	156	80.9	993	190	2992	1342	72.8	1093	284	3230	80.9	163	1270	704	2243	156
Y	3904	1410	14934	4901	14503	11321	1899	6497	7789	12165	1870	4291	8984	13451	15246	3752
Ferry & Watson (2007) Temperature [$a_{\mathrm{TiO2}} = 0.7$]																
Temp (ºC)	836	779	807	842	841	865	813	810	852	737	814	824	836	764	897	831

Appendix B.5 (continued)

AUSTURHORN INTRUSIVE COMPLEX

SHRIMP-RG Zircon Trace Element Data

Sample:	**IA-NS-7 (Continued)**														**IA-G-1**	
ELEMENT	NS-7-11.2	NS-7-12.1	NS-7-12.2	NS-7-13.1	NS-7-13.2	NS-7-14.1	NS-7-15.1	NS-7-16.1	NS-7-16.2	NS-7-17.1	NS-7-17.2	NS-7-18.1	NS-7-19.1	NS-7-19.2	G-1-1.1	G-1-2.1
Trace Element Abundance (ppm)																
La	0.131	0.148	0.138	0.89	0.132	0.082	0.424	0.101	0.140	0.114	0.195	0.091	1.03	0.197	0.030	0.037
Ce	361	539	525	150	47.7	15.1	462	21.7	700	769	204	105	136	57.1	10.5	12.3
Nd	6.55	30.1	22.9	13.5	18.9	6.49	40.2	9.6	21.0	30.7	22.5	12.3	13.5	23.7	3.69	3.50
Sm	21.8	77.9	60.7	35.6	46.0	17.9	88.8	20.4	61.0	77.5	48.8	38.3	31.6	50.6	7.58	7.43
Eu	1.72	7.59	5.68	3.46	15.7	6.46	8.56	6.31	5.51	6.24	3.79	11.1	2.96	16.5	3.14	3.11
Gd	262	588	501	341	372	155	732	160	560	655	397	298	278	364	70.3	70.4
Tb	114	175	155	113	116	50.7	244	50.5	189	202	129	89.8	94.3	111	24.1	25.4
Dy	1406	1652	1524	1223	1145	525	2518	508	1949	1941	1326	846	1009	1070	257	278
Ho	564	532	497	434	382	185	875	177	681	638	470	265	375	348	90.5	102
Er	2506	1978	1888	1694	1464	746	3300	688	2634	2375	1772	954	1437	1252	392	424
Tm	520	338	332	319	266	138	590	125	475	422	320	162	275	218	75.0	80.5
Yb	3973	2349	2354	2308	1952	1030	4183	928	3410	2953	2304	1126	1984	1528	558	615
Lu	568	344	345	359	301	170	610	150	503	426	348	158	315	228	90.6	102
Al	281	2.35	15.3	18.7	2.35	1.92	3.21	5.40	4.10	2.39	1.62	9.34	571	2.58	5.06	3.99
Fe	32.1	3.48	4.63	4.06	2.91	2.95	3.76	3.37	3.65	3.64	3.27	3.36	96.4	3.78	4.28	3.98
Hf	13324	6807	6986	7550	7323	7923	8825	7969	9135	6355	6342	6523	7008	7181	9519	9767
Nb	718	299	254	57.8	24.4	9.42	107	7.40	342	435	64.1	59.0	51.8	22.7	1.38	1.72
Th	5164	2247	2430	482	306	117	1444	116	3190	2428	457	697	385	242	97.2	108
Ti	15.5	36.0	25.5	8.96	20.7	17.1	9.25	15.8	19.2	27.9	8.59	38.2	8.61	19.2	14.9	12.8
U	5933	1684	1763	606	316	178	1331	175	2057	2117	579	650	545	283	144	158
Y	15666	12385	11714	9942	8564	4247	20787	3982	15396	15022	10735	6067	8780	7941	2178	2445
Ferry & Watson (2007) Temperature [a_{TiO2} = 0.7]																
Temp (ºC)	827	927	884	770	859	838	773	829	851	895	766	935	766	850	822	806

Appendix B.5 (continued)

AUSTURHORN INTRUSIVE COMPLEX

SHRIMP-RG Zircon Trace Element Data

Sample:	IA-G-1 (Continued)															
ELEMENT	G-1-3.1	G-1-4.1	G-1-5.1	G-1-6.1	G-1-6.2	G-1-7.1	G-1-8.1	G-1-9.1	G-1-10.1	G-1-11.1	G-1-12.1	G-1-13.1	G-1-14.1	G-1-15.1	G-1-16.1	G-1-17.1
Trace Element Abundance (ppm)																
La	0.008	0.092	0.035	0.013	0.008	0.016	0.049	0.022	0.035	0.080	0.132	0.028	0.035	0.050	0.016	0.078
Ce	8.88	13.2	5.60	13.2	8.44	10.6	10.0	9.49	11.6	11.3	20.2	6.91	20.1	11.4	4.62	21.9
Nd	0.90	4.52	2.75	2.70	1.58	3.22	3.68	3.82	3.52	3.98	6.46	2.44	3.06	3.46	2.32	7.61
Sm	2.53	8.52	6.10	6.58	4.99	6.39	7.66	8.31	6.97	8.98	17.8	5.39	7.39	7.46	5.05	21.1
Eu	1.07	3.97	3.41	1.73	1.75	2.52	3.53	3.71	2.71	4.20	7.90	2.43	3.63	2.95	2.57	9.8
Gd	24.0	104	60.9	55.9	36.0	61.4	77.4	69.2	69.5	88.1	175	46.1	70.4	62.7	42.0	190
Tb	8.86	40.1	21.9	19.8	12.7	21.5	25.3	22.5	23.8	31.1	58.3	15.8	24.0	20.9	14.4	61.9
Dy	105	474	229	209	139	239	263	229	262	334	606	170	253	237	152	634
Ho	45.2	183	81.7	74.9	52.2	84.8	93.8	82.0	100	123	215	62.5	94.1	89.9	53.2	218
Er	208	788	348	319	211	365	393	326	414	508	862	255	390	370	223	870
Tm	44.3	147	64.8	58.8	41.9	69.3	71.7	62.5	78.5	95.8	159	49.7	72.3	68.6	42.3	162
Yb	358	1097	512	446	321	527	531	470	591	726	1177	379	548	512	334	1184
Lu	65.5	177	84.3	70.0	53.7	85.2	86.6	76.9	93.9	118	186	60.9	89.2	84.6	57.0	190
Al	2.52	2.36	4.44	9.92	3.00	2.05	3.54	2.34	2.19	4.88	2.86	2.22	5.51	0.88	21.7	2.28
Fe	3.76	3.78	3.82	3.56	3.98	3.64	3.98	3.72	3.57	4.06	3.93	3.71	3.68	2.85	3.60	3.63
Hf	9393	8629	9059	9917	10347	9728	9155	8733	9781	9269	8823	9640	8418	9573	9026	8536
Nb	2.28	3.18	0.89	0.96	1.08	1.05	1.45	1.44	1.44	1.68	3.71	0.76	2.57	1.43	0.63	4.24
Th	32.6	220	59.2	85.0	44.3	76.3	72.6	47.6	93.1	108	197	35.7	222	94.5	31.0	198
Ti	17.1	21.5	19.8	9.37	11.5	14.7	18.4	19.8	14.0	19.1	21.0	16.9	31.6	12.1	17.9	24.6
U	100	237	92.3	137	76.9	119	106	74.3	139	144	216	60.5	187	143	51.4	204
Y	1119	4000	1900	1735	1350	2072	2261	1980	2440	2863	5003	1467	2273	2157	1278	5197
Ferry & Watson (2007) Temperature [a_{TiO2} = 0.7]																
Temp (ºC)	838	863	854	774	794	821	846	854	815	850	861	836	910	800	842	879

Appendix B.5 (continued)

AUSTURHORN INTRUSIVE COMPLEX

SHRIMP-RG Zircon Trace Element Data

Sample:	**IA-G-1 (Continued)**											
ELEMENT	G-1-18.1	G-1-19.1	G-1-20.1	G-1-21.1	G-1-22.1	G-1-22.2	G-1-23.1	G-1-24.1	G-1-24.2	G-1-25.1	G-1-26.1	G-1-27.1
	Trace Element Abundance (ppm)											
La	0.089	0.051	0.014	0.059	0.053	0.137	0.084	0.045	0.041	0.152	0.029	0.033
Ce	17.1	9.15	8.89	8.90	88.6	56.4	13.1	11.8	116	10.9	25.8	7.84
Nd	5.33	3.80	2.23	3.19	3.90	11.0	4.36	3.08	3.88	2.70	2.67	2.60
Sm	11.6	7.90	5.20	6.62	13.3	28.5	12.4	6.28	11.5	6.62	7.00	6.80
Eu	6.00	3.69	2.14	3.04	4.30	9.23	5.87	2.48	1.80	2.29	3.72	3.27
Gd	152	80.9	46.1	60.3	142	252	126	63.5	121	59.2	74.6	68.8
Tb	55.1	27.6	15.3	21.5	53.5	86.1	42.0	22.0	45.2	21.7	26.4	23.2
Dy	602	297	162	232	569	903	432	233	514	236	282	249
Ho	222	106	61.2	83.3	210	316	155	89.2	192	87.1	102	91.5
Er	914	431	243	342	888	1298	643	371	836	385	424	383
Tm	167	81.1	47.7	64.8	170	244	116	69.8	166	71.7	78.9	71.6
Yb	1227	606	355	496	1297	1815	880	527	1224	561	588	564
Lu	196	101	56.8	80.9	205	276	139	86.0	186	91.4	96.1	91.7
Al	1.02	7.18	3.18	3.88	6.98	3.01	3.35	3.39	1.63	7.63	1.53	5.68
Fe	2.33	3.60	2.98	2.93	3.26	3.36	3.48	3.47	3.56	3.73	2.71	2.88
Hf	8592	9078	10002	9301	9973	10149	8656	9797	11878	10938	8256	9837
Nb	3.76	1.57	1.14	1.13	9.05	4.87	2.38	1.42	11	1.03	3.17	1.29
Th	234	82.2	41.4	58.5	1143	798	131	100	846	129	231	101
Ti	21.3	19.4	13.6	17.5	15.6	10.4	23.7	11.2	9.29	8.84	31.8	14.2
U	242	115	72.2	93.3	1123	755	160	150	1247	204	197	155
Y	5227	2446	1572	1981	5021	7450	3976	2152	4731	2061	2455	2288
	Ferry & Watson (2007) Temperature [a_{TiO2} = 0.7]											
Temp (ºC)	862	852	812	840	827	784	875	792	773	768	911	817

Appendix B.6

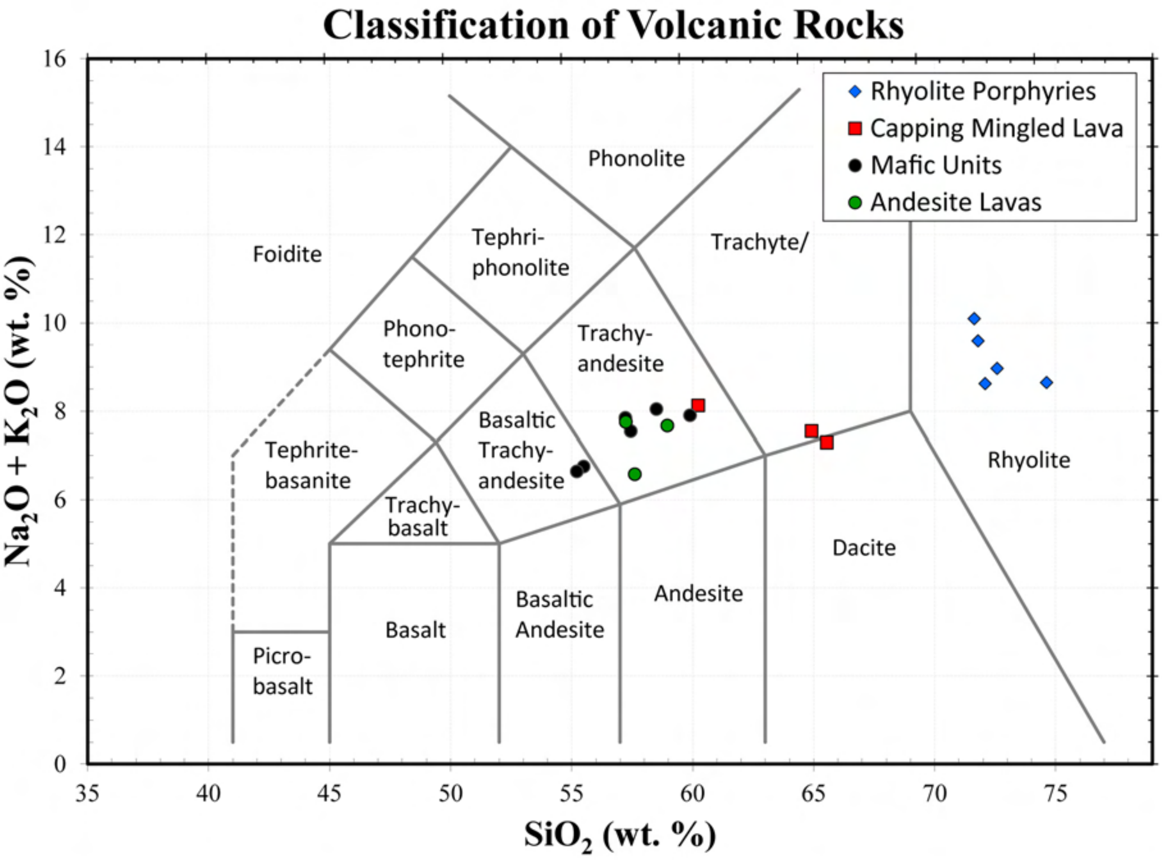

Whole-rock geochemical classification of sampled units from the Highland Range Silicic Volcanic Sequence.

Appendix B.7

HIGHLAND RANGE SILICIC VOLCANIC SEQUENCE
Whole-Rock Major Element Geochemistry

Sample	Rock Type	Major Oxide (wt.%)									
		SiO_2	TiO_2	Al_2O_3	Fe_2O_3	MnO	MgO	CaO	Na_2O	K_2O	P_2O_5
Rhyolite Porphyries											
HRAb-05a	Porphyry	74.63	0.356	12.2	2.13	0.051	0.854	1.02	2.73	5.91	0.112
HRA-05g	Porphyry	71.64	0.402	13.0	2.19	0.044	1.013	1.56	4.03	6.06	0.105
HRAb-25d	Porphyry	72.09	0.449	13.5	2.57	0.051	0.949	1.59	3.54	5.08	0.153
HRA-12	Porphyry	71.80	0.407	13.4	2.19	0.047	0.986	1.43	4.20	5.39	0.126
HRL 12a	Porphyry	72.59	0.403	13.5	2.13	0.052	0.760	1.47	3.27	5.69	0.122
Capping Mingled Lava											
HRAb-06a	Mingled Lava	64.92	0.782	14.8	4.62	0.082	2.892	4.08	3.43	4.12	0.288
HRA-38	Mingled Lava	60.23	1.101	15.2	5.71	0.055	3.857	5.21	4.27	3.85	0.532
HRL 14a	Mingled Lava	65.54	0.791	14.5	4.51	0.078	2.763	4.21	3.41	3.88	0.299
Mafic Dike, MMEs (mafic magmatic enclaves), and Dike-Porphyry Hybrid											
HRAb-05c	Dike	57.45	1.177	15.7	6.21	0.052	5.226	6.02	3.52	4.02	0.589
HRAb-05f	MME	57.23	1.175	15.6	6.49	0.082	5.174	5.81	3.54	4.31	0.598
HRA-05h	Dike	58.51	1.185	15.6	6.28	0.056	3.901	5.84	4.22	3.82	0.590
HRAb-06b	MME	55.50	1.298	16.1	7.69	0.112	4.945	7.12	3.77	2.98	0.531
HRAb-25c	MME	55.21	1.355	16.3	7.91	0.092	4.475	7.45	3.75	2.89	0.544
HRAb-05d	Hybrid	59.89	1.036	15.0	5.79	0.083	4.536	5.22	3.48	4.42	0.507
Andesite Lava											
HRA-37	Andesite	57.75	1.158	15.1	6.59	0.062	4.484	6.48	4.31	3.44	0.582
HRAb-40	Andesite	59.50	1.078	15.4	5.98	0.092	4.187	5.54	3.78	3.89	0.534
HRA-42	Andesite	58.12	1.175	15.6	6.38	0.057	4.248	7.15	2.88	3.69	0.685
Searchlight Pluton Felsic Units											
SL43	Felsic Dike	77.35	0.120	12.4	0.77	0.000	0.120	0.31	3.12	5.82	0.000
SL55	Leucogranite	77.88	0.110	12.5	0.59	0.030	0.040	0.30	3.80	4.75	0.000
GG9	Leucogranite	75.74	0.160	13.4	0.99	0.020	0.240	0.90	3.60	4.94	0.030
SL48	Leucogranite	75.74	0.230	13.0	1.35	0.030	0.310	0.87	3.57	4.88	0.050
Other Highland Range Lavas											
HRL 21	Rhyolite Lava	77.40	0.119	12.4	0.69	0.039	0.095	0.64	2.64	5.92	0.011
HRL 26	Trachyandesite	62.09	0.952	15.1	4.98	0.046	3.114	4.83	3.39	4.98	0.531

Appendix B.8

HIGHLAND RANGE SILICIC VOLCANIC SEQUENCE
Whole-Rock Trace Element Geochemistry

ELEMENT	Sample										
	Rhyolite Porphyries					Capping Mingled Lava			Andesite Lava		
	HRAb-5a	HRA-05g	HRAb-25d	HRA-12	HRL12a	HRAb-6a	HRA-38	HRL14a	HRA-37	HRAb-40	HRA-42
Trace Element Abundance (ppm)											
La	48.0	0	55.7	0	58.9	57.3	55.4	56.0	44.6	74.4	68.2
Ce	102	97.0	116	126	104	120	173	110	136	152	78.4
Pr	9.8	--	11.2	--	10.1	12.5	--	13.1	--	17.2	--
Nd	31.3	--	35.7	--	31.0	42.0	--	39.8	--	62.5	--
Sm	4.80	--	5.42	--	5.78	6.56	--	7.24	--	10.53	--
Eu	0.77	--	0.89	--	0.94	1.43	--	1.54	--	2.37	--
Gd	4.13	--	4.66	--	4.03	5.28	--	5.25	--	7.77	--
Tb	0.55	--	0.63	--	0.62	0.66	--	0.74	--	0.92	--
Dy	2.69	--	3.11	--	3.62	3.15	--	4.11	--	4.13	--
Ho	0.55	--	0.65	--	0.73	0.63	--	0.83	--	0.75	--
Er	1.58	--	1.84	--	2.20	1.64	--	2.39	--	1.89	--
Yb	1.74	--	2.00	--	2.25	1.73	--	2.16	--	1.78	--
Lu	0.26	--	0.29	--	0.31	0.25	--	0.33	--	0.26	--
Ni	4.00	18.0	9.00	17.9	--	39.0	25.6	--	25.1	68.0	30.1
Cu	21.0	--	37.0	--	--	36.0	--	--	--	55.0	--
Zn	26.0	--	31.0	--	--	48.0	--	--	--	64.0	--
Rb	158	169	141	156	155	116	112	119	105	94.0	111
Sr	137	151	231	181	173	610	1037	584	1138	1036	1216
Y	18.6	31.0	21.2	31.2	21.0	19.7	26.6	21.0	24.4	22.9	23.9
Zr	210	195	236	201	210	245	321	260	320	341	319
Nb	26.3	13.8	29.0	18.9	21.3	23.2	31.9	20.0	19.0	23.7	28.4
Ba	468	367	558	392	525	839	1283	797	1453	1269	1543
V	31.4	11.8	41.4	12.4	29.0	95.8	134	84.0	164	131	147
Cr	21.4	14.8	22.8	14.3	24.6	67.9	16.8	58.8	19.0	132	14.8
Ga	--	18.5	--	20.2	--	--	22.1	--	23.1	--	18.1
Ta	1.91	--	2.02	--	--	1.38	--	--	--	1.37	--
Hf	4.69	--	5.2	--	5.80	4.84	--	6.80	--	7.11	--
Pb	29.3	--	28.3	--	18.0	23.4	--	19.0	--	18.0	--
Th	16.9	--	18.1	--	18.6	14.6	--	15.6	--	16.2	--
U	3.40	--	3.79	--	3.16	3.32	--	5.53	--	3.72	--

Appendix B.8 (continued)

HIGHLAND RANGE SILICIC VOLCANIC SEQUENCE
Whole-Rock Trace Element Geochemistry (continued)

ELEMENT	Sample											
	Dikes, MMEs, and Porphyry-Dike Hybrid						SLP Felsic Units				Other HR Lavas	
	HRAb-5c	**HRAb-5f**	**HRA-05h**	**HRAb-6b**	**HRAb-25c**	**HRAb-5d**	**SL43**	**SL55**	**GG9**	**SL48**	**HRL 21**	**HRL 26**
Trace Element Abundance (ppm)												
La	78.4	80.9	62.4	66.8	68.8	73.4	--	--	40.0	--	35.7	83.1
Ce	161	160	12.8	133	135	146	--	--	57.5	--	59.8	160
Pr	18.5	18.5	--	15.4	15.8	16.9	--	--	4.76	--	5.48	17.0
Nd	68.1	67.9	--	56.4	58.5	61.2	--	--	14.0	--	13.2	55.3
Sm	11.6	11.5	--	9.7	10.0	10.1	--	--	1.95	--	2.08	10.2
Eu	2.68	2.67	--	2.38	2.45	2.26	--	--	0.23	--	0.20	2.40
Gd	8.38	8.49	--	7.39	7.70	7.48	--	--	1.86	--	1.41	6.60
Tb	0.99	1.01	--	0.93	0.97	0.89	--	--	0.21	--	0.27	0.81
Dy	4.36	4.52	--	4.22	4.56	4.04	--	--	1.13	--	1.81	3.90
Ho	0.78	0.82	--	0.79	0.86	0.73	--	--	0.22	--	0.42	0.72
Er	1.93	2.06	--	1.99	2.13	1.86	--	--	0.72	--	1.47	1.95
Yb	1.77	1.94	--	1.84	1.92	1.78	--	--	0.95	--	1.77	1.68
Lu	0.25	0.28	--	0.26	0.27	0.25	--	--	0.17	--	0.25	0.23
Ni	81.0	76.0	30.0	84.0	85.0	66.0	--	--	--	--	--	--
Cu	58.0	44.0	--	76.0	71.0	48.0	--	--	--	--	--	--
Zn	74.0	73.0	--	71.0	75.0	61.0	--	--	--	--	--	--
Rb	101	99.0	127	67.0	66.0	107	124	218	168	203	202	106
Sr	1084	1055	1154	1075	1055	894	23.0	26.0	149	147	19.0	1083
Y	22.6	24.6	25.2	22.8	24.0	21.8	--	--	--	--	--	--
Zr	345	356	338	293	299	325	100	100	140	210	91.0	382
Nb	22.3	22.4	37.2	19.2	19.2	22.6	--	--	--	--	--	--
Ba	1331	1355	1473	1225	1206	1212	80.0	70.0	640	380	33.0	1610
V	135	130	163	158	163	117	--	--	--	--	--	--
Cr	141	133	19.7	116	129	124	--	--	--	--	--	--
Ga	--	--	22.8	--	--	--	--	--	--	--	--	--
Ta	1.26	1.31	--	1.10	1.12	1.31	--	--	--	--	--	--
Hf	7.39	7.70	--	6.35	6.50	6.81	--	--	--	--	--	--
Pb	16.8	19.7	--	13.2	13.2	18.6	--	--	--	--	--	--
Th	15.9	16.1	--	11.8	12.2	15.8	--	--	--	--	--	--
U	3.59	3.61	--	2.56	2.44	3.62	--	--	--	--	--	--

Appendix B.9

HIGHLAND RANGE SILICIC VOLCANIC SEQUENCE
SHRIMP-RG Quartz Ti Abundance Data

Crystallization temperatures calculated using the equation of Wark and Watson (2006).

Spot Name	Location	Ti (ppm)	Temp (ºC)
HRA-05a (74.63 wt.% SiO_2)			
HRA-05a-2-1.1	Rim	50.8	**710.3**
HRA-05a-2-1.2	Core	72.2	**751.0**
HRA-05a-2-1.3	Rim	64.0	**736.8**
HRA-05a-2-1.4	Rim	63.1	**735.0**
HRA-05a-3-1.1	Core	73.7	**753.5**
HRA-05a-3-1.2	Core	69.7	**746.9**
HRA-05a-3-1.3	Rim	63.2	**735.1**
HRA-05a-3-1.4	Rim	65.3	**739.1**
HRA-05a-4-1.1	Rim	74.4	**754.7**
HRA-05a-4-1.2	Core	74.9	**755.5**
HRA-06a (64.92 wt.% SiO_2)			
HRA-06a-1-1.1	Rim	77.5	**759.7**
HRA-06a-1-1.2	Interior	54.7	**718.5**
HRA-06a-1-1.3	Core	58.8	**726.9**
HRA-06a-1-1.4	Rim	57.5	**724.3**
HRA-06a-2-1.1	Rim	72.2	**751.0**
HRA-06a-2-1.2	Interior	71.2	**749.4**
HRA-06a-3-1.1	Rim	68.4	**744.5**
HRA-06a-3-1.2	Interior	70.6	**748.4**
HRA-06a-3-1.3	Core	89.5	**777.6**
HRA-06a-4-1.1	Rim	80.8	**764.8**
HRA-06a-4-1.2	Interior	87.7	**775.1**
HRA-06a-4-1.3	Core	115.2	**810.8**
HRA-06a-4-1.4	Core	105.6	**799.2**
HRA-06a-5-1.1	Rim	76.6	**758.2**
HRA-06a-5-1.2	Interior	88.6	**776.4**
HRA-06a-5-1.3	Core	66.5	**741.1**
HRA-06a-6-1.1	Rim	79.0	**762.1**
HRA-06a-6-1.2	Core	77.6	**759.8**
HRA-25d (72.09 wt.% SiO_2)			
HRA-25d-1-1.1	Rim	65.1	**738.7**
HRA-25d-1-1.2	Core	92.3	**781.6**
HRA-25d-1-1.3	Interior	79.8	**763.3**
HRA-25d-1-2.1	Rim	67.8	**743.5**
HRA-25d-1-2.2	Core	73.2	**752.7**
HRA-25d-2-1.1	Rim	80.1	**763.8**
HRA-25d-2-1.2	Core	96.9	**787.9**
HRA-25d-2-1.3	Interior	110.7	**805.5**
HRA-25d-2-1.5	Rim	95.3	**785.8**
HRA-25d-2-2.1	Core	76.0	**757.2**
HRA-25d-2-2.2	Interior	61.1	**731.3**
HRA-25d-2-2.3	Core	66.7	**741.5**
HRA-25d-2-2.5	Interior	57.6	**724.5**
HRA-25d-2-2.7	Interior	65.4	**739.3**
HRA-25d-3-1.1	Rim	68.9	**745.5**
HRA-25d-3-1.2	Interior	72.4	**751.4**
HRA-25d-3-1.3	Interior	74.3	**754.6**
HRA-25d-3-2.1	Rim	58.8	**726.7**
HRA-25d-3-2.2	Interior	67.8	**743.4**
HRA-25d-4-1.2	Core	77.8	**760.1**
HRA-25d-4-1.3	Interior	66.9	**741.9**
HRA-25d-4-1.4	Rim	62.3	**733.5**
HRA-25d-5-1.2	Core	79.4	**762.6**
HRA-25d-5-2.1	Rim	65.5	**739.3**
HRA-25d-5-2.2	Core	80.4	**764.3**
HRA-25d-6-1.1	Core	74.0	**754.0**
HRA-25d-6-1.2	Rim	66.7	**741.6**

TiO_2 activity (a_{TiO2}) = 0.70

APPENDIX C

Petrography: representative photomicrographs of the Austurhorn Intrusive Complex and the Highland Range Silicic Volcanic Sequence

AUSTURHORN INTRUSIVE COMPLEX, SOUTHEAST ICELAND

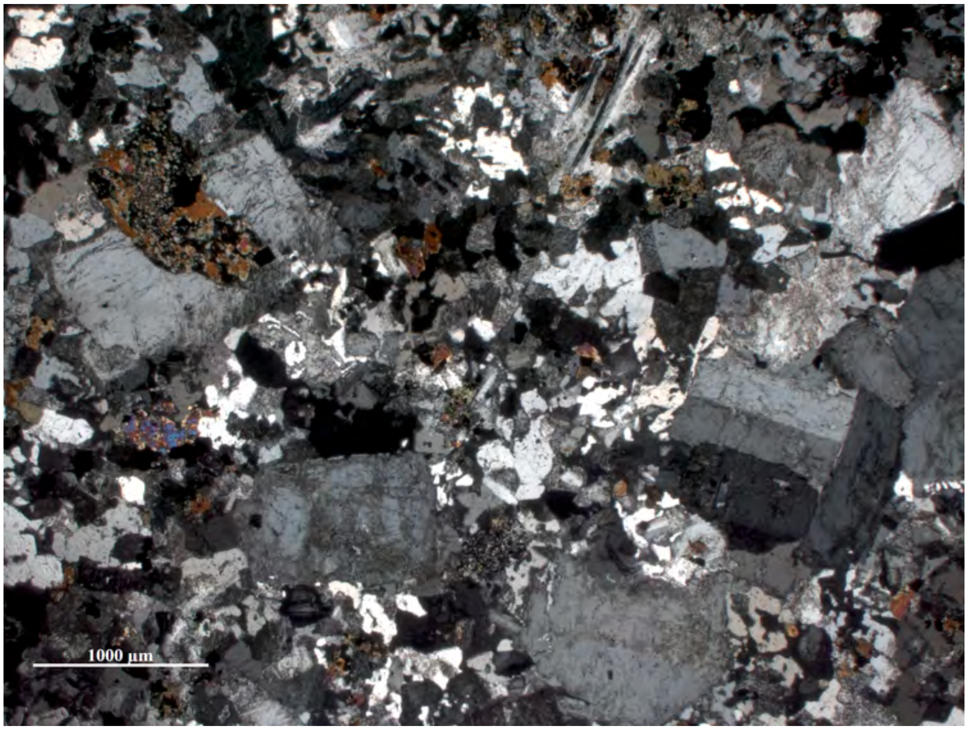

Photomicrograph C.1 – AIC sample IA-NS-2, heterogenous and enclave-bearing granophyre, magnified 2.5x under crossed-polarized light.

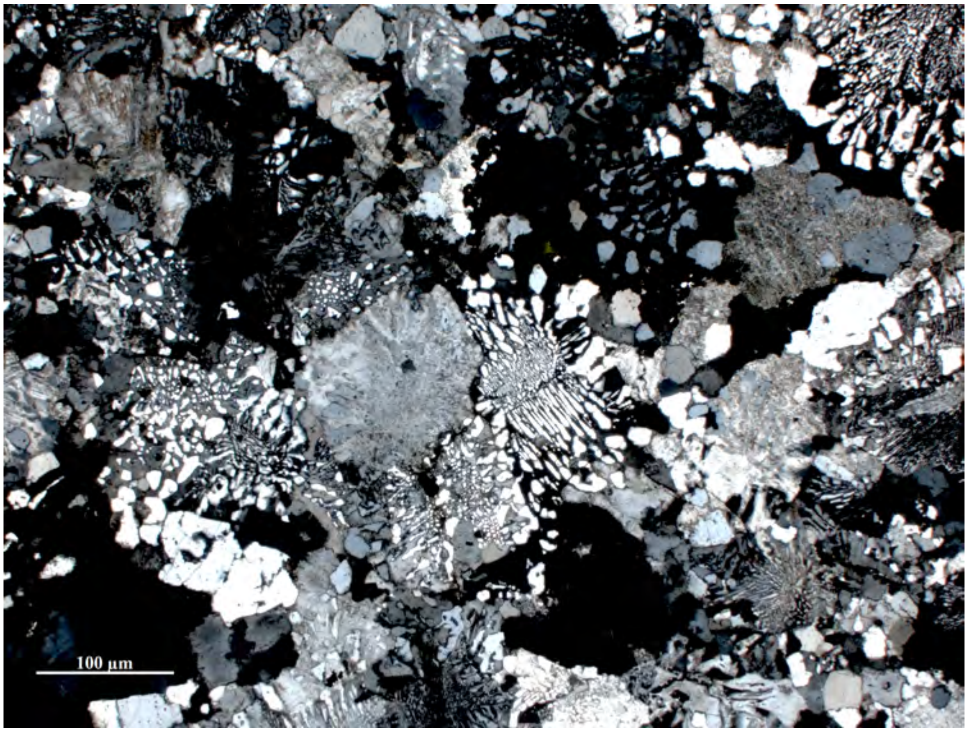

Photomicrograph C.2 – AIC sample IA-NS-4B, homogeneous and enclave-free high-Si granophyre, magnified 2.5x under crossed-polarized light.

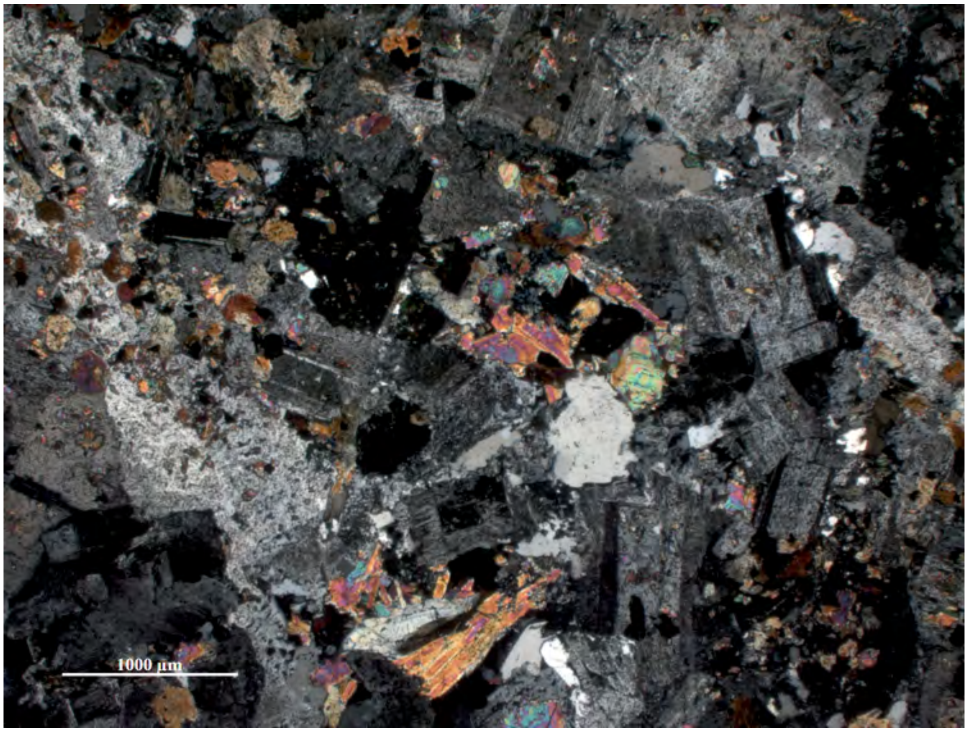

Photomicrograph C.3 – AIC sample IA-NS-6, homogeneous and enclave-bearing diorite, magnified 2.5x under crossed-polarized light.

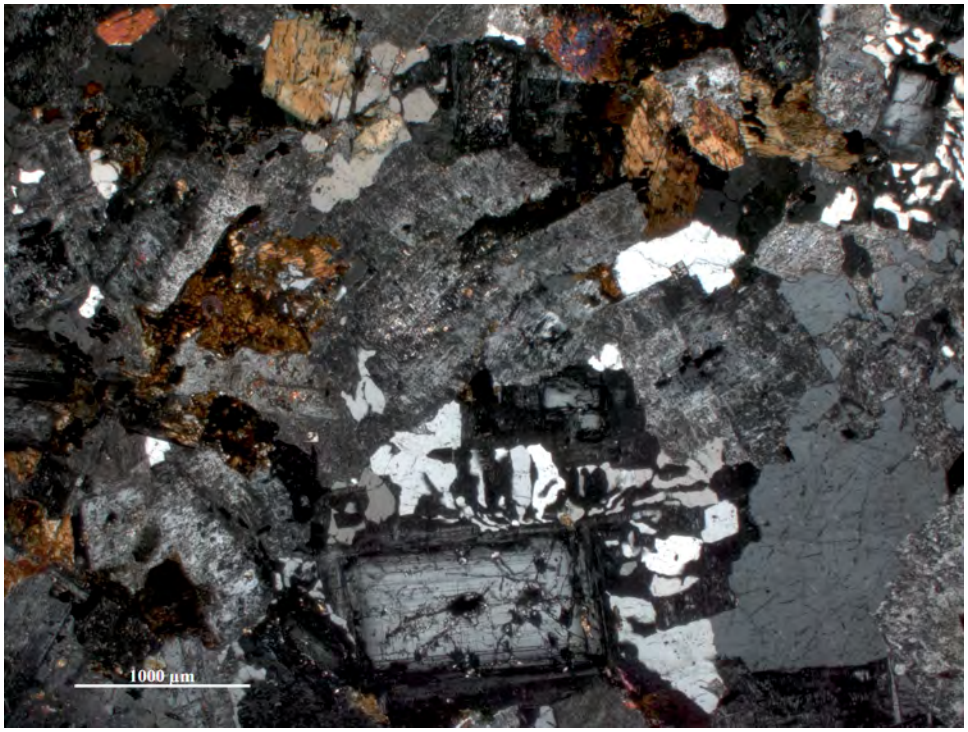

Photomicrograph C.4 – AIC sample IA-NS-7, homogeneous and enclave-free granodiorite, magnified 2.5x under crossed-polarized light.

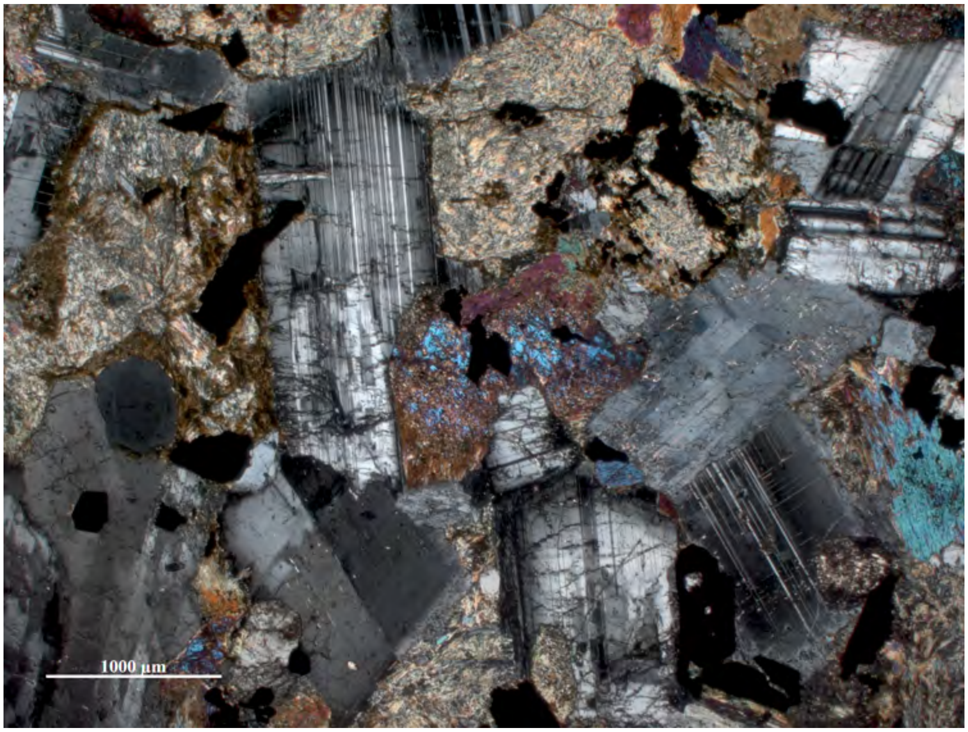

Photomicrograph C.5 – AIC sample IA-G-1, homogeneous *coastal* gabbro, magnified 2.5x under crossed-polarized light.

THE HIGHLAND RANGE SILICIC VOLCANIC SEQUENCE,

SOUTHERN NEVADA

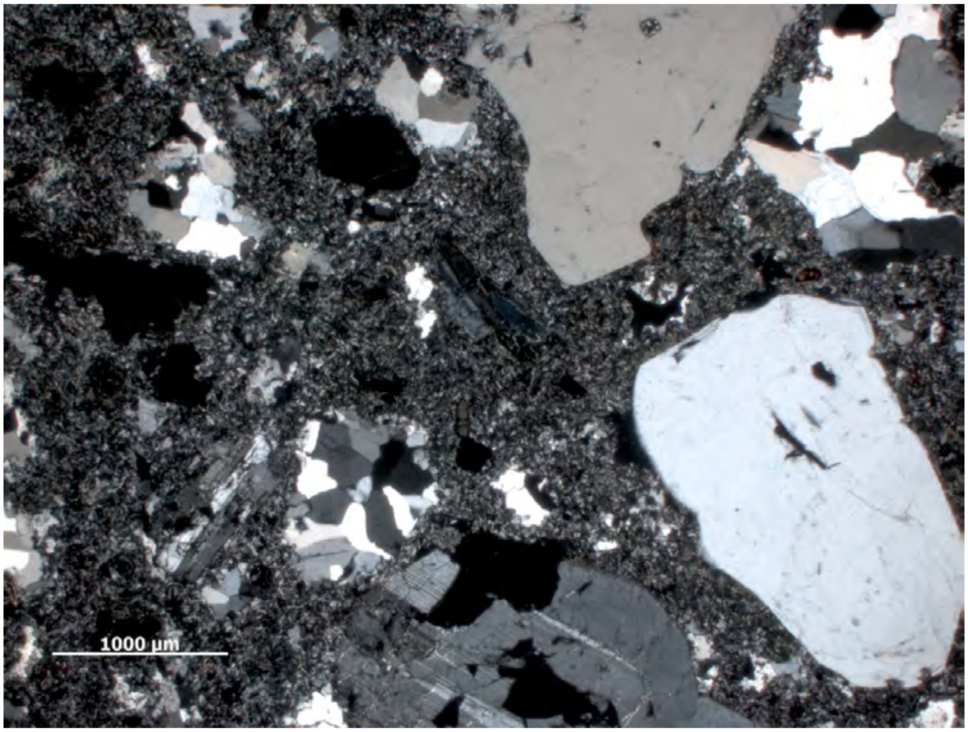

Photomicrograph C.6 – HRSVS sample HRA-05e-1, outermost (hybridized host) zone of a skialithic enclave from the rhyolite porphyry, magnified 2.5x under crossed-polarized light.

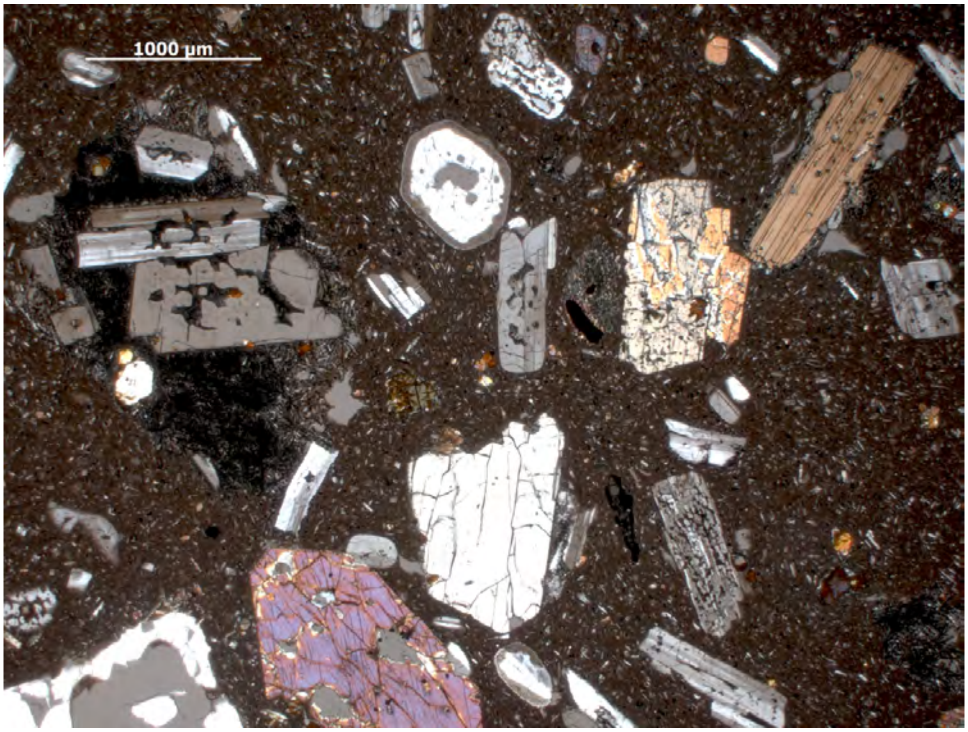

Photomicrograph C.7 – HRSVS sample HRA-06a, vitrophyric capping mingled lava, magnified 2.5x under crossed-polarized light.

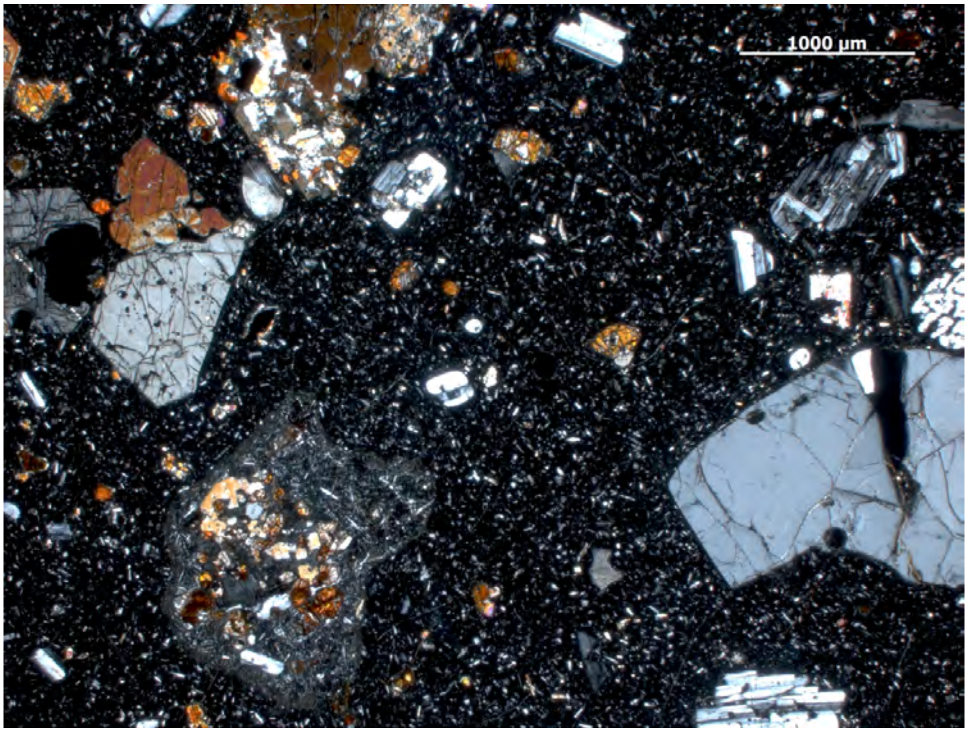

Photomicrograph C.8 – HRSVS sample HRA-25a, vitrophyric, enclave-rich rhyolite porphyry, magnified 2.5x under crossed-polarized light.

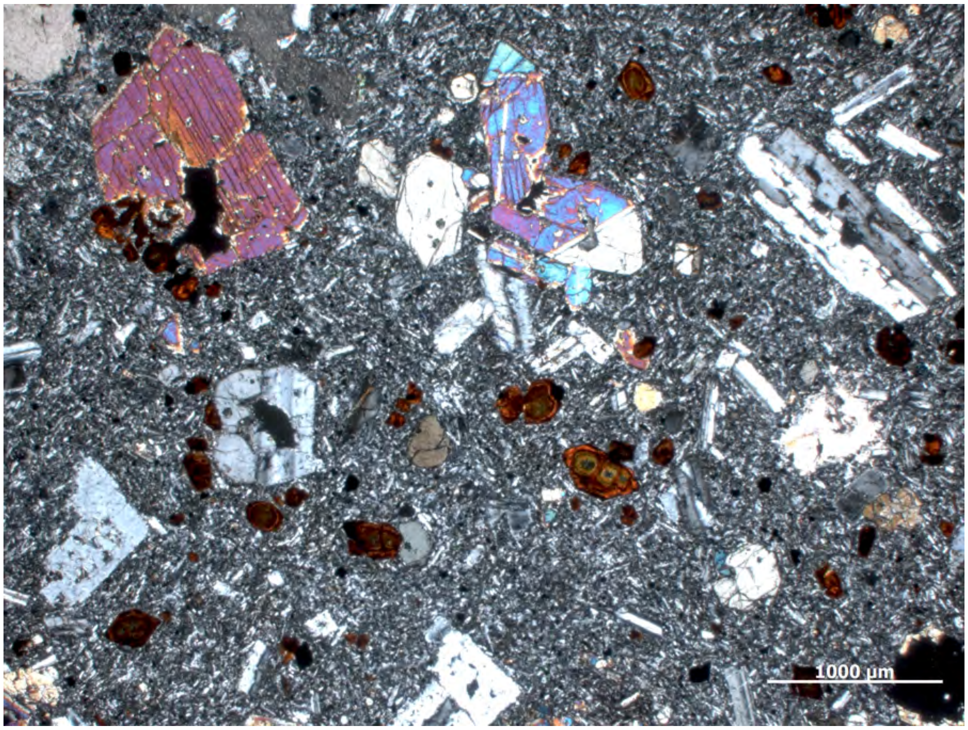

Photomicrograph C.9 – HRSVS sample HRA-42, homogeneous andesite lava, magnified 2.5x under crossed-polarized light.